AFRL-AFOSR-VA-TR-2023-0237

Plasma-Enhanced Flames at Elevated Pressure

Bane, Sally
PURDUE UNIVERSITY
2550 NORTHWESTERN AVE STE 1900
WEST LAFAYETTE, IN, 47906
USA

12/30/2022
Final Technical Report

Air Force Research Laboratory
Air Force Office of Scientific Research
Arlington, Virginia 22203
Air Force Materiel Command

REPORT DOCUMENTATION PAGE

PLEASE DO NOT RETURN YOUR FORM TO THE ABOVE ORGANIZATION.

1. REPORT DATE	2. REPORT TYPE	3. DATES COVERED	
20221230	Final	START DATE 20160930	END DATE 20200331

4. TITLE AND SUBTITLE
Plasma-Enhanced Flames at Elevated Pressure

5a. CONTRACT NUMBER	5b. GRANT NUMBER	5c. PROGRAM ELEMENT NUMBER
	FA9550-16-1-0565	61102F
5d. PROJECT NUMBER	**5e. TASK NUMBER**	**5f. WORK UNIT NUMBER**

6. AUTHOR(S)
Sally Bane

7. PERFORMING ORGANIZATION NAME(S) AND ADDRESS(ES)
PURDUE UNIVERSITY
2550 NORTHWESTERN AVE STE 1900
WEST LAFAYETTE, IN 47906
USA

8. PERFORMING ORGANIZATION REPORT NUMBER

9. SPONSORING/MONITORING AGENCY NAME(S) AND ADDRESS(ES)	10. SPONSOR/MONITOR'S ACRONYM(S)	11. SPONSOR/MONITOR'S REPORT NUMBER(S)
Air Force Office of Scientific Research 875 N. Randolph St. Room 3112 Arlington, VA 22203	AFRL/AFOSR RTA1	AFRL-AFOSR-VA-TR-2023-0237

12. DISTRIBUTION/AVAILABILITY STATEMENT
A Distribution Unlimited: PB Public Release

13. SUPPLEMENTARY NOTES

14. ABSTRACT
A small plasma generation system was first developed using a ring-pin electrode configuration with the goal of producing a plasma disk at the burner outlet. Two distinct plasma regimes were identified: diffused and filamentary. Diffuse discharges were generated at low frequencies while filamentary discharges were generated at moderate to high frequencies. The induced flow fields generated by both diffuse and filamentary plasma discharges were investigated using high-speed schlieren visualization and particle image velocimetry. The rise in gas temperature was measured using optical emission spectroscopy. Lastly, the electrical properties for both types of plasma discharges was measured. The measurements provided a set of pulse parameters for the investigation of the plasma-flame interaction on the atmospheric pressure burner. An atmospheric pressure plasma-assisted burner with a ring-pin electrode geometry was designed and fabricated to investigate the effect of nanosecond repetitively pulsed discharges on methane-air flames. The burner can produce both Bunsen-type and swirl-stabilized flames (helical vane swirlers, swirl number of 0.62) with a modular design to allow for a removable block swirler component.

15. SUBJECT TERMS

16. SECURITY CLASSIFICATION OF:			17. LIMITATION OF ABSTRACT	18. NUMBER OF PAGES
a. REPORT U	b. ABSTRACT U	c. THIS PAGE U	UU	93

19a. NAME OF RESPONSIBLE PERSON	19b. PHONE NUMBER *(Include area code)*
CHIPING LI	426-8574

AFOSR Grant FA9550-16-1-0565
Plasma-Enhanced Flames at Elevated Pressure
Final Technical Report
2020

Nadia Numa and Prashanth Bangalore Venkatesh

Graduate Research Assistants

Sally Bane

Associate Professor

School of Aeronautics and Astronautics

Purdue University

TABLE OF CONTENTS

EXECUTIVE SUMMARY

A small plasma generation system was first developed using a ring-pin electrode configuration with the goal of producing a plasma disk at the burner outlet. Two distinct plasma regimes were identified: diffused and filamentary. Diffuse discharges were generated at low frequencies while filamentary discharges were generated at moderate to high frequencies. The induced flow fields generated by both diffuse and filamentary plasma discharges were investigated using high-speed schlieren visualization and particle image velocimetry. The rise in gas temperature was measured using optical emission spectroscopy. Lastly, the electrical properties for both types of plasma discharges was measured. The measurements provided a set of pulse parameters for the investigation of the plasma-flame interaction on the atmospheric pressure burner. An atmospheric pressure plasma-assisted burner with a ring-pin electrode geometry was designed and fabricated to investigate the effect of nanosecond repetitively pulsed discharges on methane-air flames. The burner can produce both Bunsen-type and swirl-stabilized flames (helical vane swirlers, swirl number of 0.62) with a modular design to allow for a removable block swirler component. Flame chemiluminescence and direct imaging of flame structure and dynamics was done to understand the burner's operating limits. The burner can operate 6 – 13 kW flames, with flames stabilizing at approximately 2 inches above the burner exit. The effect of air flow rate on plasma formation was investigated and it was found that the high velocity of the incoming gas changes the plasma regime and electrical properties. Finally, the plasma discharge was applied on lifted, swirled flames and used for plasma-assisted ignition. For lifted swirled flames, we found that a minimum of 100 pulses is required to generate a filamentary discharge in the air stream. Higher number of pulses at high frequencies appeared to extinguish the primary flame. A minimum of 6000 was used for ignition. Finally, preliminary studies on thermoacoustic instability were performed to establish the unstable operating regime for future plasma control exploration. The plasma-assisted burner will allow for future studies to investigate the plasma flame coupling for various conditions using a wide variety of diagnostics.

1. INTRODUCTION & BACKGROUND

1.1 Motivation

As the standard of living increases through globalization, the consumption of energy has also increased. For several decades, the depletion of natural resources, coupled with the imminent threat of global warming has increased the demand for cleaner fuels and high efficiency combustion technologies. The new combustion strategies require operating near poorly understood limits of combustion stability and at conditions for which the combustion reaction zone development are not understood [1]. New concepts and development strategies are needed to drive the industry into a new generation of technologies providing solutions for more efficient propulsion systems.

The understanding and control of turbulent combustion and flame dynamics is critical for improving the design of propulsion systems. The development of technologies for controlling combustor dynamics would have a tremendous impact, allowing for more efficient energy conversion and longer combustor lifetimes. Plasma, the fourth state of matter, provides new avenues for emission and combustion control. Over the past decade, plasma-assisted combustion and ignition have been widely studied as potential means of improving combustion efficiency across a wide range of applications that include land-based power generation, aviation gas turbines, and supersonic propulsion [2]. While thermal plasma ignition (i.e. spark ignition) has been in use for more than a century, interest in using both non-equilibrium and equilibrium plasmas for ignition and combustion control has drastically increased. The details of the various mechanisms by which a plasma discharge can affect combustion are not yet well understood, but initial experimental and computational studies have been encouraging [2] [3] [4]. These studies have shown that plasmas can have several advantageous effects on flames, including reduced ignition delay, increased flame speed, and enhanced stabilization at low equivalence ratios. These results suggest that plasma-assisted combustion could be a route to leaner combustion with increased stability and lower pollutant emissions.

The overall goal of the current work is to develop an atmospheric pressure plasma-assisted burner to investigate the effect of plasma discharges on combustion at elevated pressures. We begin with the investigation and characterization of plasma discharges in quiescent air based on various pulse parameters. The plasma was generated using a custom nanosecond high voltage pulse generator with variable pulse duration, peak voltage, and pulse repetition frequency. We measured the electrical properties of the discharge and investigated the induced flow fields through high-speed schlieren visualization particle image velocimetry (PIV). The rise in the gas temperature induced by the plasma was also investigated using optical emission spectroscopy (OES).

The plasma characterization work was extended to investigate the plasma-flame interaction for each plasma regime. To achieve this, an atmospheric-pressure plasma-assisted burner was developed to produce both Bunsen-type and swirl-stabilized flames. The burner can produce swirl-stabilized flames and has a modular design to allow for a removable block swirler component. For simple non-swirled flames, the design includes a straight honeycomb structure which serves as a

flow straightener to ensure swirl-free flows. The burner features a ring-pin electrode configuration and in this electrode arrangement, plasma discharges are generated in a disk-shaped planar region at the burner outlet. Flame chemi-luminescence, dynamics, and statistics were used to characterize the burner and to determine the operating envelope to be used to understand the plasma-flame coupling. The influence of airflow rate on the plasma discharges was investigated to understand its effect on the plasma morphology and the electrical energy deposited in the probe volume. Direct imaging of swirled plasma-assisted flames and preliminary plasma-assisted ignition is presented.

Lastly, the electrode configuration used in the plasma characterization work at atmospheric pressure is integrated in Purdue's Aviation Combustion Experiment at Maurice Zucrow Laboratories. A novel injector was designed featuring the electrode configuration as well as a swirl component to maintain parity in the type of flows investigated at atmospheric pressure. This work lays the foundation to begin the investigation of the plasma-flame coupling at pressures relevant to standard engine applications.

1.2 Project Objectives

The overall goal of the proposed work, funded by the Air Force Office of Scientific Research Young Investigator Program (AFOSR YIP), is to advance the understanding of the underlying physics of the plasma-flame coupling in plasma-assisted combustion at elevated pressures. Initial experimental and computational studies have shown that plasma discharges can have several advantageous effects on flames, including reduced ignition delay, increased flame speed, and enhanced stabilization at low equivalence ratios. The purpose of the current work was to establish two experimental platforms at Purdue University for plasma assisted combustion studies. The work spans five primary objectives which are shown in Figure 1. Significant progress made in Tasks 1, 2 and 3 are presented in detail in the following sections. Section 1 discusses the background and presents a summary of literature review. Section 2 discusses the experimental setup and Section 3 discusses the results. Lastly, Section 4 concludes with a summary and recommendation for future work.

TASK	YEAR 1				YEAR 2				YEAR 3			
	Q1	Q2	Q3	Q4	Q1	Q2	Q3	Q4	Q1	Q2	Q3	Q4
1. Development and Characterization of a Plasma System for Flame Enhancement at Elevated Pressures												
1.1 Fabrication, initial testing of electrode geometries												
1.2 Effect of electrode geometry and pulse parameters												
1.3 Plasma measurements at atmospheric pressure												
1.4 Plasma measurements at elevated pressures												
1.5 Characterization of plasma-induced flow field												
2. Investigation of the Effect of Plasma on Premixed Flames at Atmospheric Pressure												
2.1 Design and fabricate portable burner with plasma												
2.2 Burner installation and validation of operation												
2.3 Flame visualization and flame effect on plasma												
2.4 Flame measurements using laser diagnostics												
2.5 PIV measurements of flame flow field												
3. Design and Fabrication of a High-Pressure Plasma-Assisted (HiPPA) Burner												
3.1 High-pressure plasma-assisted burner design												
3.2 Burner fabrication and installation												
3.3 Safety review and validation of burner operation without plasma												
3.4 Integration of plasma and validation at high pressures												
4. Preliminary Characterization of Plasma Effect on Flames at Elevated Pressures												
4.1 Effect of pressure on the flame and plasma												
4.2 Effect of pressure on plasma-flame coupling												
4.3 Develop plan for future high-pressure flame studies												

Figure 1: Project objectives and timeline.

1.3 Plasma Discharge Physics

The simplest illustration of a plasma discharge is the process of ionization of a gas in a tube where two metal electrodes are connected to a DC voltage power supply [5]. When a low voltage is applied to the electrodes in a tube, the recorded current is extremely low resulting in insufficient ionization for the gas to emit light. As the voltage is increased approaching the breakdown voltage, the current increases drastically and light emission is observed. Breakdown begins with ejected electrons and their energy increase as they move in the electric field. The tube subsequently glows with colored light which is dependent on the type of gas used in the tube. This breakdown voltage is a function of the gas pressure as well as the distance between the electrodes. For air at atmospheric pressure, a breakdown voltage of 10s of kVs are required for ionization with a given pair of electrodes at some distance. This ionization process can be best described by the Townsend Mechanism, which posits that the energy of the electrons increases as they move through an applied electric field colliding with gas molecules (creating ions), and consequently the electrons proliferate. The newly produced electrons are accelerated and subsequently produce additional electrons and the cycle repeats until the electric field is removed. This process is referred to as *electron avalanche* allowing conduction through the gas. At low pressures, 1-10 Torr, a glow discharge which is a weakly ionized plasma, develops. A glow discharge is one of the most frequently used types of discharge, i.e., glowing tubes for street advertisements, plasma lamps nebula plasma balls. For glow discharges, the assumption is that the electrons must be able to move freely to efficiently acquire the energy needed for ionization. As gas pressure increases (~ 1 atm), the mobility and mean free path of electrons reduce. Therefore, the Townsend mechanism becomes invalid for discharges created in high pressure conditions.

As the voltage increases, a radiant corona discharge may develop if the electric field is nonuniform and insufficient for breakdown in the entire gap. The discharge is concentrated around the tips of the electrodes. With sufficiently high voltages at atmospheric pressure and gap lengths greater than 10 cm, sparks are produced. This discharge is characterized by rapid growth of a strongly ionized plasma channel from one electrode to another. Lightning is an example of a spark discharge at atmospheric pressure. If the resistance of the external circuit is low to allow for the passage of high current, a continuous arc discharge will develop after breakdown. Arc discharges release high degree of thermal power and the high current heats up the cathode where thermionic emission develops [5]. In the current work, both diffuse and filamentary spark discharges are used to understand the plasma-flame interaction.

1.3.1 Nanosecond Repetitively Pulsed (NRP) Plasma Discharges

Nanosecond repetitively pulsed (NRP) discharge plasmas have been the subject of most of the recent work on plasma-assisted combustion and ignition. NRP discharges are highly effective in the generation of active chemical species with low power demand, resulting in a high degree of electronic excitation and dissociation [6]. The repetitive pulsing allows for the accumulation of species for sustaining the discharge. The production of excited and active species by the plasma

alters the kinetics which is particularly useful for combustion control. The production of atomic oxygen is a particularly advantageous effect of NRP discharges in combustion kinetics. In air plasma discharges, the high concentration of electronically excited N_2 molecules formed by electron impact excitation are quenched by O_2 molecules to produce atomic oxygen atom and heat [7]:

$$N_2(X) + e^- \rightarrow N_2(A, B, C) + e^-$$
$$N_2(A, B, C) + O_2 \rightarrow N_2(X) + 2O + \text{heat}$$

In addition to their efficiency at generating excited and radical species to enhance the kinetics, another important advantage of NRP discharges is their low power consumption due to the small duty cycle. In most studies on plasma assisted combustion, the required plasma power was on the order of 1% or less of the thermal power of the flame.

1.4 Plasma-Assisted Flames

In traditional ignition systems, a spark plug generates a hot plasma between two metal electrodes to ignite a volume of gas resulting in a self-sustaining flame. In this case, the primary ignition mechanism is the thermal effect from the plasma. For an electric discharge, the mechanism is dependent on the type of plasma created. The three most important mechanisms for altering a gas are the thermal, chemical, and fluid dynamics mechanisms [6]. In the thermal mechanism, the energy released in the plasma heats the gas resulting in an increase in the local reaction rates. In the chemical mechanism, excited and active radical species produced by the plasma alters the kinetic pathways. Lastly, in the fluid dynamics mechanism, the production of compression waves and induced flow fields results in a high degree of mixing and localized turbulence.

A substantial amount of research on plasma-assisted flames has been done over the past decade by several different research groups. It has been found that plasma discharges can have a significant effect on many characteristics of the flame, including the laminar flame speed, flame stability limits, blow-off velocity, and most recently, the thermoacoustic instability. Studies have used many different kinds of flames, including premixed and diffusion flames, laminar and turbulent. However, a great deal of work remains to be done to fully understand the physics of the plasma-flame coupling and how to use it to enhance combustion at relevant engine conditions.

1.4.1 Ignition and Flame Speed Enhancement

Nagaraja et al. [8] studied the effect of NRP discharges on a lean premixed H2/O2/N2 flat flame produced using a McKenna burner at low pressure (25 Torr). A metallic mesh placed above the burner was used as the cathode and the burner surface was the ground electrode. In this configuration a uniform, large-volume plasma was produced due to the low pressure and high temperature. They observed an increase in temperature in all parts of the flame and an upstream shift of the reaction zone, indicating faster flame ignition. Xu et al. [9] studied the effect of plasma on a weakly turbulent bluff body-stabilized lean methane/air flame by producing NRP discharges

in the flame recirculation zone. They observed that the OH radicals produced by the discharge were convected into the shear layer where they mixed with the unburned gas and caused almost immediate ignition, indicating a reduction of the chemical ignition time. Vu et al. [10] used a DBD to generate ozone in the oxygen stream of a premixed Bunsen burner and studied the effect on methane/air and propane/air flames. They observed a reduction in the flame height and flame stand-off distance from the burner, implying an increase in the laminar burning velocity. For the same weakly turbulent flame as studied in [9], Lacoste et al. [11] also observed a reduced flame lift-off height when NRP discharges were generated between two pin electrodes above the recirculation zone. The authors noted that the average plasma power was 20 W or less, which was on the order of 1% of the flame thermal power.

1.4.2 Extension of Extinction and Blow-Off Limits

In addition to the enhancement of the laminar flame speed, Vu et al. [10] found that with the additional ozone generated by the DBD plasma, flames could be re-stabilized above the rich flammability limit. They also observed an increase in the flame blow-off velocity. Kim et al. [12] studied blow-off of an ultra-lean premixed methane/air flame stabilized by a mesoscale burner. Using NRP discharges between two electrodes above the burner exit, they were able to extend the lean blow-off limit by 10%. They also observed that the plasma created a “cold” “pre-flame” due to the stream of activated species from the discharge that serves as an in situ fuel reformer. Sun and co-workers [13], [14], [15] have performed several studies on ignition and extinction of plasma-enhanced flames in a counter-flow burner at low pressure (~70 Torr). They found that using plasma-activated oxidizer streams allowed for increase of the extinction strain rates. They also demonstrated for the first time the phenomenon of plasma-activated low temperature combustion (PA-LTC) which may be used to permit ignition at low temperature and pressure.

1.4.3 Emissions

Lacoste et al. [16] studied the effect of plasma on the NO emissions of a lean premixed methane/air swirl-stabilized flame. They used NRP discharges to generate plasma in a disk-shaped region at the outlet of the burner and observed an increase of NO concentration in the burned gases due to the thermal effect of the plasma. Therefore, they concluded that while the plasma can have positive effects on the flame behavior, one must be wary of increasing harmful emissions. They also noted that further experiments at higher Reynolds numbers and elevated pressures are needed to fully understand the plasma effect on emissions. In a separate study in the same research group, Stancu et al. [17] studied the effect of NRP discharges on both NO and CO emissions for a bluff-body stabilized premixed methane/air flame. They found a 20-30% increase in CO due to the plasma for rich flames as well as an increase in NO in the exhaust stream. Through optimization of the discharge (lower voltage, lower PRF, smaller electrode gap), they demonstrated that a lean flame could be stabilized using the discharges while maintaining the NO concentration below the value for an unassisted stoichiometric flame.

1.4.4 Flame Dynamics and Combustion Stability

Pioneering work on the effect of NRP plasma discharges on lean premixed flames has been done by Laux, Lacoste and co-workers. They first studied the effect of NRP plasma discharges on lean premixed propane-air flames in both bluff-body stabilized [18] and swirl-stabilized configurations [19]. They found that the blow-out limit of a 25 kW flame could be extended to higher flow rates and lower equivalence ratios using a plasma power of only 75 W. Similar studies then done using lean methane-air mixtures, and plasma control was shown to extend the lean extinction limit and improve flame anchoring for weakly turbulent bluff-body stabilized flames [20] [11].

Lacoste et al. [21] and Moeck et al. [22] studied the response of a lean methane-air swirl-stabilized premixed flame to acoustic disturbances generated by a loudspeaker with and without plasma at the burner outlet. The plasma discharge was found to have significant effect on the flame transfer function (FTF), which could potentially lead to instability mitigation. Additionally, the plasma had a strong effect on the amplitude of the flame transfer function, reducing it by an order of magnitude using only a small fraction of the flame thermal power. The investigators hypothesized that the changes in the FTF and the flame anchoring location was due to the thermal effect and chemistry of the plasma. Both authors noted that the coupling between plasma, acoustics, and combustion should be studied in greater detail.

In two additional studies, the same researchers investigated the effect of NRP discharges on the thermoacoustic instability [21] [23]. By confining lean, premixed methane/air flames in long quartz tubes, they were able to obtain unstable flames characterized by self-sustained oscillation at frequencies consistent with the quarter-wave mode of the combustor. They found that the velocity fluctuation could be reduced by an order of magnitude [21] and that the pressure oscillations in the combustor could also be mitigated [23] by applying the NRP discharges. It was also found that the electrode arrangement had a strong influence on the plasma control effectiveness; in one configuration, the plasma was actually able to move the flame upstream and re-stabilize it in the burner passage [23]. In a separate study, Lacoste and Moeck showed that the flame could be controlled dynamically at typical instability frequencies by a gated nanosecond glow discharge, which could potentially be used to counteract the thermoacoustic oscillations [24]. The effect of NRP discharges on laminar flame temperature was recently investigated [25] where broadband vibrational CARS was used to determine the temperature of the flame with and without plasma enhancement. The investigators did not see any significant effect on the flame temperature by the plasma but proposed the rotational CARS technique to quantify the local heating in the combustion environment by the plasma. While these studies were performed using flames with relatively low power and at atmospheric pressure only, the results demonstrate the feasibility of using plasma to possibly control and mitigate combustion instability in practical applications.

2. EXPERIMENT SETUP

2.1 Plasma Generation System

A plasma generation system was developed with a pin-ring electrode geometry shown in Figure 2. A length of 63.50 mm inner diameter stainless steel pipe is used for the outer electrode to match the size of the burner exit and a 3.175 mm diameter stainless steel rod is use for the inner electrode, resulting in a gap length of 30.48 mm. The electrodes are precisely machined to minimize surface roughness and are cleaned with isopropyl alcohol before every experiment. Transparent acrylic posts are used to support the electrodes to provide optical access for schlieren visualization axially through the electrode gap. The tip of the center electrode is aligned in the same plane as the ring electrode to produce a plasma in a single two-dimensional plane.

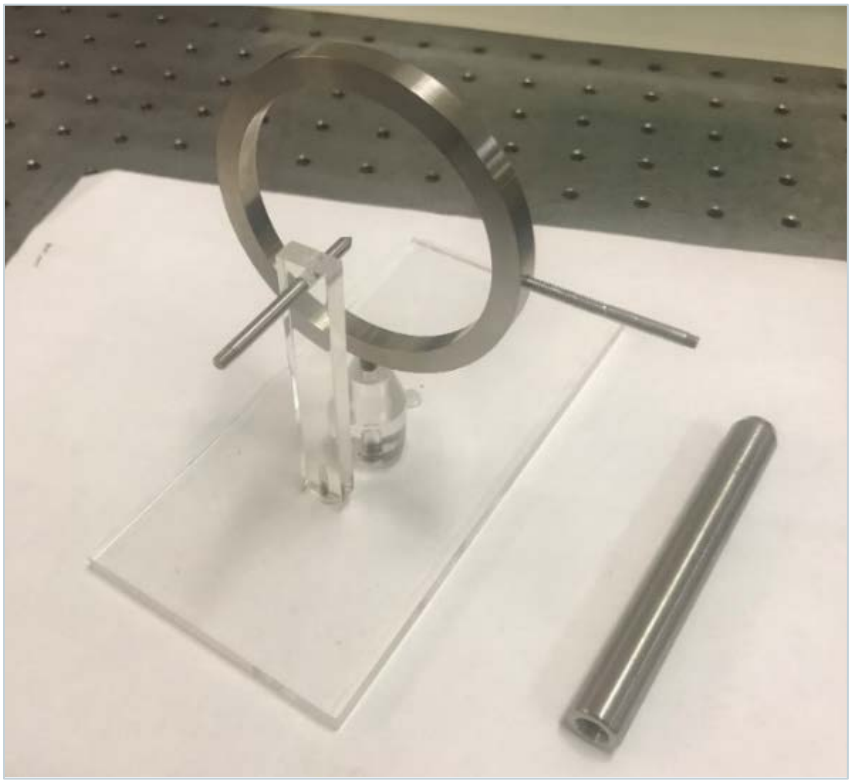

Figure 2: Ring-pin electrode configuration with larger gap (~30.48mm inches) for generating plasma on the atmospheric pressure burner.

The high voltage pulses are generated using a custom-built NSP-3300-20-F nanosecond pulser from Eagle Harbor Technologies is shown in Figure 3. The pulse parameters can be varied, with peak voltage up to 20 kV, pulse duration from 20 ns to 110 ns, and pulse repetition frequency (PRF) up to 400 kHz. The pulser is powered by a TDK-Lambda power supply that can operate between 0 and 500 V DC. The pulser output scales linearly with the power supply input voltage,

where 0-500 V on the power supply is equivalent to 0-20 kV at the output; however, the resistive load at the pulser output restricts the voltage to a maximum of approximately 20 kV. The output of the pulser is floating and the potential is symmetric with respect to ground and so during a pulse, one electrode is at positive potential while the second electrode is at negative potential. The pulser is triggered using a delay generator and a fiber optic transmitter.

Figure 3: NSP-3300-20-F Eage Harbor Technologies Nanosecond Pulser

Two Tektronix P6015A high voltage probes are used to make a differential measurement of the voltage waveform. One probe is connected to the cathode, the other to the anode, and the ground cables of the two probes are connected so the difference in the readings between the two probes gives the voltage across the gap. A Princeton instruments PI-MAX4 1024i intensified CCD camera is used to image the discharge formation. A signal generator is used to trigger both the pulser and the camera. The intensifier gate width is set to capture a series of pulses in a single image to visualize the overall plasma development. The exposure time on the camera is set to a

range of 25-100 ms with varying PRFs of 10-50 kHz. A photograph of the experiment setup for plasma generation and measurement is shown in Figure 4.

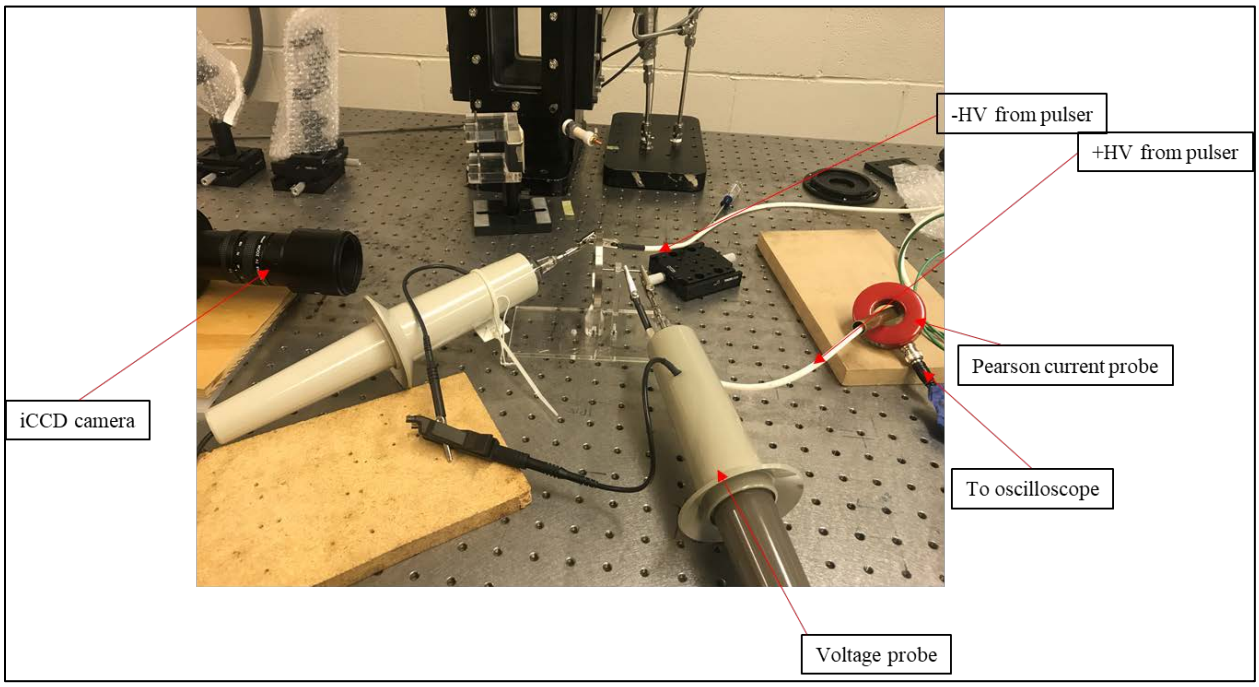

Figure 4: Experimental setup showing the loop-pin electrodes with connections to the HV pulser, probes for discharge voltage and current measurements, and the ICCD camera for plasma imaging.

2.1.1 High-Speed Schlieren and Particle Image Velocimetry

High-speed schlieren visualization and a 10-kHz PIV system are used to study the local flow field induced by the pulsed plasma discharges. A schematic of the schlieren setup is shown in Figure 5 and a photograph of the PIV system is shown in Figure 6. The schlieren system uses an arc lamp as the light source where a condenser of 60 mm focal length is used to collect and direct the light to a pinhole. The light passes through a set of concave mirrors with a focal length of 60 inches and the test section to visualize the density gradients. A Photron FASTCAM SA-Z camera operating at 50,000 fps with 1024x1024 pixel resolution. An ICCD camera is used simultaneously to provide long exposure imaging of the plasma discharge corresponding to each schlieren image.

The PIV system uses an Edgewave INOSSLAB Nd:YAG laser that produces light at 532 nm with pulse repetition rate up to 10 kHz with 10 ns pulse duration. Cylindrical lenses are used to produce a laser sheet approximately 30.48 mm in height for planar PIV. The electrodes are enclosed in a pressure tight steel chamber with fused quartz windows for optical access. Aluminum oxide (Al_2O_3) tracer smoke particles of 0.2 - 0.3-µm in diameter are used to seed the flow. The small size and low density allow the particles to follow the flow without significant lag. PIV images are recorded using a Photron FASTCAM SA-Z camera operating at 10,000 fps with

1024x1024 pixel resolution. The images are processed using PRANA (PIV Research and ANAlysis) software developed by Vlachos and coworkers at Virginia Polytechnic Institute and State University and Purdue University [26]. The entire system is synchronized using a LaVision high speed controller.

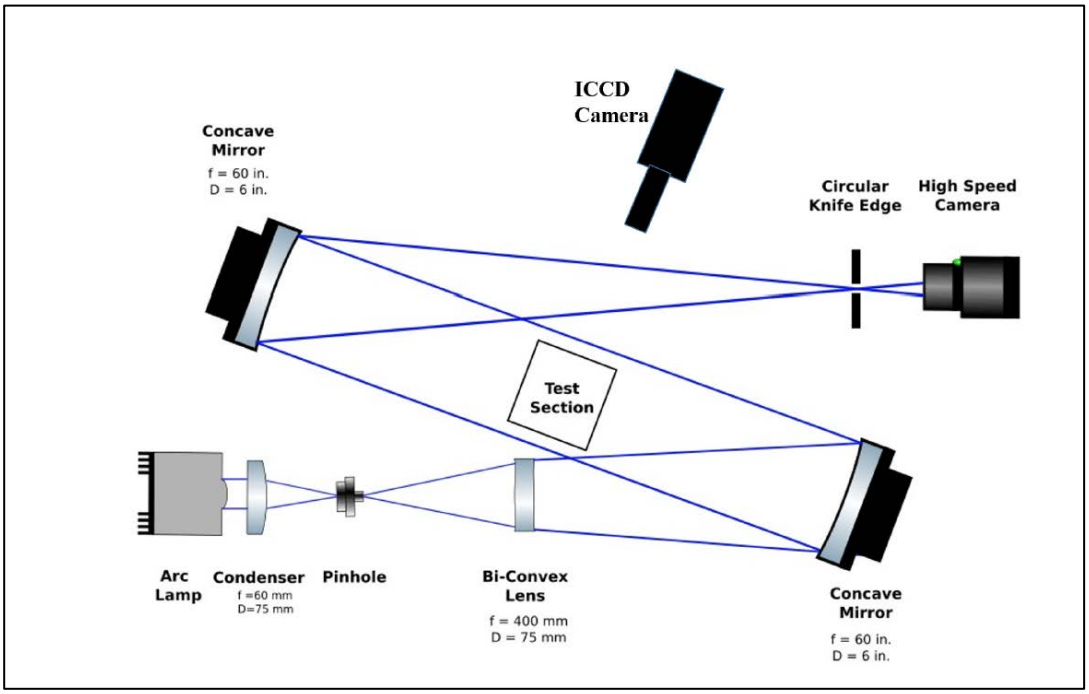

Figure 5: Schematic of the high-speed schlieren visualization system.

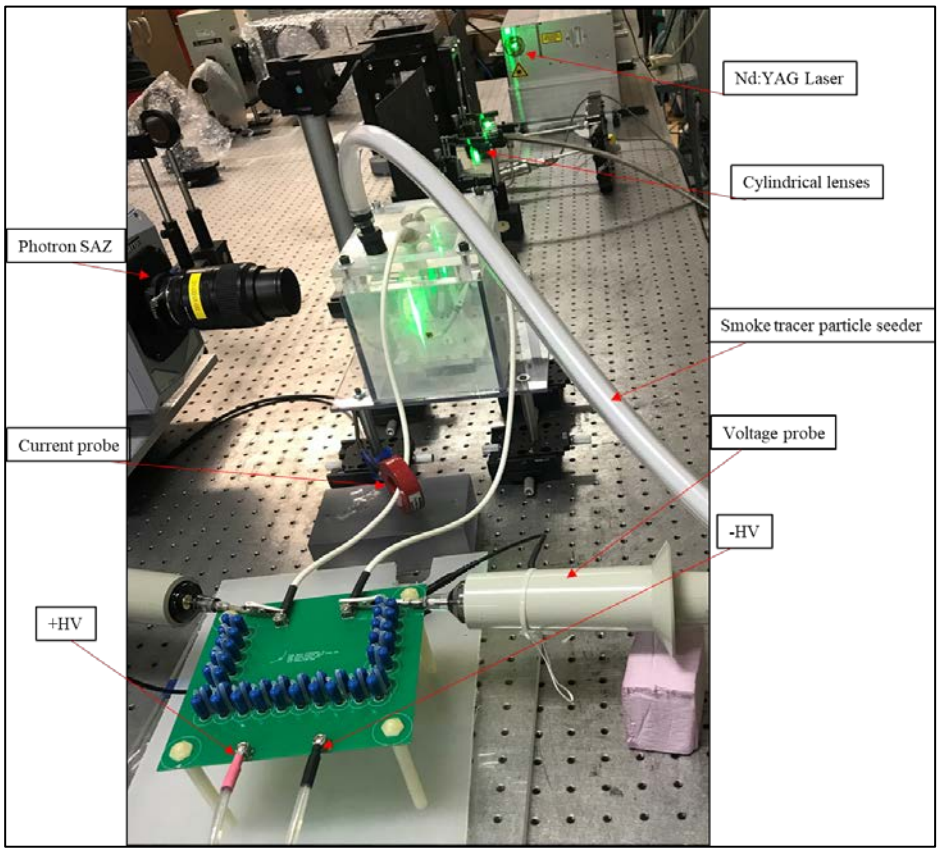

Figure 6: Particle image velocimetry (PIV) setup.

2.2 Atmospheric pressure plasma-assisted burner development

To investigate the effect of nanosecond repetitively pulsed (NRP) plasma discharges on the dynamics of premixed laminar flames at atmospheric pressure, a simple plasma-assisted burner was designed and fabricated. The burner, shown in Figure 7, Figure 8, and Figure 9, was used to establish swirl-stabilized flames and has a modular design to allow for a removable block swirler component. For simple non-swirled flames (Figure 8), the design includes a straight honeycomb structure with 2.8 mm cell size which serves as a flow straightener to ensure swirl-free flows. A 3.2 mm stainless steel central pin electrode, held by a transparent acrylic bar for insulation, is extended to the burner exit and serves as the anode. A stainless-steel circular ring with an inner diameter of 63.5 mm mounted at the burner exit serves as the cathode. An electrically insulated ceramic flange holds the circular electrode to isolate it from the burner body and to also withstand heat from the flame. The electrodes are connected to the nanosecond pulser through insulated cables and a high voltage electrical feedthrough is installed in the burner tube to provide the positive potential to the central pin electrode. In this electrode arrangement, plasma discharges are generated in a disk-shaped planar region at the burner outlet. The swirler is currently placed approximately 6.35 mm upstream of the burner exit plane. However, the burner's modular design allows for a block swirler component to be placed approximately 102 mm upstream for high flow

rate applications. A stainless steel flange holds a quartz rectangular box to provide confinement for the flame. The rectangular cross section was chosen for future laser diagnostics measurements instead of a circular cross section. A confinement ratio (area ratio between the rectangular duct and the burner exit) of 4 was chosen to induce a large central recirculation zone at the swirler exit [27].

The plumbing and instrumentation photograph and diagram are shown in Figure 10 and Figure 11. Fuel and air are injected far upstream of the burner to produce premixed fuel/oxidizer conditions at the burner outlet. Mass flow controllers by Alicat Scientific are used to regulate the mass flow rate to the burner, providing a range of flow rates similar to those used by Pilla et al. [18]. The air and methane flow controllers are capable of flowrates up to 1500 SLPM and 100 SLPM for high flame thermal power conditions. The pneumatically actuated valves, stainless steel tubing, and fittings were obtained from Swagelok. The experiment uses a LabVIEW visual instrument (VI) control, shown in Figure 12 for data acquisition. The VI uses 5 digital output (DO) channels and 4 analog output/input (AO/AI) channels. Additionally, the VI is capable of recording temperatures and externally trigger the nanosecond pulser. All electrical components were obtained from DigiKey and the NI module was obtained from National Instruments.

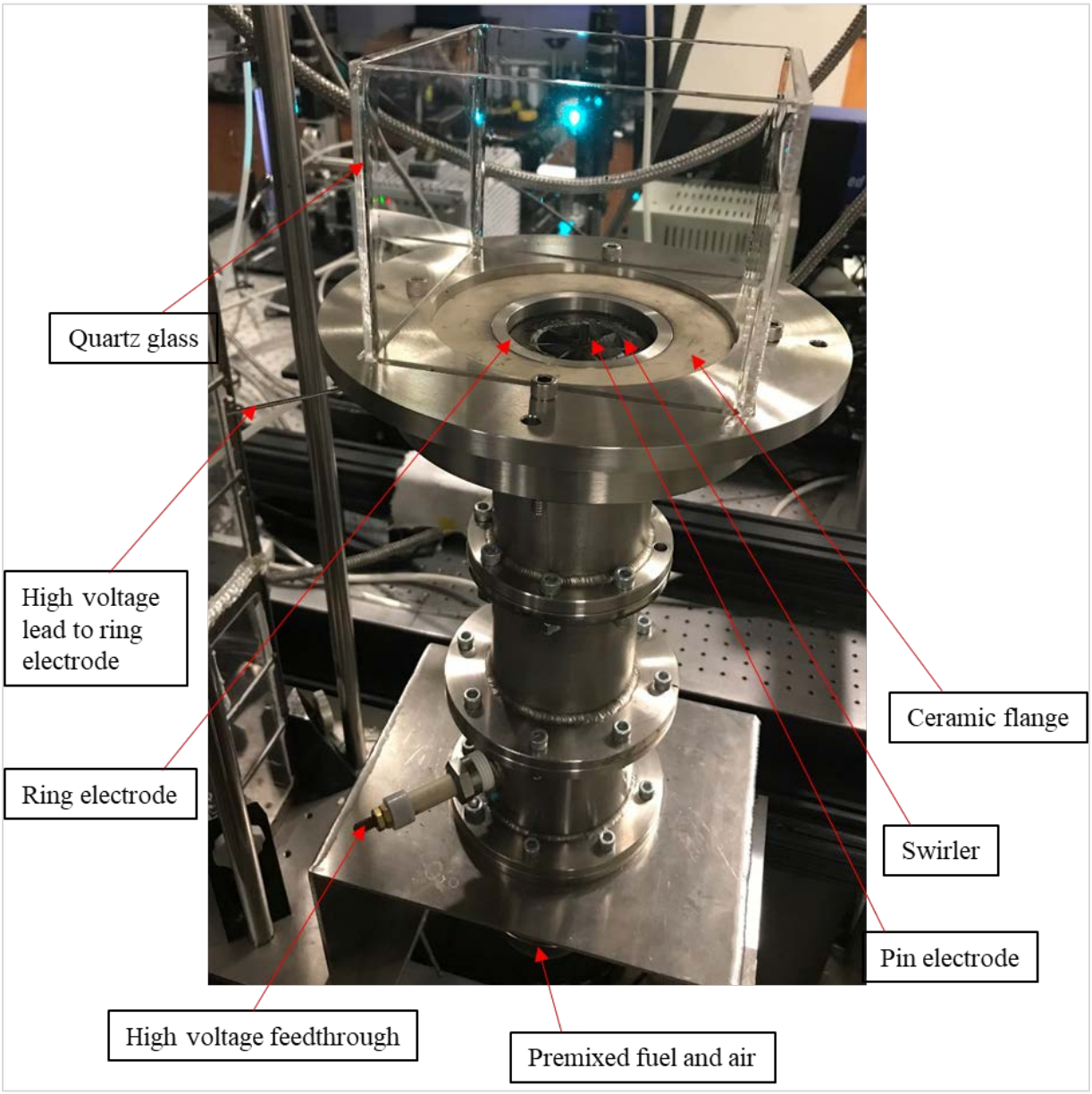

Figure 7: Swirl stabilized plasma-assisted burner.

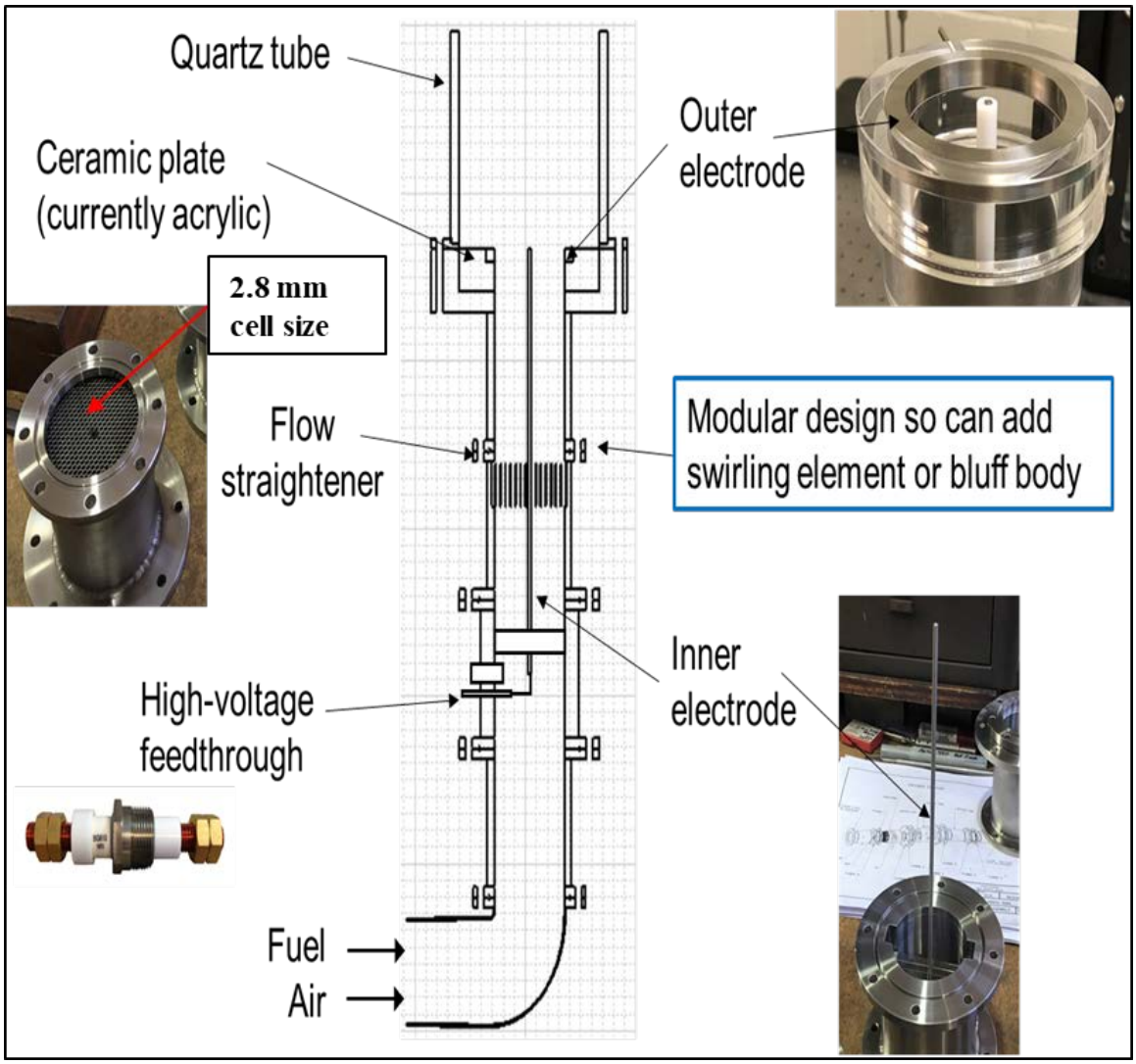

Figure 8: Cross sectional view of the atmospheric pressure burner, non-swirl configuration.

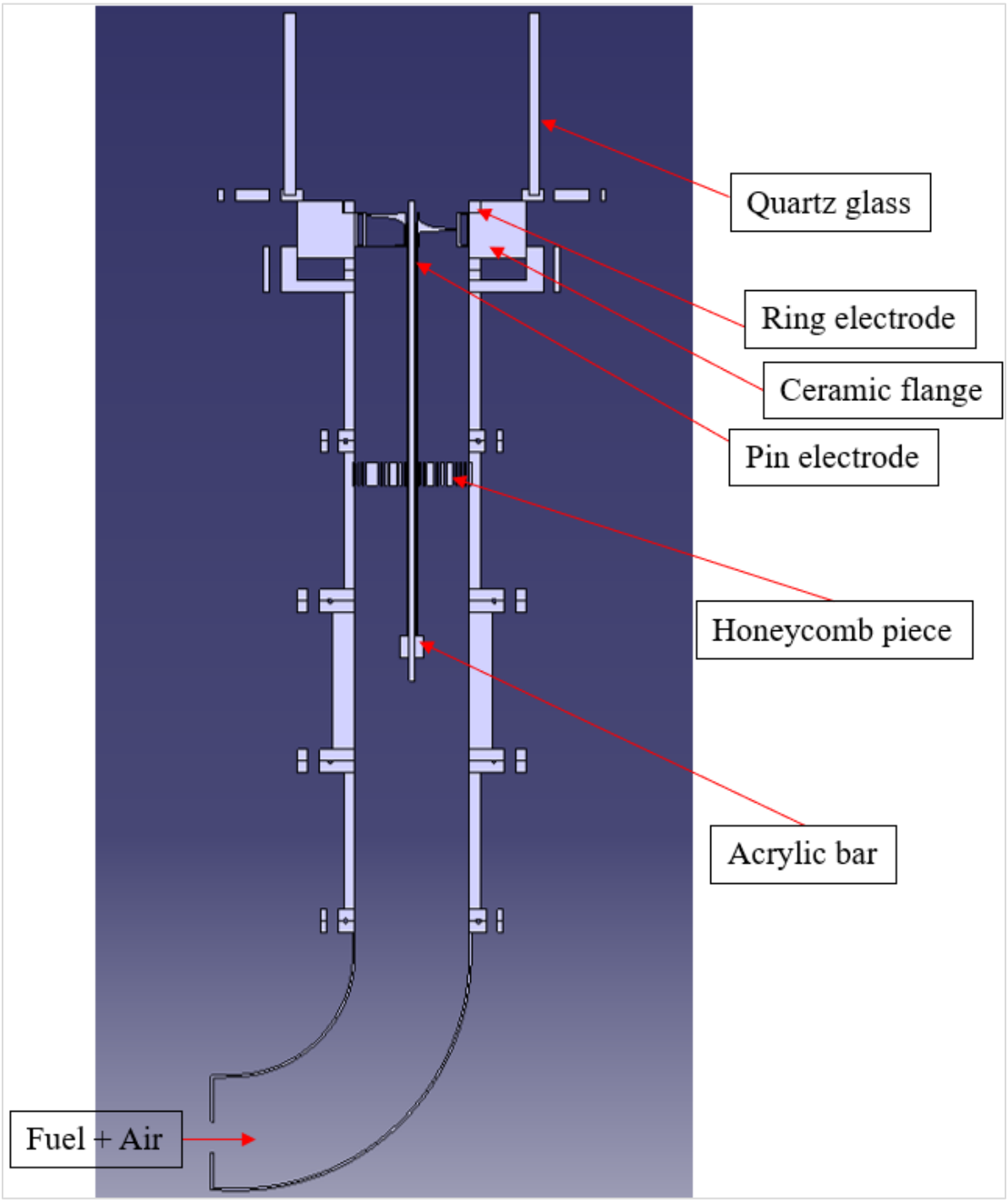

Figure 9: Cross sectional view of the atmospheric pressure burner, swirl configuration.

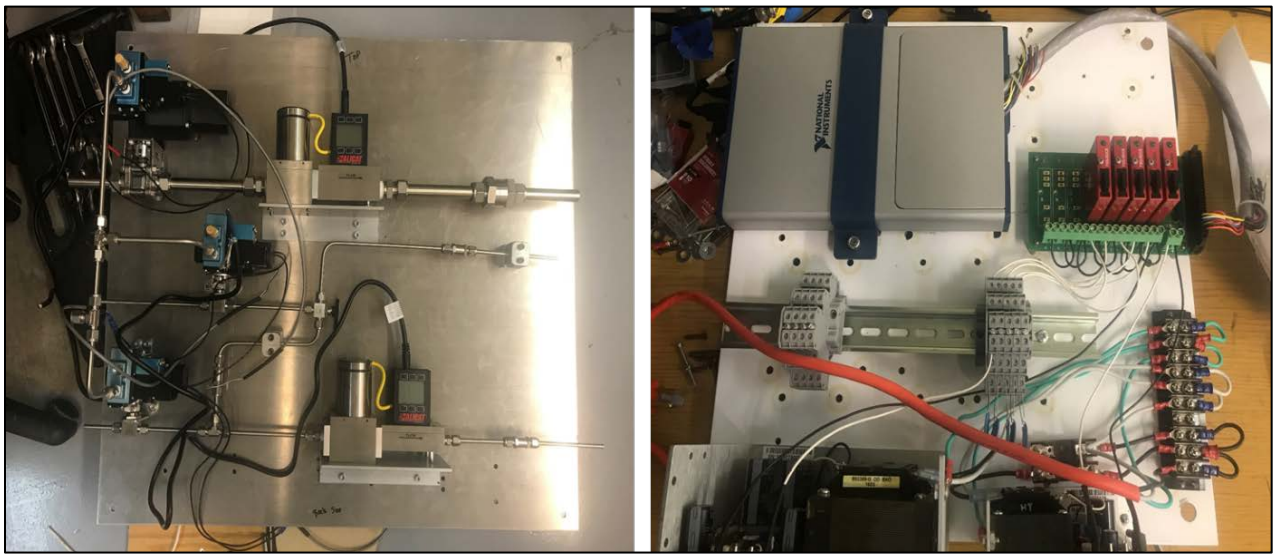

Figure 10: Plumbing panel for fuel, air, and purge gas (nitrogen) delivery (left) and the experiment control and data acquisition (DAQ) panel (right).

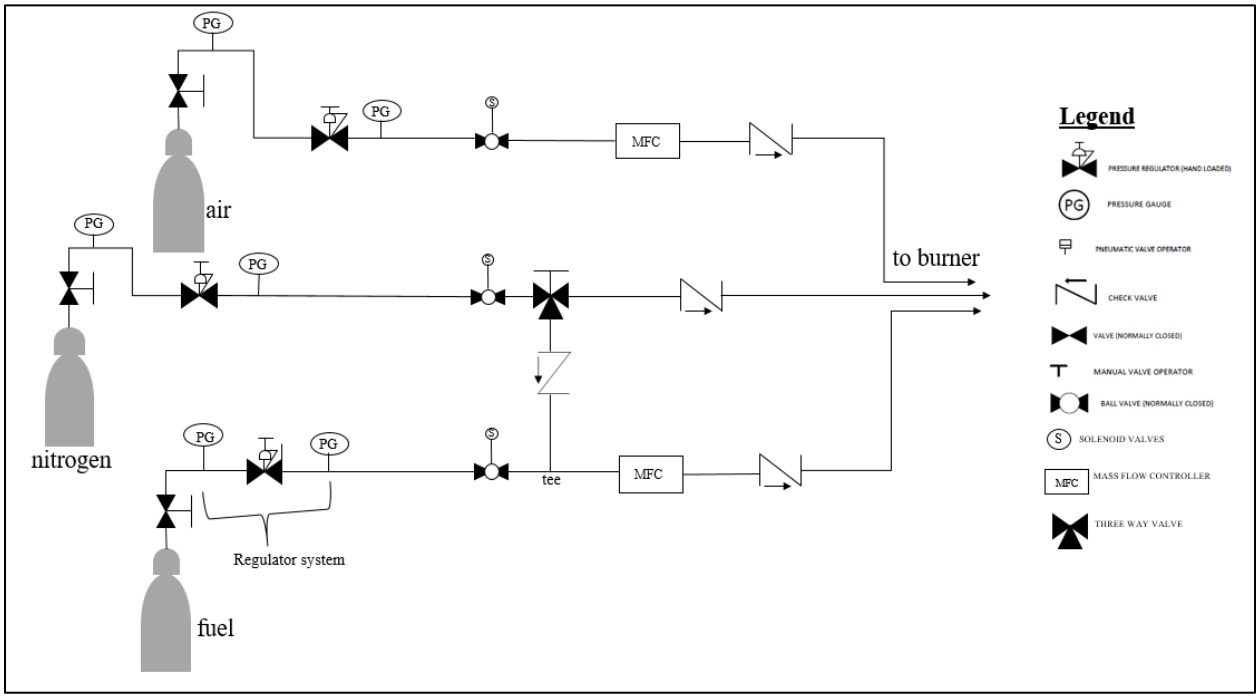

Figure 11: Plumbing and instrumentation diagram (P&ID) for fuel/oxidizer/nitrogen delivery panel.

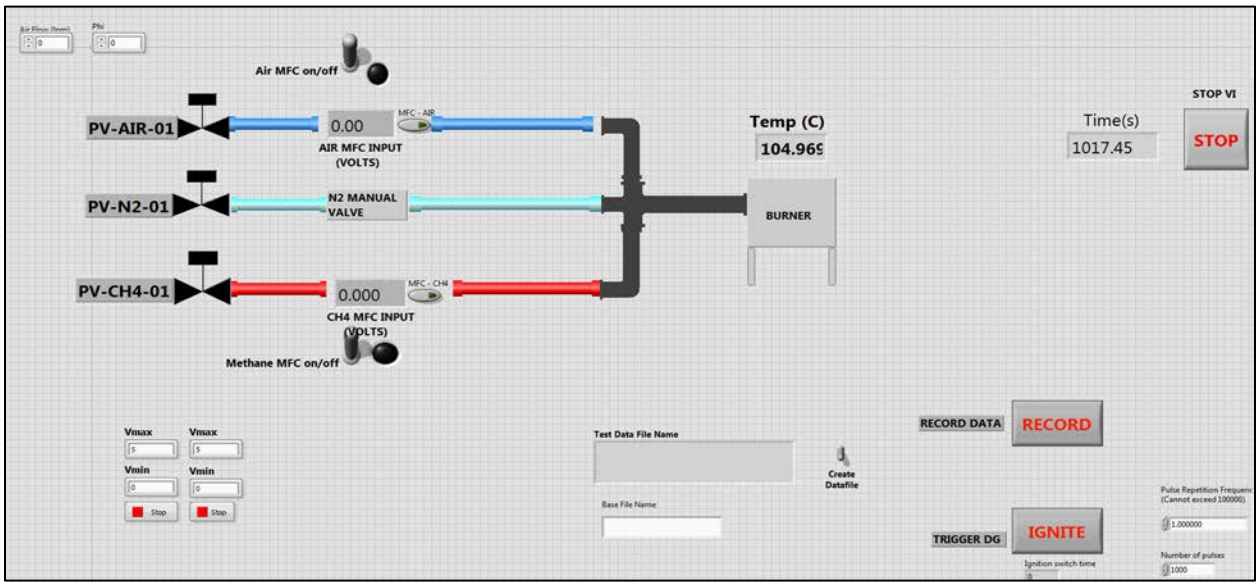

Figure 12: Experiment LabVIEW visual instrument controls.

2.2.1 Swirler Design

Flame stabilization can be achieved by introducing a swirl component to the flow using swirl vanes. Experimental studies have shown the swirl component to effect flame stability, shape, size, and combustion intensity [28]. The degree of recirculation is a function of the swirler geometry. Weak swirling flows (S < 0.6) are characterized by insufficient internal recirculation due to inadequate pressure gradients in the axial direction. Strong swirling flows are characterized by a strong central recirculation zone due to large radial and axial pressure gradients containing chemically active species and well-mixed combustion products [29] [30]. The swirl number, a non-dimensional parameter used to describe swirled flows, is the axial flux of swirl momentum (G_θ) divided by axial flux of axial momentum (G_x) times the equivalent nozzle radius [29]:

$$S = \frac{G_\theta}{G_x * R} \qquad (1)$$

$$G_\theta = \int_0^\infty (\rho uw + pu'w')r^2 dr \qquad (2)$$

$$G_x = \int_0^\infty \left(\rho u^2 + \rho U'^2 + (P - P_\infty)\right) r dr \qquad (3)$$

For a helical axial-vaned swirler, the swirl number can be approximated as function of the swirl tip vane angle, θ_m, and the swirler radii R_1 and R_2. By assuming constant axial velocity in the radial direction and omitting the static pressure term, G_θ and G_x can be approximated as [28] [31]:

$$G_\theta = \int_{R_1}^{R_2} (Wr) * \rho U * 2\pi r dr \qquad (4)$$

$$G_x = \int_{R_1}^{R_2} \rho U * U * 2\pi r dr = \pi\rho * U^2 * (R_2^2 - R_1^2) \qquad (5)$$

where the tangential velocity component, W, is approximated by $W = U * tan\theta$ and U is the axial velocity component of the incoming gas. Therefore,

$$S_1 = \frac{R_2^2 + R_1^2}{2R_2^2} * tan\theta_m \quad (6)$$

Empirical swirler design information was also referenced from Purdue's Internal Combustion course to establish the swirler passage aspect ratio, L/b, defined as the length of the swirler passage to its width. The vane height and the number of vanes is used to control this ratio, and an ideal L/b is approximately 2.5. If the length of the swirler passage is too short compared to its width, insufficient swirl will be imparted unto the incoming flow. If the length of the passage is too long, it will result in superfluous flow restriction. In the current work, the L/b for all swirlers used ranges from 2.1 - 2.6 and an example of how the swirler passage ratio was determined is shown in **Error! Reference source not found.**.

Table 1: Example geometry calculation for a 1.5-inch inner diameter swirler.

Theta	50
T_{vane}	0.04
L	0.68
No. vanes	7
D_o	1.5
D_i	0.312
b	0.273
L/b	2.495

Various swirlers, 3D printed out of thermoplastic polymer ABS, were used to investigate the burner flow field. The first swirler geometry, shown in Figure 13, was designed to be mounted approximately 90 mm upstream of the burner exit plane with rectangular vanes positioned at 45 degrees. This geometry resulted in a toroidal vortex-like flame, which stabilized upstream of the exit plane on the hub of the swirler. The high thermal release from the flame was entrained to the hub of the swirler, thereby exceeding the temperature capability of the polymer.

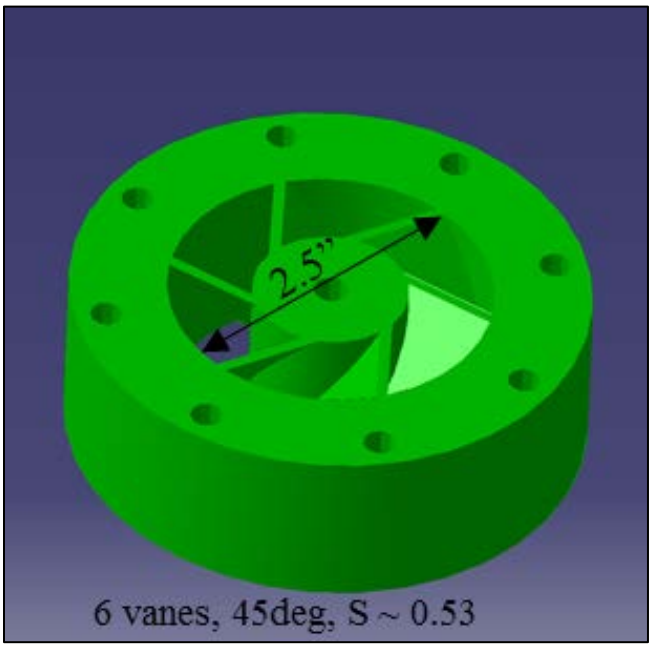

Figure 13: Initial swirler design with an inner passage diameter of 2.5 inches and a swirl number of 0.53.

In the latest swirler designs, shown in Figure 14, the vanes were changed from rectangular to helical for more efficient swirl generation and to minimize the pressure drop across the swirler [31]. The swirl angle was changed from 45 degrees to 50 degrees to generate more compact flames as well as a stronger central recirculation zone. The swirler inner diameters are 2 and 1.5 in., resulting in swirl numbers of 0.61 and 0.62, respectively. Additionally, a plastic insert was printed for the 1.5 in. swirler to reduce the flow rate requirements and to investigate swirl stabilized flames at lower thermal powers, as seen Figure 14. A high temperature stainless steel paint was used to coat the swirlers to increase their temperature capacity. The metal coating allowed for longer flame operation given that the burner is not currently water-cooled. Additionally, as the swirlers become more damaged by use (Figure 15), a higher the equivalence ratio is required to sustain a lifted flame. The damaged swirl vanes produce less swirl which in turn increases the axial velocity. As the axial velocity increases, the flame speed must increase to maintain a lifted, unattached flame.

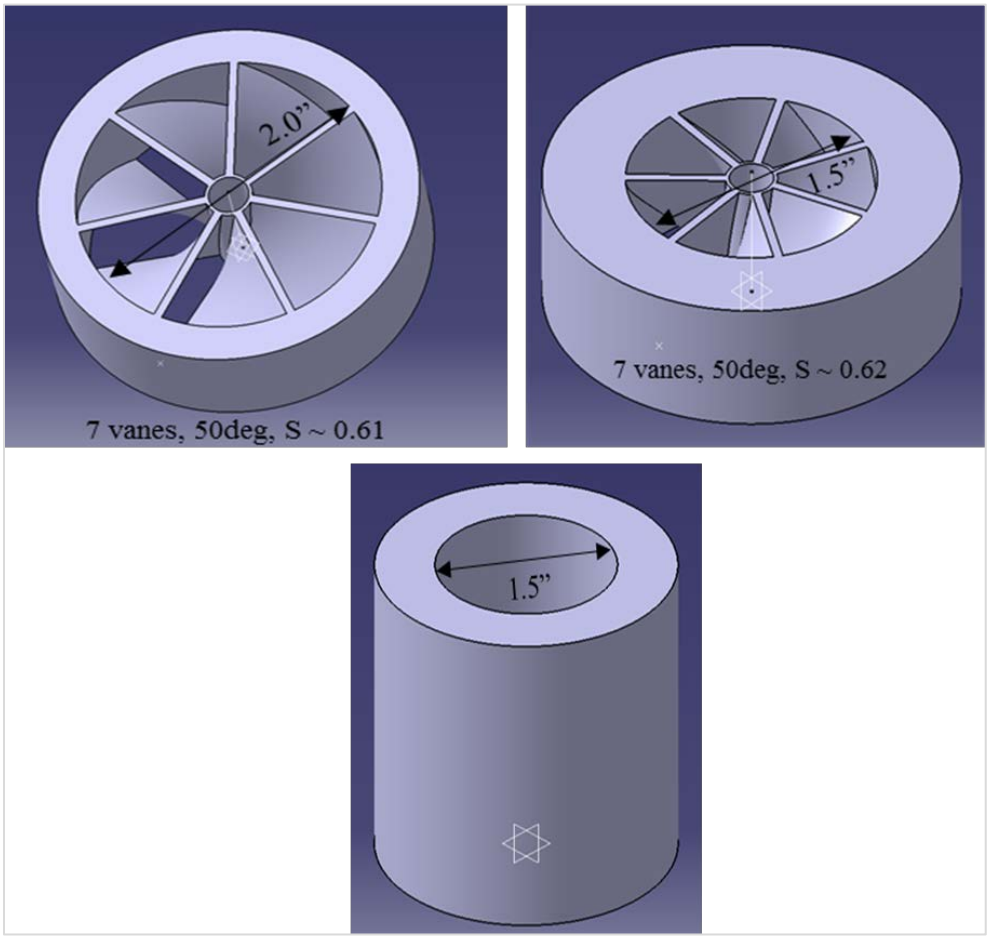

Figure 14: Final swirler designs and insert for the atmospheric pressure burner.

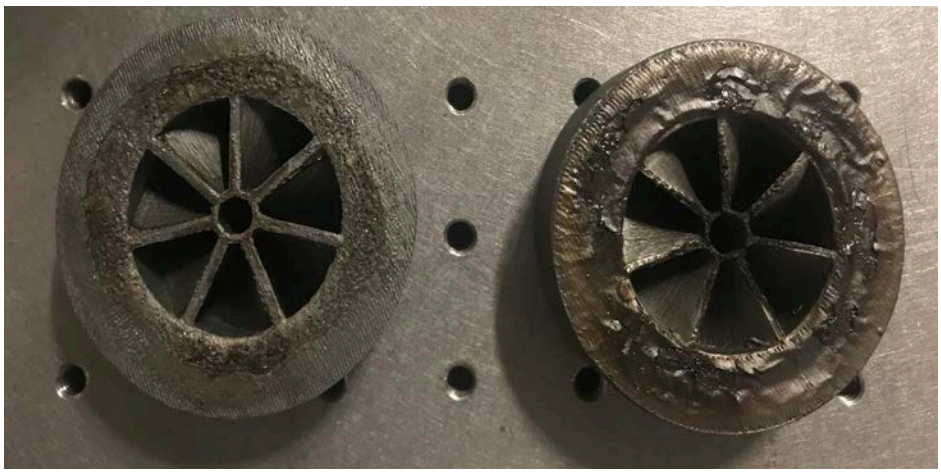

Figure 15: Evolution of swirler damage from exposure to the burner flame.

2.2.2 Flame Chemiluminescence and Dynamics

Flame chemiluminescence is primarily produced by electronically excited species such as CH*, C_2*, and OH*. Specifically, CH* chemiluminescence is used to study flame response and estimate the flame front location [32]. Images of CH* chemiluminescence of a lean premixed methane-air flame were obtained at 10 fps using a Princeton instruments PI-MAX4 1024i intensified CCD camera. The exposure on the camera was set to 500 microseconds with a gain of 60. A Semrock 434/17nm BrightLine single-band bandpass filter was mounted to the intensified camera to capture the signal emitted from CH*. The experimental schematic is shown in Figure 16. A Bernzomatic propane torch was used to ignite the flame in the absence of the NRP plasma discharge. To investigate the flame dynamics and structure, high-speed images were obtained using a Photron FASTCAM SAZ model 500K-M2 high-speed camera with a Nikon NIKKOR Z 70-210mm lens. The camera is coupled with a LaVision High-speed IRO controller. At maximum resolution (1024 X 1024), the Photron SA-Z camera offers frame rates up to 21000 fps. The LaVision high-speed IRO coupled to the SA-Z camera is suitable high-speed imaging and is capable of gating times down to 10 ns and a spectral range of 190 – 800 nm. For these series of tests, the camera frame rate set to 8000 fps and a shutter speed of 125 µs and the high-speed controller was set to a constant gain of 65% with an intensifier gate between 100 µs. Investigation of the flame structure and dynamics provided insight into the ignition kernel development, blow-off, and attachment. The investigation was also used to predict the onset of flame blow-off and flashback to the swirler and the burner exit plane.

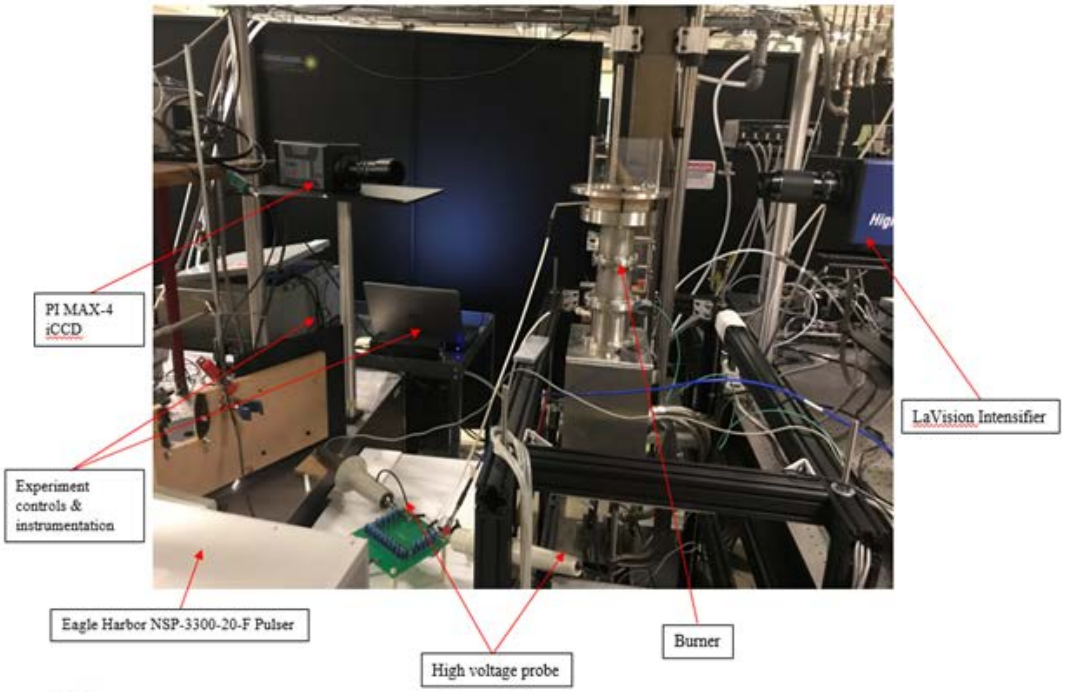

Figure 16: Experimental setup for flame chemiluminescence imaging.

2.2.3 Optical Emission Spectroscopy

The mean temperature of the gas in the electrode gap from the plasma discharge in the pin-ring electrode configuration was investigated using optical emission spectroscopy (OES). The plasma was generated using the high-voltage pulse generator described in Section 2.1. The charged species, made up of excited atoms and molecules, present in the electrode gap from the discharge emit light at a range of wavelengths, each with its unique spectral line. These characteristic emission lines correspond to the electron transitions between the various energy levels. The plasma emission was collimated and focused onto the entrance slit of a Princeton Instruments 2500i Spectrometer using two off-axis parabolic (OAP) mirrors with 2" reflected focal length. The slit width of the spectrometer was set to 50 microns with a 2400 gr/mm^{-1} grating to allow for precise spectral resolution for averaged temperature measurements. The ICCD camera (NI PI-MAX4) was used to detect the emission intensity and produced spectrum of light intensity versus wavelength. The experimental spectra were fit with theoretical spectra to extract the gas temperature using open source spectral-fitting software [33]. The experimental schematic for the OES measurements is shown in Figure 17.

We began with the ring-pin electrode configuration with an electrode gap of 11 mm. The electrode fixture was placed approximately 102 mm from the first off-axis mirror. The intensifier gate of the ICCD camera was gated at 100 ns to capture the spectrum from one discharge inside a train of pulses and spectra from the same discharge (within the train) were accumulated over a large number of tests to increase the signal-to-noise ratio (SNR). Gating the ICCD camera for 100 ns at a time (during the length of the pulse train) reduced the accumulation of background noise resulting in higher fidelity of temperature measurements. The camera conditions kept constant at a gain of 0, a gate delay of 29 and the center wavelength was set to 377 nm. The interrogation area shown in Figure 17 was used and once the spectral lines were detected, the data was biased in the y-axis direction to obtain all spectral measurements. The plasma temperature was obtained from the second positive system of molecular nitrogen, the second overtone. The second overtone was chosen to prevent the camera from saturating from the significant light emission from the plasma discharge. The PRF was varied (5, 10, 20, and 50 kHz) to investigate the effect of the pulse frequency on the gas temperature and a summary of the pulse parameters is presented in Table 2.

Table 2: Electrical pulse parameters for gas temperature measurements.

Case	PRF (kHz)	No. of Pulses	Burst Duration (ms)
1	5	250	50
2	10	500	50
3	20	1000	50
4	50	2500	50

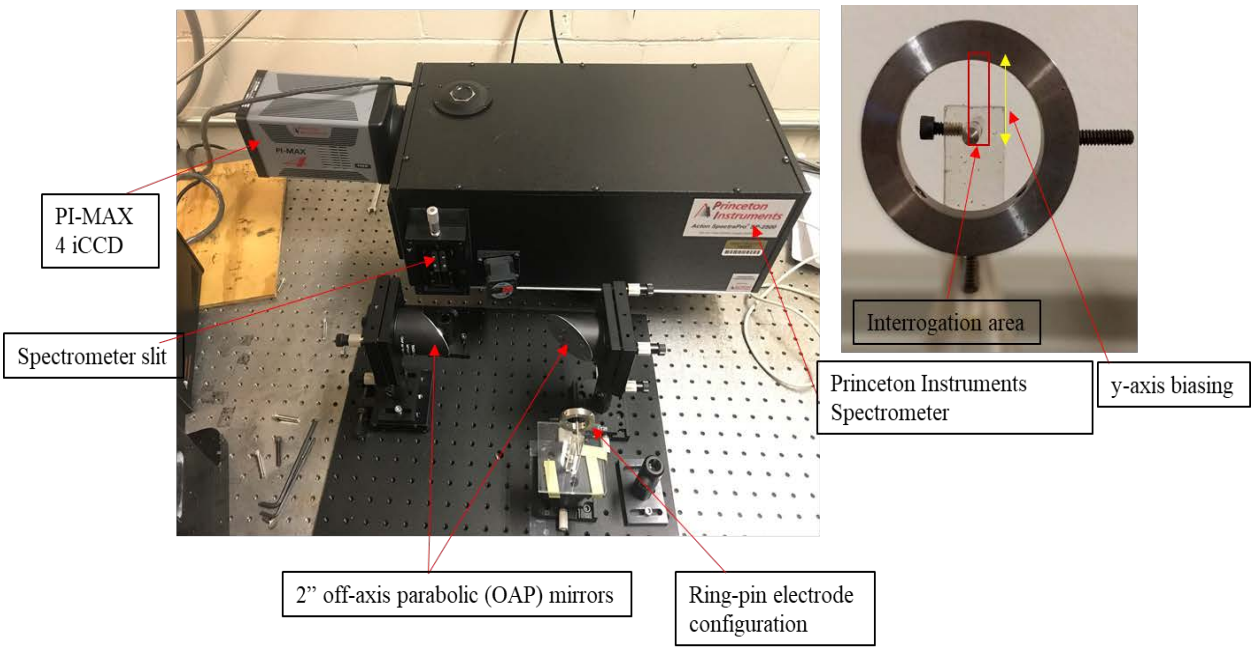

Figure 17: Setup for optical emission spectroscopy of the plasma.

2.3 High Pressure Plasma-Assisted Burner Development

The Purdue University Zucrow Lab supports large scale combustion experiments operating at relevant engine conditions. The facility is equipped with an air plant which provides continuous supply of dry, clean compressed air at up to 150 bars. Continuous supply of pre-heated air at 4 kg/s, 40 bars to 800 K is provided by a natural-gas fired heat exchanger. A secondary electric heat exchanger can provide additional pre-heated air supply at 40 bars to 950 K. Nitrogen is used for pneumatic controls, purges, and any other experiment needs. The facility is also equipped with flame-shield fuel containments for liquid fuel experiments with the capability to investigate standard aviation fuels and other blends. A summary of the available resources at the High-Pressure Lab, the location of the new high-pressure burner, is presented in Figure 18.

The plasma generation system will be integrated in Purdue's high-pressure Aviation Combustion Experiment (ACE) to characterize the plasma-flame coupling at elevated pressures. ACE is a high-pressure water-cooled windowed combustor used to investigate reacting flows at relevant engine conditions [34]. To date, ACE has 200 hours of run time with demonstrated application of advanced multi-kHz OH-PLIF, stereo and planar PIV, and other emission measurements. The test stand, shown in Figure 19 and Figure 20, provides translational capability for a variety of test articles to aid in quick assembly and disassembly. Data system capability is available with an extensive number of AI/AO/DO channels for data acquisition. It also features 32 channels with 180 kHz sampling rates for dynamic pressure. The combustion chamber is 230-mm long with a 105-mm square cross section and optical access through all four walls. It has a two-window design: a thin, inner window serving as the combustion chamber wall, while a secondary

thick outer window is used to contain the high operating pressures. The combustion chamber operates at chamber pressures up to 40 bars, 3 MW of thermal power, and inlet air temperatures up to 950 K. A photograph of the facility plumbing is presented in Figure 22.

To investigate the plasma-flame coupling and its effect on stability limits and flame dynamics, an injector design incorporating a ring-pin electrode configuration like that used in the atmospheric pressure burner, was designed as shown in Figure 21. The injector design will allow translational capability for the electrode configuration with respect to the burner outlet to study the effect of plasma location as well as different electrode gaps. A single element swirler, with vanes orientated at 60 degrees producing a swirl number of 1.26, will be used to impart tangential velocity to the air stream. Pre-heated air will be injected upstream of the burner face while the fuel (natural gas) will be injected normal to the air flow. High voltage feedthroughs with high temperature and pressure capability will be used to generate the plasma at the burner outlet. The plasma-flame coupling will be investigated at chamber pressures up to 10 bars with thermal flame power up to 1 MW. Upon fabrication, installation, and safety review, the effect of plasma discharge on flame morphology, structure, and stability limits will be investigated and compared to atmospheric pressure flame measurements.

Fluid System	*Fluid*	*Max. Pressure (bar)*	*Max. Flow Rate (per circuit) [kg/s]*
Bottled Gaseous fuels (FB01-04)	Methane/H_2/..	410	0.2
Natural Gas	Natural gas	250	7
Liquid Fuel Tank	Jet Fuel	100	0.16
Nitrogen	Nitrogen	410	1.4
Air Supply (un-heated) (AS01-02)	Air	138	23
Heated Air Supply- Circuit HS01	Air	55 (at 1090 K)	4.0
Heated Air Supply- Circuit HS02	Air/N_2	40 (at 800 K)	2.3
Heated Air Supply- Circuit HS03	Air/N_2	40 (at 920 K)	0.25
High Pressure Water (HPW)	Water	67	6.35
Low Pressure Water (LPW)	Water	7	3.0

Figure 18: High Pressure Lab at Purdue Zucrow Laboratory where the high pressure plasma-assisted burner will be located.

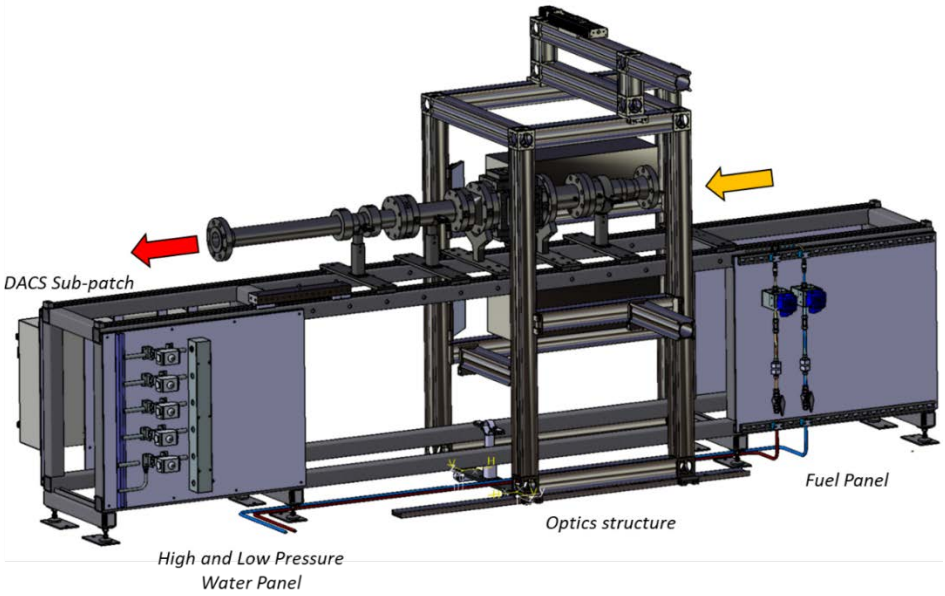

Figure 19: VIPER Test Stand and ACE assembly used for the high pressure plasma-assisted burner.

Figure 20: Photograph of the VIPER Test Stand with ACE assembly which will be used for the high pressure plasma-assisted burner.

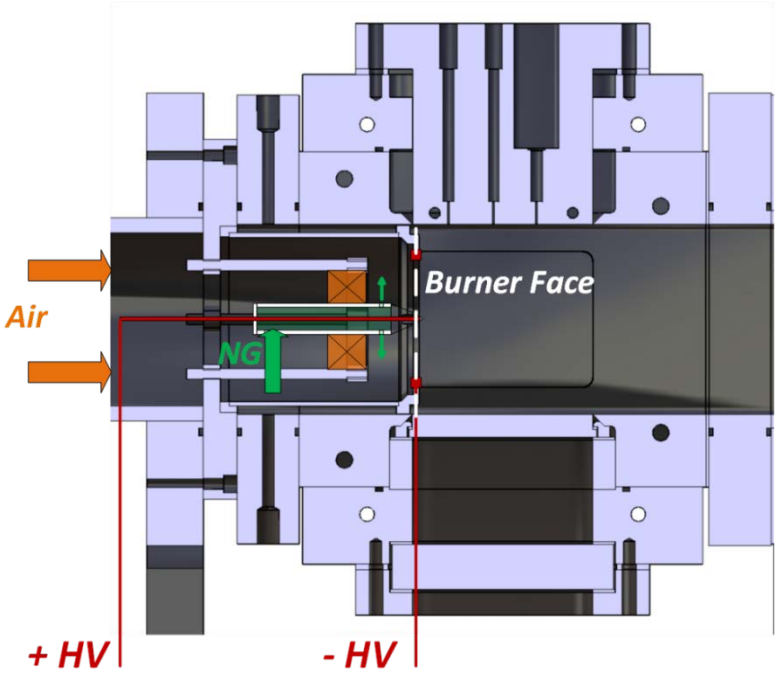

Figure 21: Preliminary Injector design with ring-pin electrode configuration.

Figure 22: HPL Test Cell 4 facility plumbing which will be used for the high-pressure plasma-assisted burner.

3. RESULTS & DISCUSSION

3.1 Plasma Generation

Previous work done by the author's colleague investigated the effect of pulse duration, polarity, pulsed repetition frequency (PRF), and peak voltage on plasma formation at atmospheric pressure using a similar electrode geometry but with a smaller (~ 11 mm) gap [35]. The results showed low PRF (1-10 kHz) and pulse durations (40-1000 ns) produced low intensity, diffuse plasma channels localized to an arbitrary sector of the annular electrode. Higher PRF (50 kHz) produced high intensity discharges which were confined to a small sector of the electrode plane. Increasing peak voltage and applying positive polarity to the inner electrode resulted in an increase in plasma emission intensity with more diffuse filaments at low and intermediate PRFs. The results of the previous study provided an optimal set of pulse parameters to efficiently generate the plasma using the electrode configuration shown in Figure 2. The electrode gap for is approximately 1.2-inch and is equal to the electrode gap on the atmospheric pressure burner. The plasma characterization provided insight on the plasma regimes to be produced to effect the flame.

For this significantly larger electrode gap, the highest peak voltage (20kV) capable on the nanosecond pulser was chosen with a positive polarity applied to the inner electrode pin. A fixed pulse width of 60 ns and PRFs in the range of 10 – 50 kHz were chosen to obtain as close to a homogenous plasma disk as possible. Images of the plasma generation for 5 different PRFs with burse duration of 50 and 100 ms are shown in Figure 23 and Figure 24. The burse duration is proportional to the number of pulses (inversely proportional to the repetition frequency) and the minimum number of pulses needed to break down the air in the larger electrode gap is 500 corresponding to a burse duration of 50 ms.

Figure 23 and Figure 24 show the plasma regimes (diffuse and filamentary) with corresponding electrical pulse parameters for burst durations of 50 ms and 100 ms. The plasma regimes are sensitive to electrode surface condition requiring higher breakdown voltage due the gradual erosion of the anode and cathode. For consistency, the electrodes were replaced often for high fidelity of measurements. The electrical properties for each burst duration are presented in Table 3 and Table 4. To obtain the energy deposited in the gap for one pulse, the voltage and current waveforms were multiped and then integrated in time over the pulse duration to yield energy deposited by that pulse. An example of the current and voltage waveform is shown in Figure 25. The total current is affected by the length of the cables and any surface contact from the cables and electrode fixture to the optics table. Therefore, the total current includes the conduction current and the displacement current which is observed as the initial rise in current in the current waveform shown in Figure 25 (left).

For a burst duration of 100 ms (Figure 23, Case B - E), the plasma discharges were mostly in the filamentary regime and confined to an arbitrary section of the electrode but spanned the entirety of the electrode gap. The peak voltage decreases with increasing PRF resulting in less electrical energy input due to residual charges remaining from the previous pulses. While the peak voltage

decreases as PRF increases, the peak current is much higher possibly due to the resistance in the gap having been reduced from the accumulation of previous charges thus requiring less voltage to achieve breakdown. The discharge for this regime created a crackling sound with visibly high intensity. For low PRF (Case A – 10 kHz, 1000 pulses), a diffuse discharge was produced spanning only a fraction of the annulus. More total electrical energy is deposited in this regime than in the localized filamentary plasma and this result is consistent over all pulse parameters tested. The effect of the accumulation of previous charges from a high number of pulses is reduced significantly at low PRFs, the resistance in the electrode gap remains high and a significant amount of energy is required for breakdown.

For the 50 ms case, similar conclusions can be made. Figure 24 (Case A – 10 kHz, 500 pulses) shows a similar diffuse discharge with high energy and the associated current is shown in Table 4. In image B (20 kHz, 1000 pulses), we observed a more transitory regime where the discharge appears to be both in the diffuse to filamentary regime. Bright filamentary plasma channels are observed. As the number of pulses and PRF increase, the plasma is fully in the filamentary regime and the electrical properties are similar to that of the 100 ms case. It was also observed that the current remains relatively constant if the discharge remains in the same regimen i.e. diffuse or "spark" (filamentary). This implies that the plasma discharge regime is independent of frequency once the regime has been established. A study done by Pai et al. reported similar transition regimes for measurements performed in heated air with pin-pin electrodes with a maximum electrode gap of 10 mm [36].

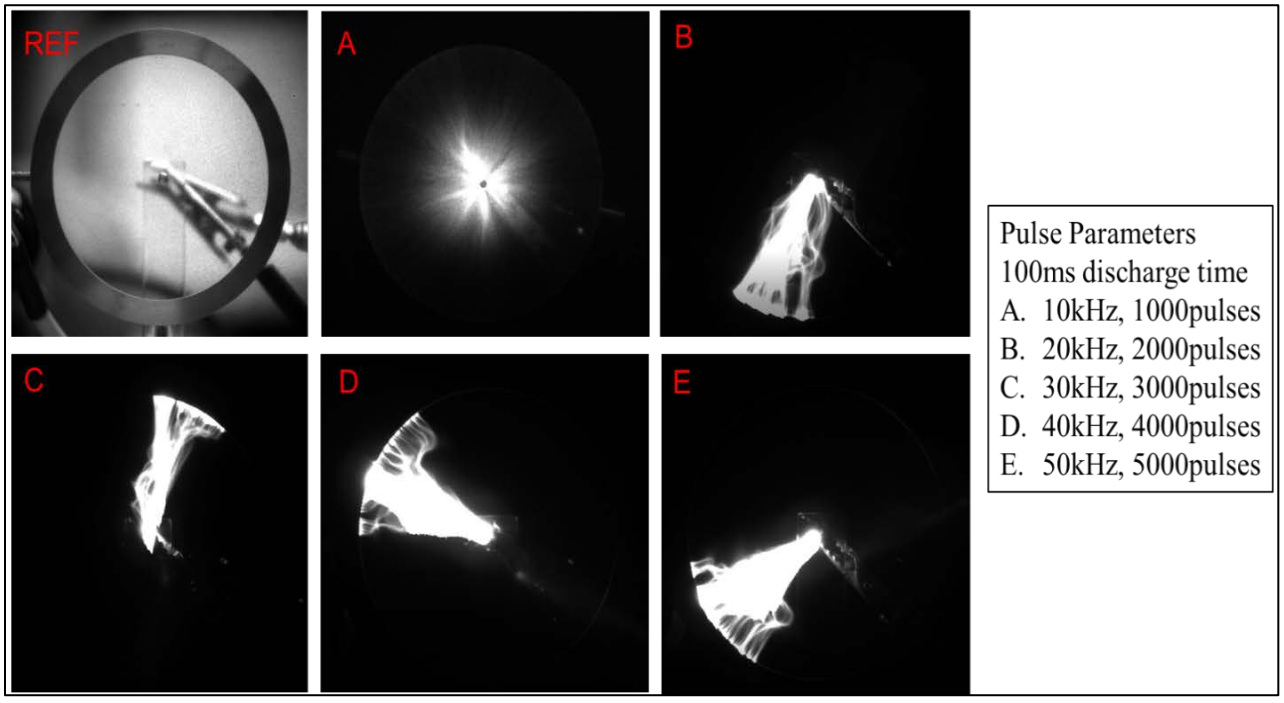

Figure 23: Plasma regime for the larger (~30.48 mm) electrode gap. The images were obtained using an ICCD camera 100 ms for 10, 20, 30, 40, and 50 kHz to capture 1000, 2000, 3000, 4000, and 5000 pulses.

Table 3: Peak current, peak voltage, and energy measurements for different pulse bursts in the larger (~ 30.48 mm) electrode gap for 100 ms burst duration.

PRF (Hz)	Pulses	Peak Current (A)	Peak Voltage (kV)	Energy of last pulse (mJ)
10000	1000	17.70	26.44	17.4
20000	2000	28.11	21.40	9.5
30000	3000	30.14	17.46	7.5
40000	4000	29.39	19.49	8.2
50000	5000	29.35	15.70	7.3

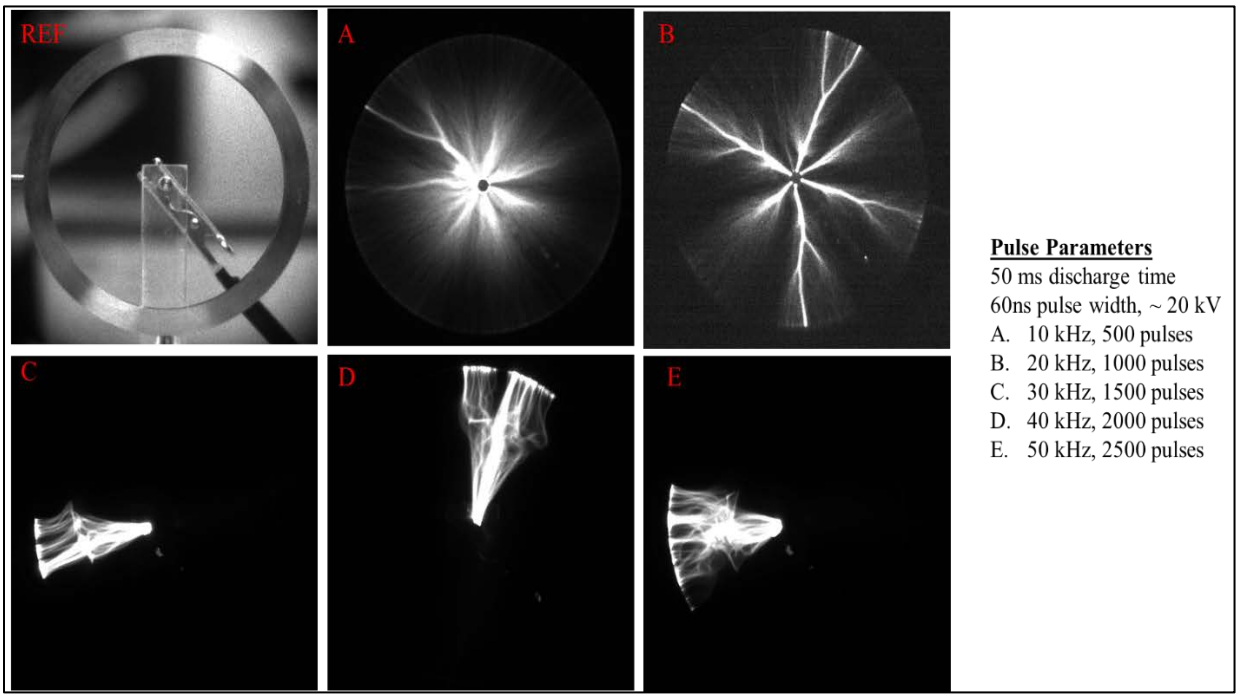

Figure 24: Plasma regimes for the larger (~ 30.48 mm) electrode gap at 50ms pulse burst duration. The images were obtained using an ICCD camera with a gate width of 50 ms to capture 500, 1000, 1500, 2000, and 2500 pulses at PRFs of 10, 20, 30, 40, and 50 kHz respectively.

Table 4: Peak current, peak voltage, and energy measurements for different pulse bursts in the larger (~ 30.48 mm) electrode gap for 50 ms burst duration.

RPF (Hz)	Pulses	Peak Current (A)	Peak Voltage (kV)	Energy of last pulse (mJ)
10000	500	10.97	25.56	18.0
20000	1000	48.19	23.28	12.6
30000	1500	57.54	19.46	11.4
40000	2000	23.50	25.37	6.9
50000	2500	56.87	15.69	9.7

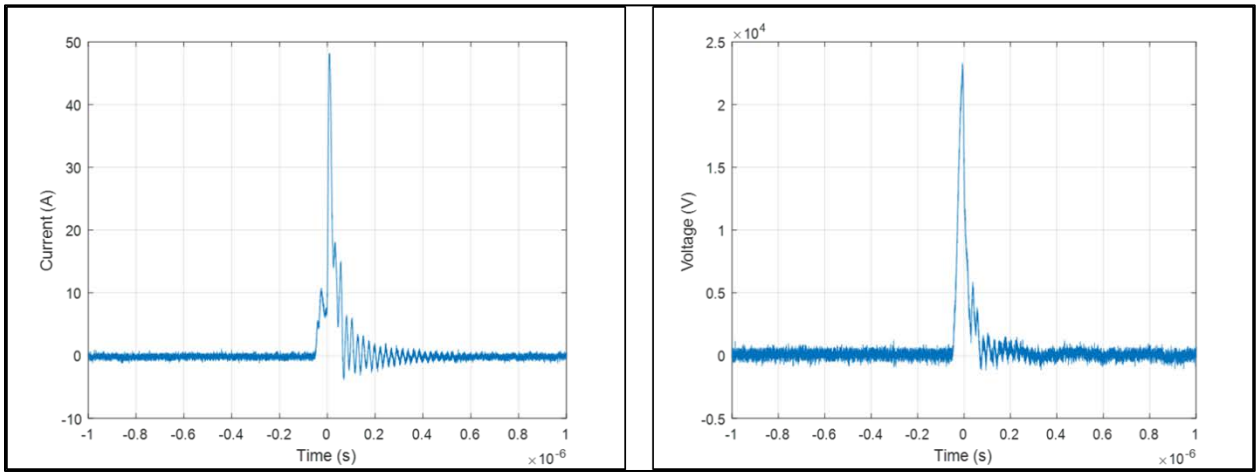

Figure 25: Example current and voltage waveforms for discharge time of 50 ms at PRF of 20 kHz (1000 pulses).

3.2 High-Speed Schlieren Visualization

Plasma discharges can induce local flow fields which can be quite complex to study or measure in detail. The three primary mechanisms by which the plasma discharge can induce local flow fields are: 1) electrostatic or electrohydrodynamic (EHD), 2) magnetohydrodynamic (MHD), and 3) thermal. In the EHD and MHD mechanism, a body force is produced, acting on the flow and results in very low velocity bulk motion of the fluid. In the thermal mechanism, the temperature rise in the plasma, caused by joule heating and relaxation of internal energy states, induces thermal perturbations in the flow. The plasma can generate compression waves and subsequent local flow fields. This induced flow field was predicted to likely influence the combustion and flame dynamics.

The schlieren technique shown in Figure 5 allows for qualitative visualization of the density gradients in the induced flow from the discharge. The visualization is conducted using two viewpoints: perpendicular to the electrode gap and front-on view of the gap. An ICCD camera is used to capture long exposure images of the discharge to aid in interpreting the schlieren images. The images in Figure 26 (diffuse regime) are for a discharge with PRF of 10 kHz for a total discharge time of 100 ms. The images in Figure 27 are for a discharge with PRF of 50 kHz for a total discharge time of 50 ms (filamentary regime).

For the diffuse discharge case (Figure 26), modest heating of the gas by the discharge channels is observed in the schlieren images, and weak shock waves emitted due to the rapid heating are visible. The shock waves also induce a small local flow. The magnitude of the induced local velocity is assumed to be weak and this discharge will likely aid in altering the chemical kinetic pathways in the flame. The induced flow field from this plasma discharge is due to the EHD and MHD mechanisms. As the number of pulses increased at higher PRFs to produce more filamentary discharges (Figure 27), the gas heating is significantly higher, resulting in stronger induced shock waves and a higher degree induced flow. The filamentary discharge also induces a high degree of vorticity and fast gas mixing. The induced flow field from this discharge is best characterized by the thermal mechanism. The magnitude of the induced local velocity is hypothesized to be significantly higher than the flame speed and was measured for a similar discharge in Section 3.3.

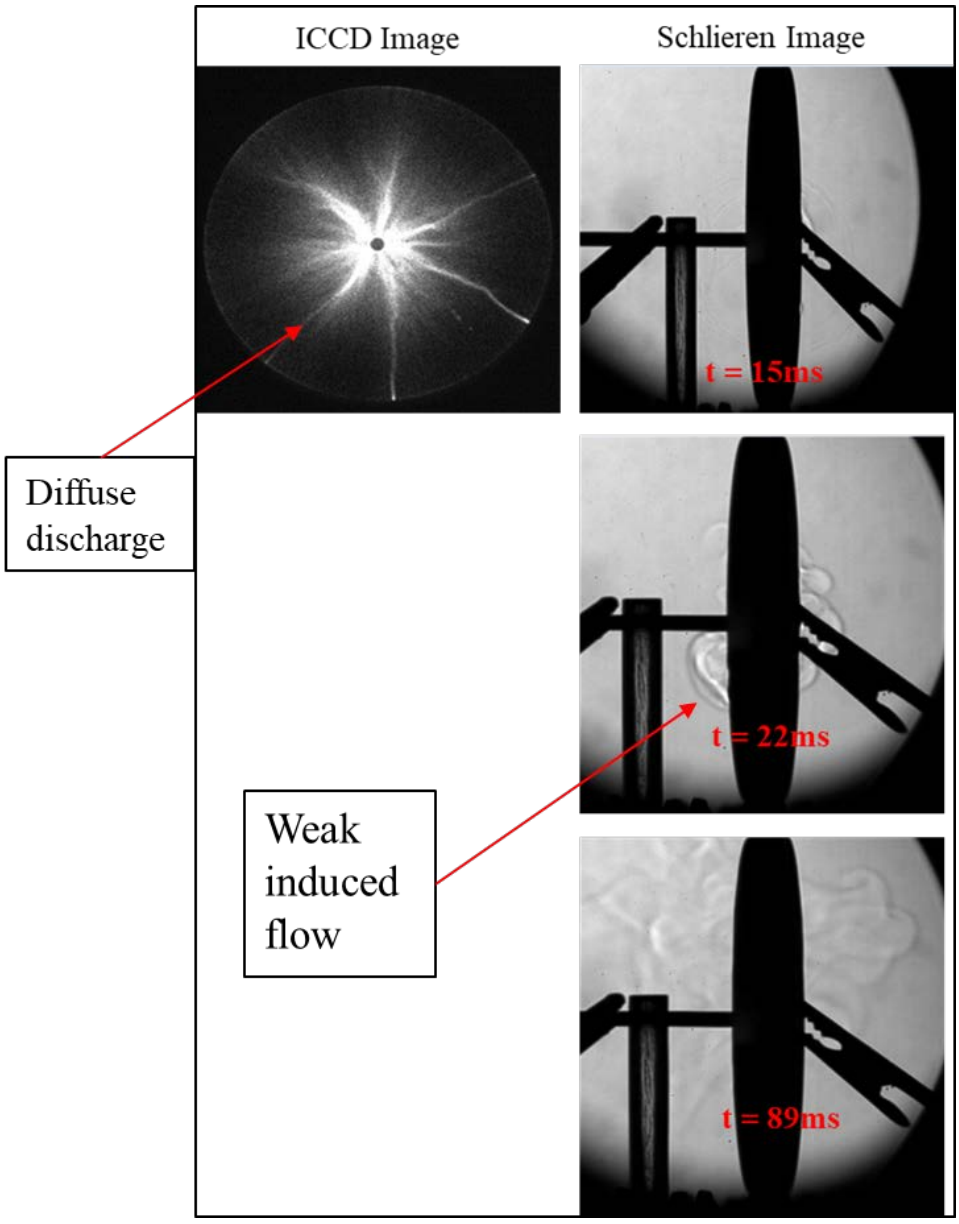

Figure 26: Schlieren imaging of the gas heating and induced flow field produced by a diffuse plasma discharge in a ring-pin electrode geometry (gap length of 1-3/16-inch, atmospheric pressure) for burst duration of 100 ms.

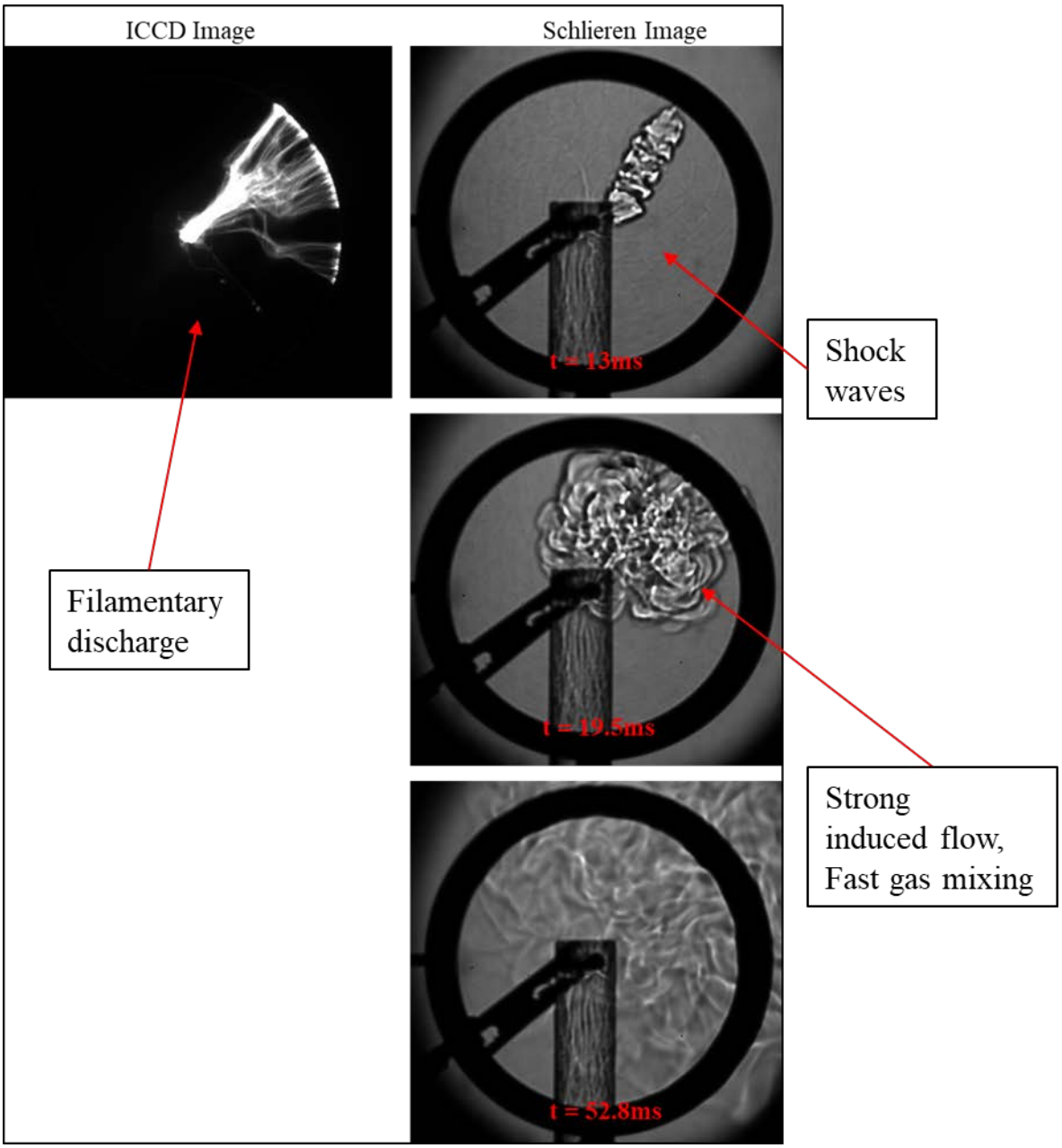

Figure 27: Schlieren imaging of the gas heating and induced flow field produced by a filamentary plasma discharge in a ring-pin electrode geometry (gap length of 1-3/16-inch, atmospheric pressure) for a burst duration of 50 ms.

3.3 Particle Image Velocimetry

The particle image velocimetry setup shown in Figure 6 was used to quantify the local velocity induced by the plasma discharge. The goal of this work was to simply perform preliminary investigation to quantify the magnitude of the induced flow velocity by the plasma discharge and limited experiments were performed. Previous work by the author's colleagues is solely based on the pin-pin configuration and the flow induced in this electrode configuration is significantly more complex than that generated in a pin-to-pin configuration by a single pulse [37]. Thus, further refinements to the PIV processing techniques used for this electrode configuration are ongoing. The vorticity and degree of mixing generated by the discharge is also currently being investigated.

Typically, PIV recordings are subdivided into interrogation areas during evaluation from which the velocity vectors are determined. In this electrode configuration, a two-dimensional plane, through the front view of the electrode gap, was identified focusing on the area around the inner electrode. This interrogation region was chosen to ensure the discharge is captured considering the discharge is formed at arbitrary locations along the annular electrode. The areas in the images containing the plasma discharge were removed to eliminate the non-uniformity of the particle image intensity shown in the left image of Figure 28. Universal outlier detection was performed on the images of interest to present validated vector fields [38]. The velocity vectors presented are for a plasma discharge at 4000 pulses and PRF of 40 kHz. This discharge is characterized by high intensity filaments that are constricted to a sector of the annular electrode with significant induced flow. Initial results show significant induced flow entrained to the location of the discharge with absolute velocity on the order of 15 m/s. Laminar flame speed for stoichiometric methane-air flames are on the order of 40 cm/s [39] further confirming the strong effect of the plasma discharge on the local flow field.

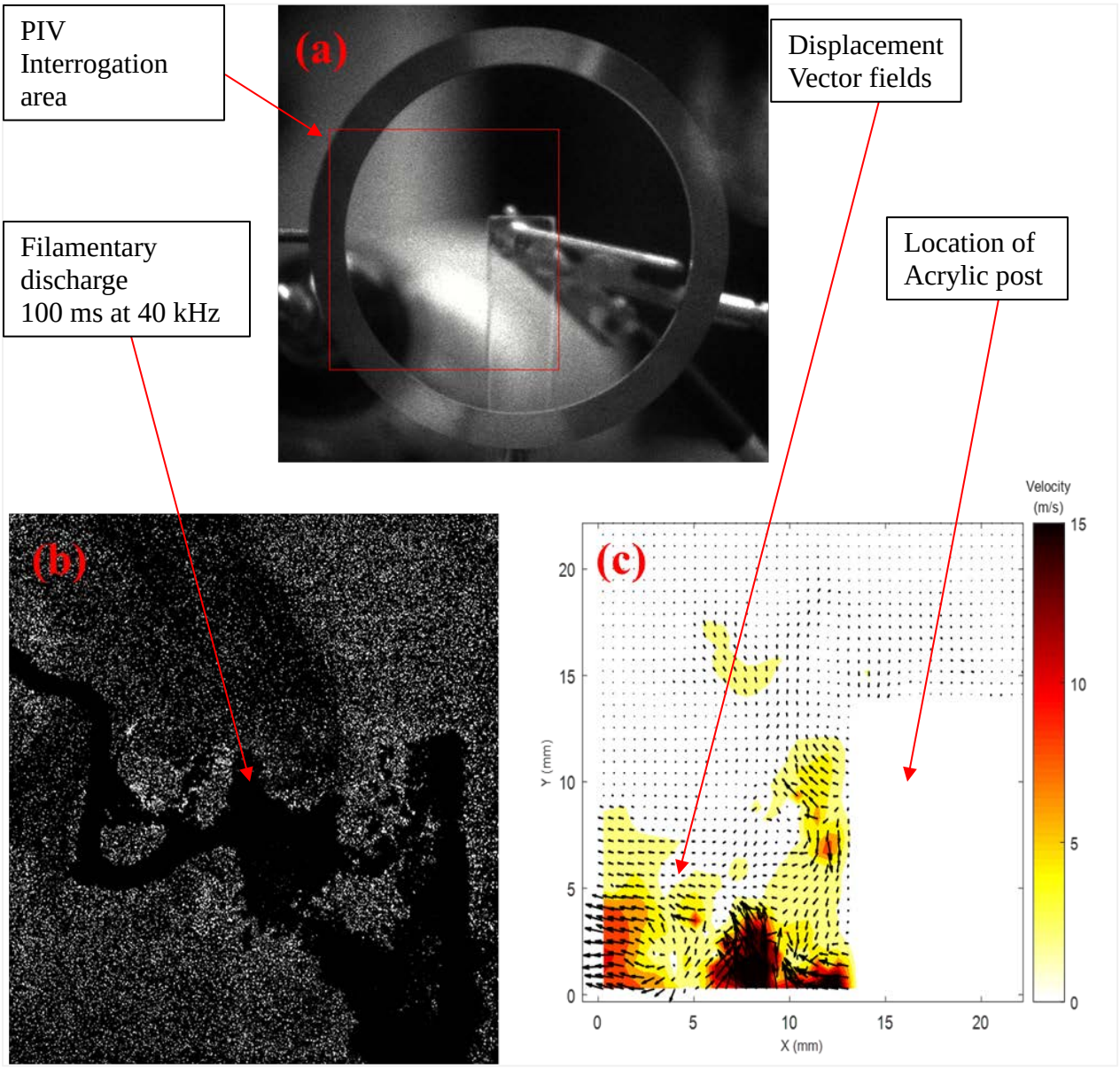

Figure 28: PIV measurements of local flow velocity induced by the plasma discharge with pulse parameters of 40 kHz, 4000 pulses, and burst duration of 100 ms, taken at 50 µs. (a) Field of view for PIV; (b) particle images; (c) velocity vectors obtained from PIV analysis.

3.4 Gas Temperature

The rise in the gas temperature induced by the plasma is an important parameter as it can strongly affect the combustion chemistry and induce complex local flow fields that enhance mixing. The second positive system of nitrogen, shown in Figure 29, is typically used to determine the rotational and vibrational temperatures in air plasma discharges by analyzing and detecting the

emission with a spectrometer. In the current work, the plasma temperature of distributed filamentary discharges generated at PRFs of 5, 10, 20, 50 kHz was deduced from the $N_2(C\,^3\Pi_u–B\,^3\_\Pi_g)$ spectrum with to 250, 500, 1000, 2500 accumulations (pulses), respectively. The temperatures were determined by fitting the experimental spectra with theoretical spectra as shown in Figure 30. Figure 31 shows how the nitrogen temperature evolves as PRF varies for a total burst duration of 50 ms. These measurements were obtained using a smaller electrode fixture with an electrode gap of 11 mm and the plasma discharge was in the filamentary regime. For the low PRF cases (5 – 10 kHz), the plasma regime was similar to that seen in Figure 24 (Case B) with thin, moderately luminous channels spanning the entirety of the electrode gap. As the PRF increased, the plasma discharge was in the filamentary regime as expected.

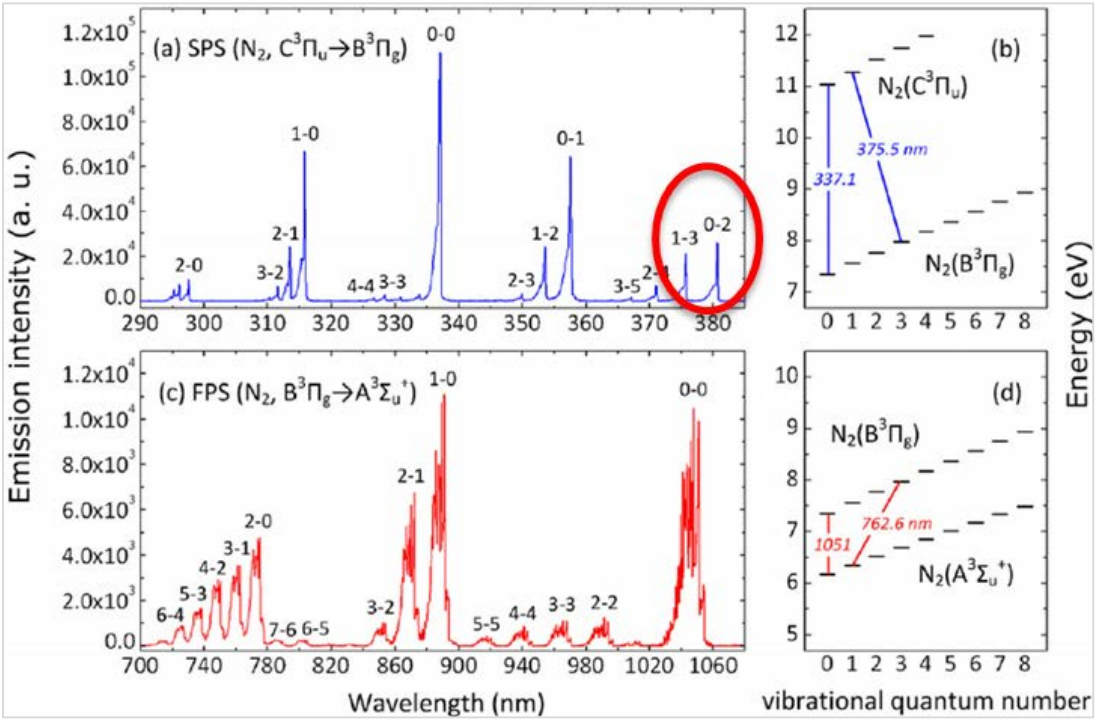

Figure 29: Nitrogen second positive system – second overtone (in red).

For a PRF of 5 kHz, the average rotational and vibrational temperatures are 576 K and 4172 K, respectively. The vibrational temperature was fairly independent of PRF for 5 and 10 kHz increasing only by 16 K. The rotational temperature increased from 576 K to 1177 K, higher by a factor two. The modest heating in the vibrational temperature supports the hypothesis that low PRF plasma discharges are dominated primarily by the EHD mechanism which is driven by bulk motion of the fluid with minimal gas heating in Section 2.1.1. The vibrational and rotational temperature increased moderately at 20 kHz by a difference of 1000 K. For the 50 kHz case, the rotational and vibrational temperature increased by a factor of 2 and 3, respectively, from the 20 kHz case. These discharges were in the filamentary regime where the primary mechanism is the

thermal mechanism which is characterized by local heating. As the PRF increased, the peak discharge current is much higher, likely due to the resistance in the gap having been reduced from the accumulation of previous charges, thus increasing both rotational and vibrational temperatures. More collisions occur under these conditions, and the nitrogen molecules vibrate, rotate, and move to higher levels of energy. In addition, the relaxation process of vibrationally excited states of N_2 is a slow process, longer than the time required for plasma-assisted ignition (10-100 μs) [40]. For a discharge at 50 kHz with 2500 pulses, each pulse is 20 μs long so the vibrational temperature remains high well after the emission from the breakdown pulses was captured. The gas temperature will also be investigated in the larger electrode which is used in the atmospheric pressure burner. Further measurements of the temperature distribution and species concentrations in the plasma discharge in the ring-pin electrode configuration will be obtained to investigate mechanisms for affecting the flame.

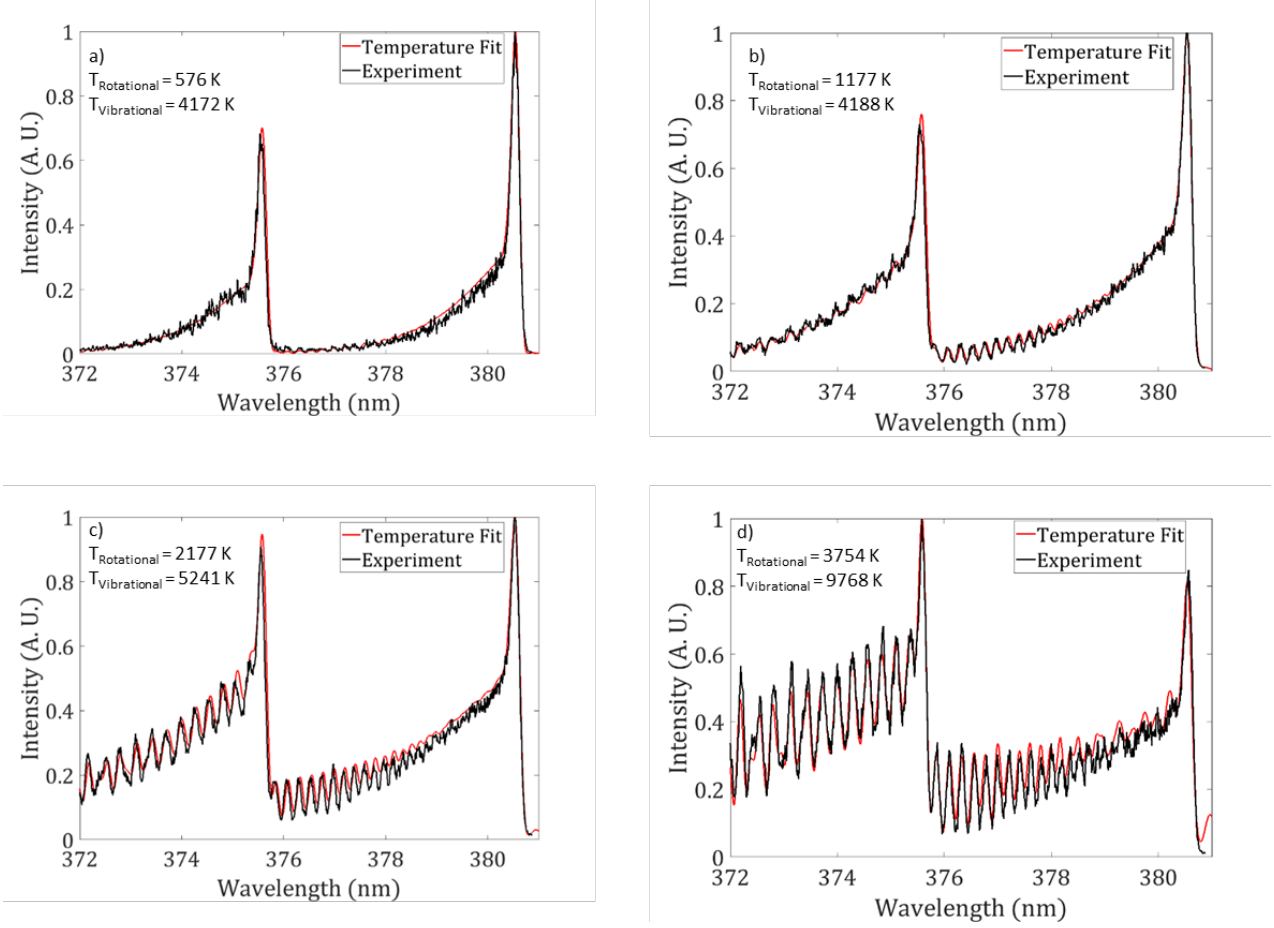

Figure 30: Experimental calibrated spectrum and theoretical simulated spectrum of the N_2(C→B) transition between 372 and 382 nm for PRFs of 5, 10, 20, 50 kHz with 100 ns exposure.

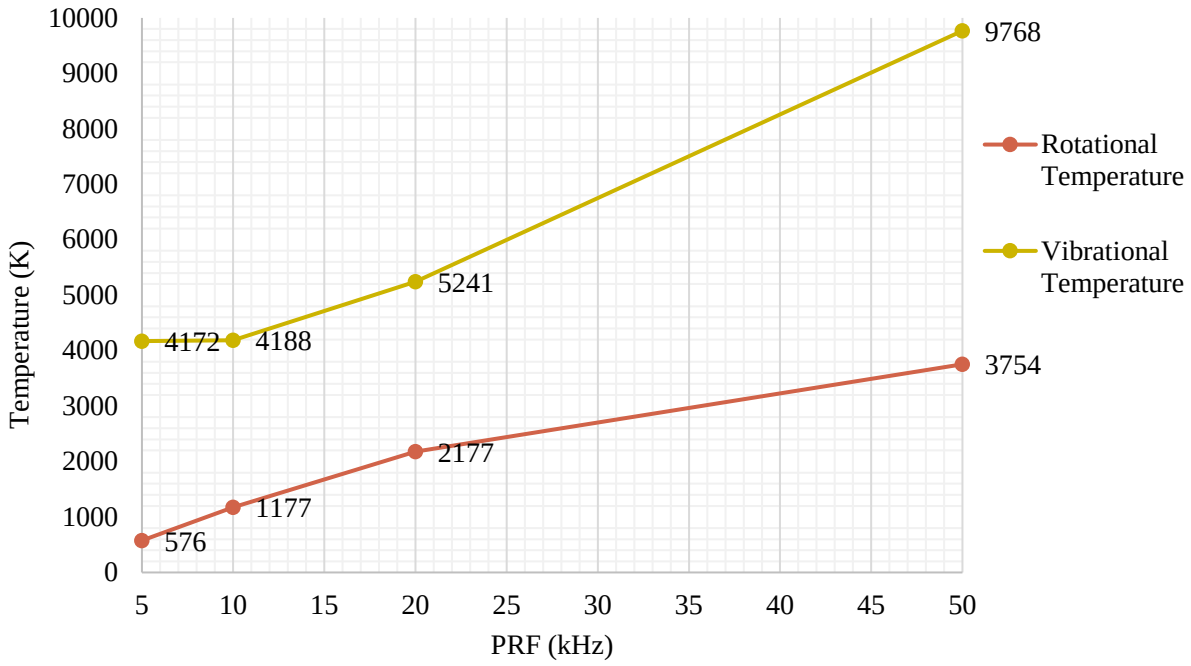

Figure 31: Gas temperature as a function of pulse repetition frequency measured from the N_2*(C→B)* transition.

3.5 Atmospheric Pressure Burner Characterization

3.5.1 Chemiluminescence of Laminar Bunsen Flames

To begin characterizing the burner, we first employ a very simple diagnostic: visualization of the flame chemiluminescence, which is primarily produced by electronically excited species such as CH*, C_2*, and OH*. Specifically, CH* chemiluminescence is used to study flame response and estimate the flame front location. CH* is produced by the following reaction [32]:

$$C_2 + OH = CO + CH^*$$

For these sets of images, a 1-inch stainless-steel insert was fabricated to effectively reduce the burner exit area to generate a laminar Bunsen flame. This allowed us to investigate a simple, more modest flame prior to extending the technique to swirl flames at much higher flow rates. Images of CH* chemiluminescence of a lean premixed methane-air flame were obtained at 10 fps using a Princeton instruments PI-MAX4 1024i intensified CCD camera. The exposure on the camera was set to 300 microseconds with a gain of 62. The intensifier gate time must be sufficient to provide adequate signal-to-noise ratio for high quality images. Figure 32-35 show the flame structure at varying equivalence ratios and air flowrate of 12 LPM. The raw images of the flame capturing all emission wavelengths are presented on the left, and the filtered images on the right. For these conditions, the flames were thermally stabilized at the burner outlet. The flame structure changed

significantly with the CH* bandpass filter and the CH* emissions from the flame appears to be more compact and is concentrated near the bottom of the flame which is indicative of flame front location. As the equivalence ratio decreases, the CH* emission from the flame is significantly reduced due to the decrease in methane flow rate as seen in Figure 34. These initial measurements provided insight on how to apply this technique to higher flow rates in the swirled configuration of the burner.

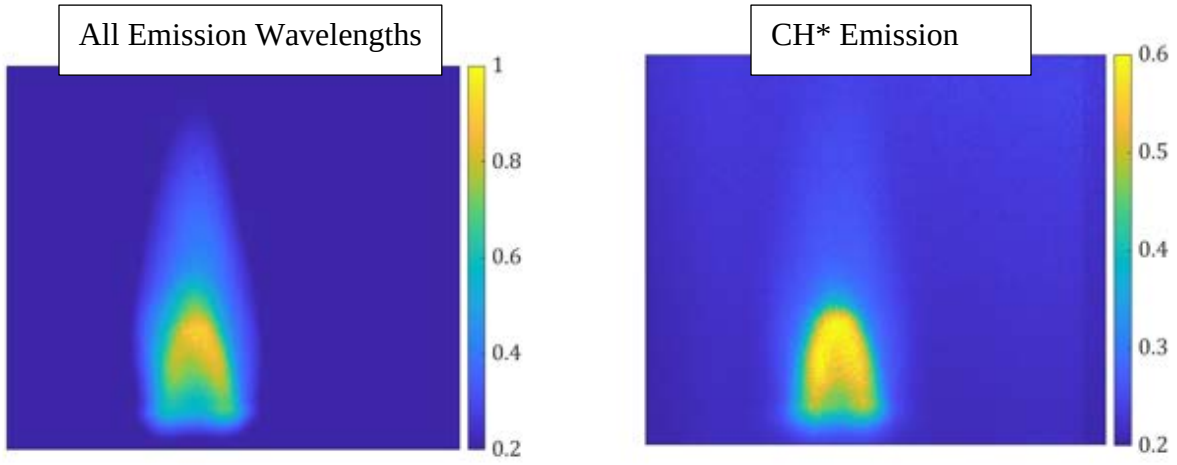

Figure 32: Images of a lean (ϕ = 1.26) methane/air Bunsen flame obtained using a Princeton instruments PI-MAX4 1024i intensified CCD camera at 10 fps with 300 μs gate.

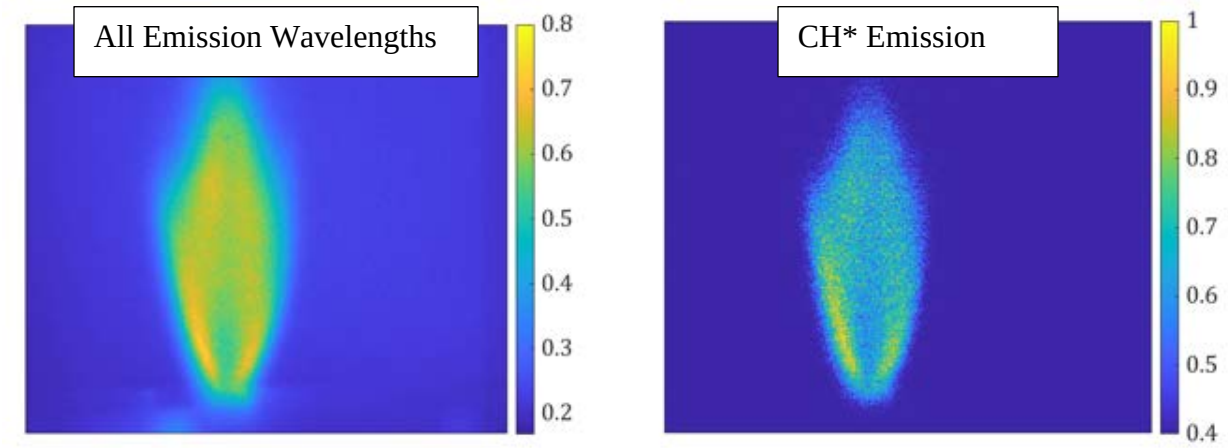

Figure 33: Images of a lean (ϕ = 0.8) methane/air Bunsen flame obtained using a Princeton instruments PI-MAX4 1024i intensified CCD camera at 10 fps with 300 μs gate.

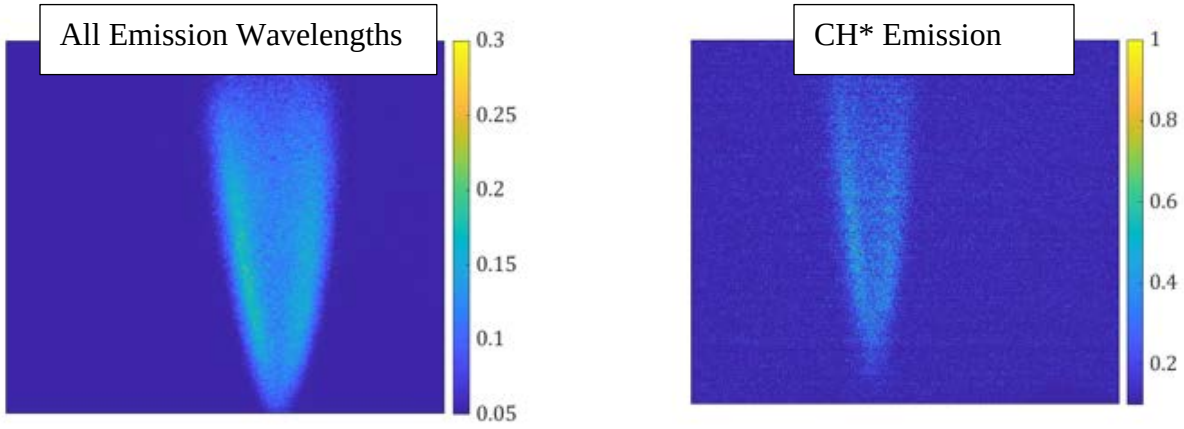

Figure 34: Images of a lean (ϕ = 0.55) methane/air Bunsen flame obtained using a Princeton instruments PI-MAX4 1024i intensified CCD camera at 10 fps with 300 μs gate.

3.5.2 Chemiluminescence and Dynamics of Swirled Flames

The blow-off limits of the flame were investigated without the plasma to characterize the burner. The 1.5 in. swirler and insert were used for these series of tests. A series of images of a lean methane/air flame with an air flow rate of 250 SLPM and an equivalence ratio of 0.86 were recorded with the ICCD camera and CH filter to visualize the flame zone. The thermal power for this flame is 12.3 kW, assuming 100% combustion efficiency with a Reynold's number of approximately 10,000. Figure 35 shows flame images from frames 1, 10, 20, 30, 40, and 50 with a 2 second time step for every 10 frames. The frames are randomly selected to show the extent of flame lift off above the electrode. This flame is highly turbulent, oscillates within the quartz tube confinement, and stabilizes approximately 53.34 mm above the electrode. This liftoff height, measured from the tip of the electrode, is based on a post processing calibration of 0.167 mm/pixel. At 250 SLPM, the blow-off limit occurs at an equivalence ratio of 0.80. Similarly, a series of images (same frame numbers) of a lean methane/air flame with an air flow rate of 150 SLPM and an equivalence ratio of 0.79, is shown in Figure 36. The thermal power for this flame is 6.85kW, assuming 100% combustion efficiency with a bulk Reynold's number of approximately 6,000. We observed this flame to be less turbulent than the previous 250 SLM case. The average liftoff height is approximately 48.51 mm above the electrode. At 150 SLPM, the blow-off limit occurs at an equivalence ratio of approximately 0.78. The blow-off height for the conditions investigated is approximately 50.8 mm above the flame anchoring location. The NRP plasma discharges are expected to improve these limits allowing the burner to operate at lower equivalence ratios.

Direct imaging of the ignition kernel formation, flame flashback, and blow-off were investigated using a Photron SA4 camera at 8,000 fps with an exposure time of 0.125 ms. The camera was used with a 50 mm lens with an *f*-number of 1.8. Figure 37 shows the ignition kernel development for the same flame as shown in Figure 35 (ϕ = 0.86, 250 SLPM). We show a sequence

of images corresponding to a 3.75 ms time step in images a through f. Upon ignition by a propane torch, a clear ignition kernel is formed and subsequently travels down towards the burner outlet where a self-sustaining flame is achieved.

Figure 38 shows the development of the flame attachment for the same conditions as Figures 31 and 33 (ϕ = 0.86, 250 SLPM) from a sequence of images with 12.5 ms time step. At sufficiently high equivalence ratios or when the quartz chamber is considerably hot, flames can become attached to the swirlers. This occurs because the swirlers are printed from plastic and the substantial heat release was is conducted away and thus the flames become susceptible to flashback/attachment. In the kernel formation condition shown in Figure 37, the burner was started under cold conditions. However, flame attachment was observed after the burner had been operating for a wide range of tests (several minutes). In the future, we intend to transition to metallic swirlers to mitigate flame attachment issues and extend flame attachment limits to higher equivalence ratios. The operating envelope for the burner with the 1.5 in swirler and insert is summarized in Table 5.

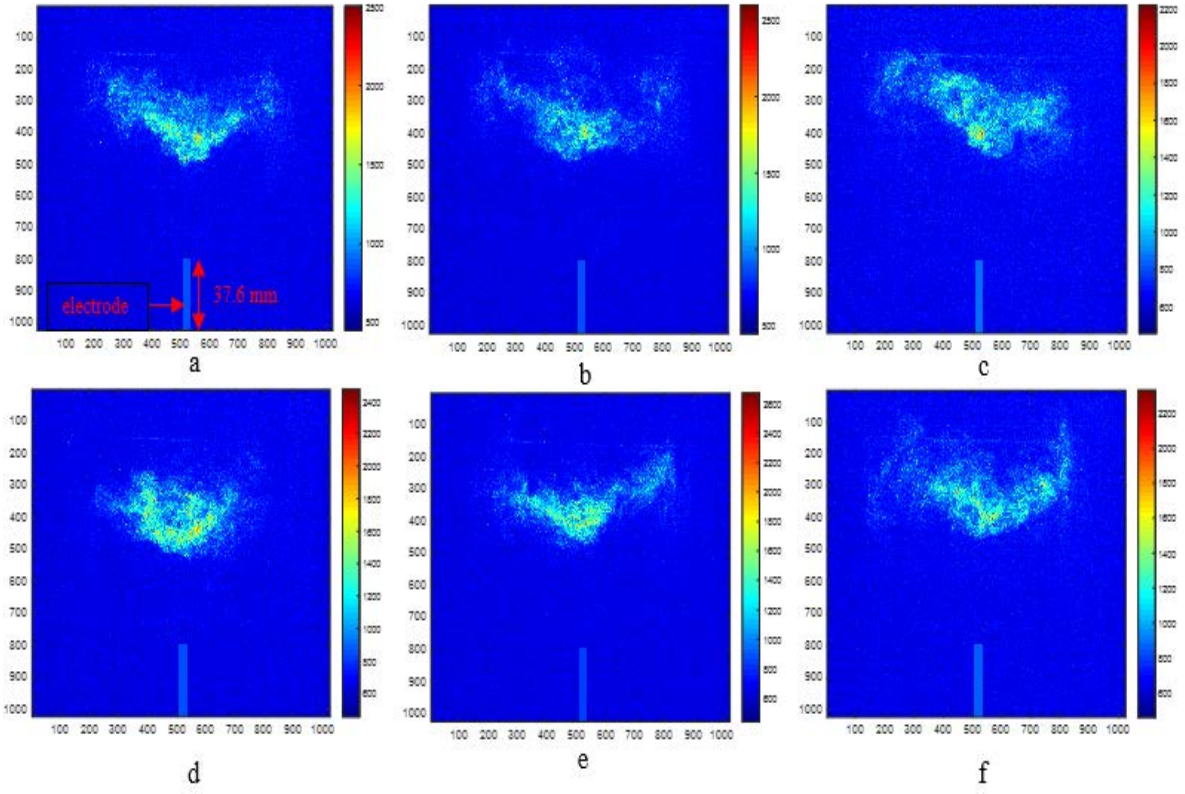

Figure 35: Images of CH* chemiluminescence of a lean (ϕ = 0.86, 250 SLPM) methane/air flame obtained using an ICCD camera with filter at 5 fps with 500 µs exposure and a 2 second time step between images.

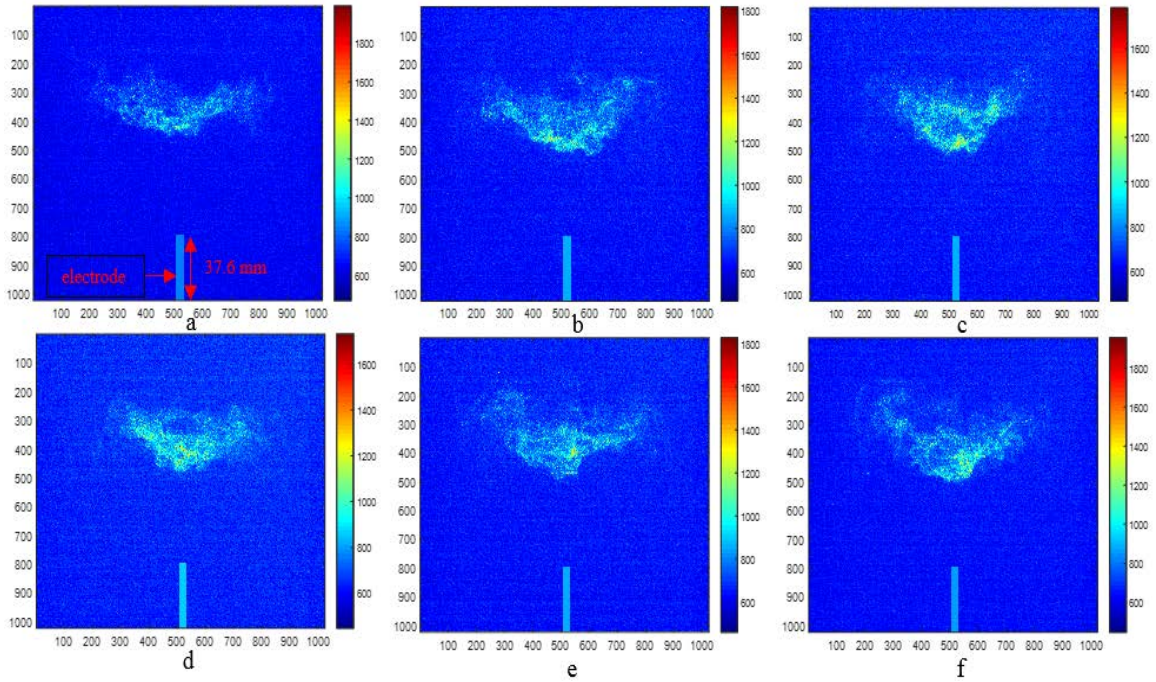

Figure 36: Images of CH* chemiluminescence of a lean (ϕ = 0.79, 150 SLPM air) methane/air flame obtained using an ICCD camera with filter at 5 fps with 500 µs exposure and a 2 second time step between images.

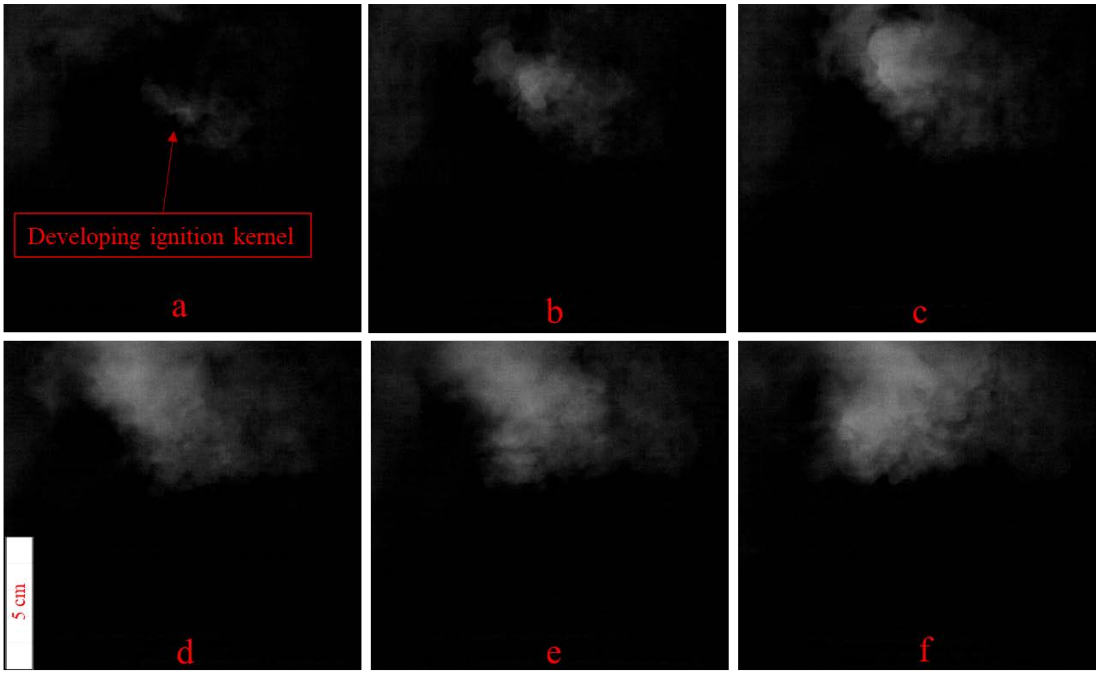

Figure 37: Images of a lean (ϕ = 0.86, 250 SLPM) methane/air flame ignition kernel formation obtained using a high-speed camera at 8,000 fps with an exposure time of 0.125 ms and a 3.75 ms time step between images.

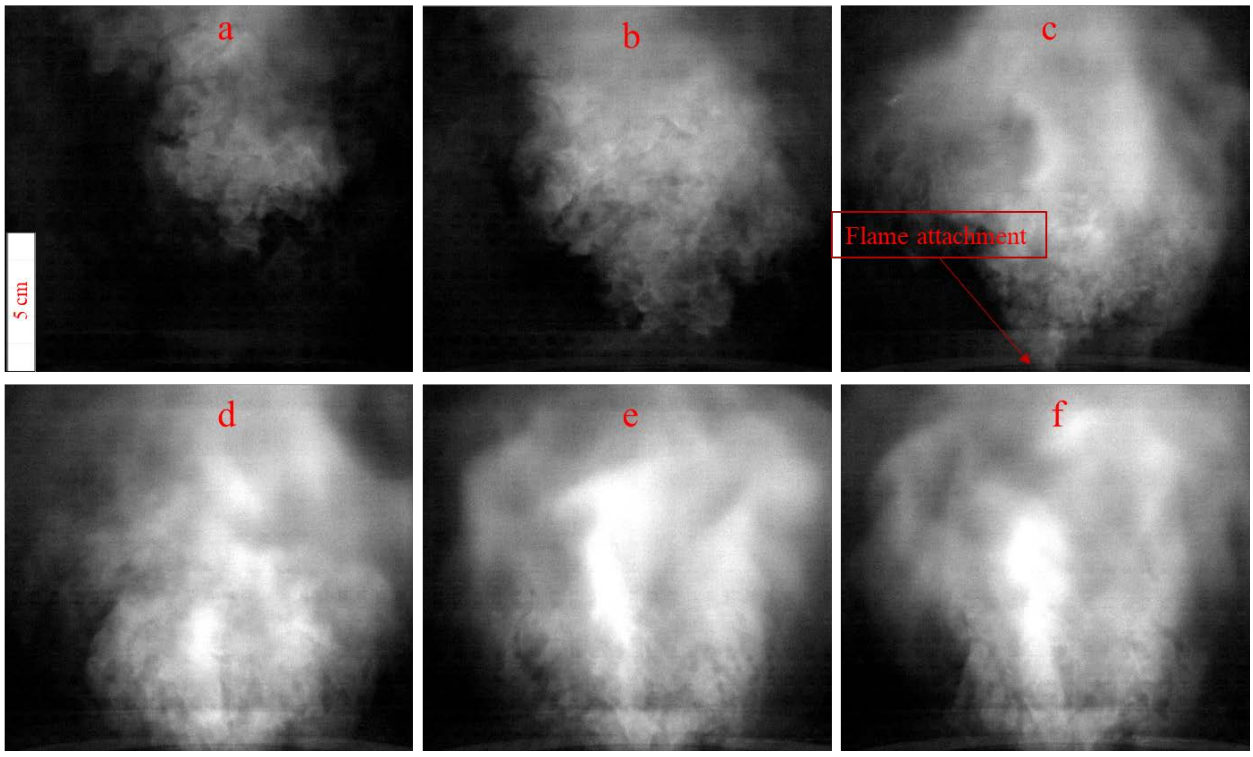

Figure 38: Images a lean (ϕ = 0.86, 250 SLPM) methane/air of attached flame obtained using a high-speed camera at 8,000 fps with an exposure time of 0.125 ms and a 12.5 ms time step between images.

Table 5: Burner Operating Envelope for the 1.5inch swirler design

Air Flow Rate (SLPM)	Thermal Power (W)	Bulk Re
300	13786	12020
250	11201	9997
200	8731	7982
150	6807	6004

3.5.3 Liftoff Height Measurements of Swirled Flames

Flame liftoff height was measured to further characterize the burner to understand its operating conditions. To obtain the liftoff height, a series of images were taken using a high-speed SAZ camera coupled with a LaVision intensifier at 60 frames per second. A MATLAB code (Appendix

B) was developed to extract how the flame anchor location changes for a given condition. The videos were converted to TIFF images and a vertical line was superimposed on each image to obtain their respective intensity profiles, as shown in Figure 39. A calibration dot card (Figure 40) was used to approximate the calibration factor (in inches/pixel) and once the bottom of the flame was determined, the calibration factor was used to determine how high the flame is with respect to the bottom of the image to calculate the flame liftoff height. A series of histograms obtained from a sequence of 500 - 600 consecutive images at 60 frames per second is presented showing the stability of the flame. The effect of equivalence ratio and flow rate is presented in Figure 41 - 47.

The effect of equivalence ratio with constant air flowrate is presented in Figure 41 - 44. We begin with Figure 41 for an air flow rate of 250 SLPM and an equivalence ratio of 0.69. The mean liftoff height was 2.14 inches from the burner exit plane and this condition is the near blow off limit in the burner's operating envelope. The mean liftoff height decreased to 1.95 inches above the burner as the equivalence ratio increased to 0.72. As the equivalence ratio increased further, near the flame attachment limit for this air flow rate, the mean liftoff decreased by 15%. Beyond an equivalence ratio of 0.75, the flame speed has increased significantly for the flame to thermally stabilize at the burner exit plane. A recent study by Liao et al. [41] confirmed the application of the plasma discharges to lifted flames decreases the flame liftoff height and thermally stable plasma-assisted flames were observed at the burner exit.

Figure 45 and Figure 46 present the effect of flowrate with constant equivalence ratio. The mean liftoff height for an air flow rate of 200 SLPM and an equivalence ratio of 0.69 is 2.0 inches. As the air flow rate increased, the mean liftoff height was 2.14 inches above the burner exit plane. Increasing the flow rate further resulted in flame blow off as expected. The flame speed for this condition remained constant and the application of the plasma discharge would be beneficial in this condition to prevent flame blow off. The standard deviation for all histograms is within 7 - 13% and the mean liftoff height distribution is clustered around 2.0 inches indicating the flame is consistently stable above the burner exit plane.

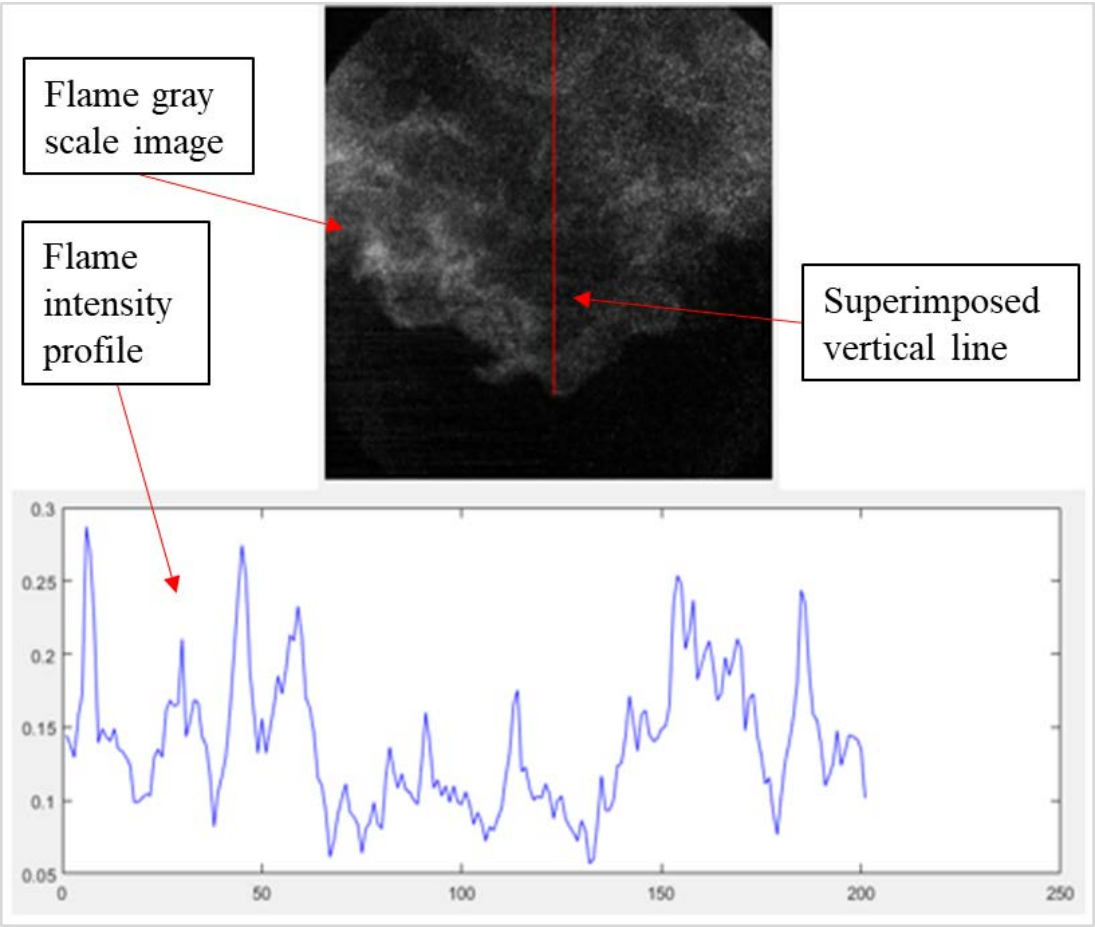

Figure 39: Flame intensity profile to measure liftoff height.

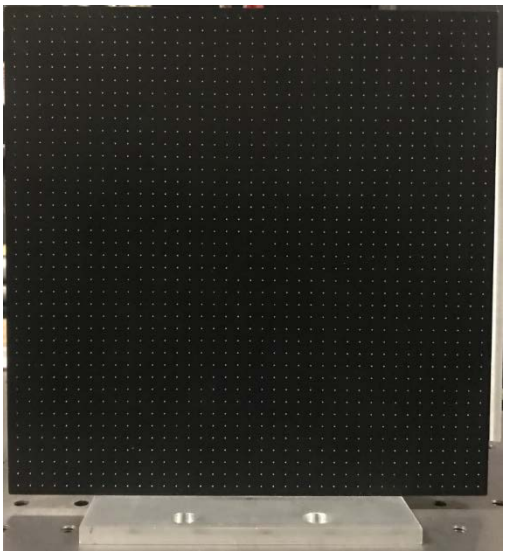

Figure 40: Calibration dot card to obtain image calibration factor for liftoff height measurements.

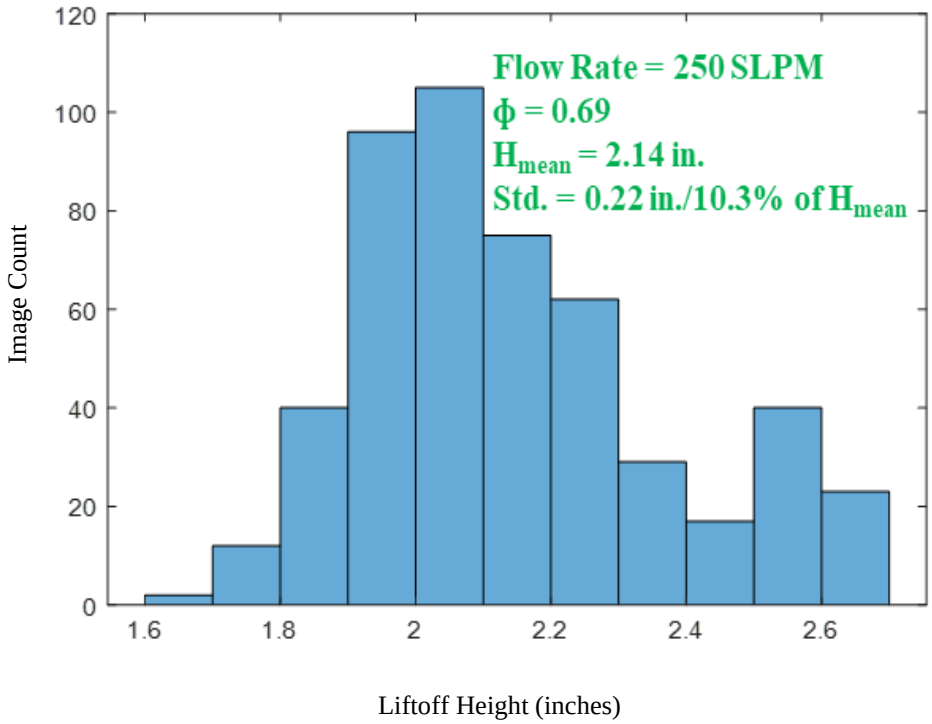

Figure 41: Liftoff height distribution for an air flowrate of 250 SLPM and an equivalence ratio of 0.69.

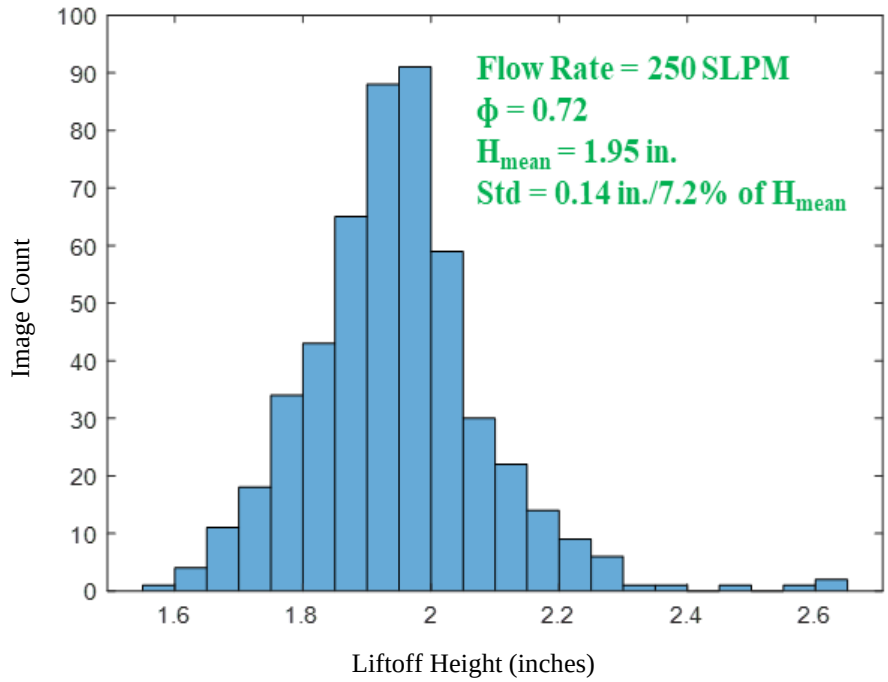

Figure 42: Liftoff height distribution for an air flowrate of 250 SLPM and an equivalence ratio of 0.72.

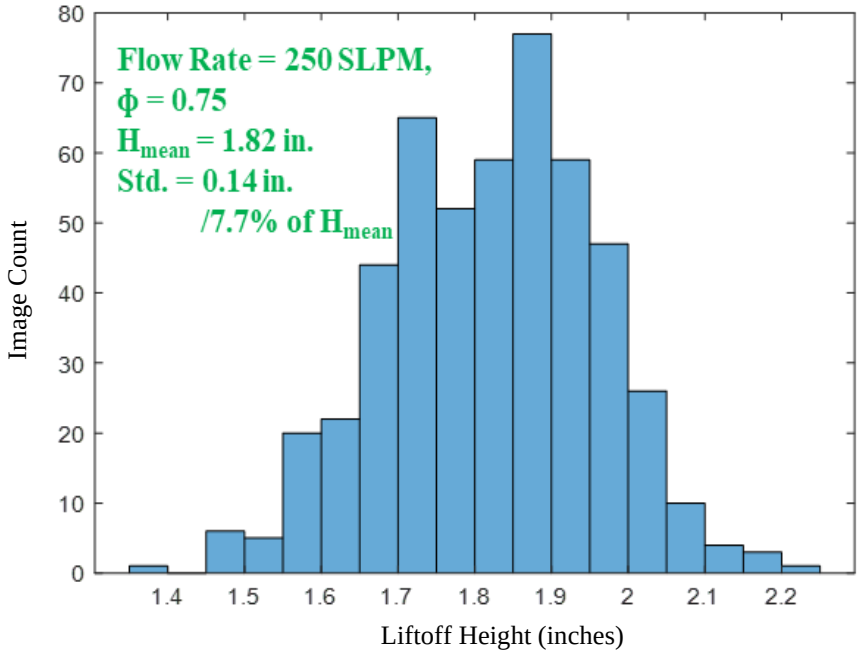

Figure 43: Liftoff height distribution for an air flowrate of 250 SLPM and an equivalence ratio of 0.75.

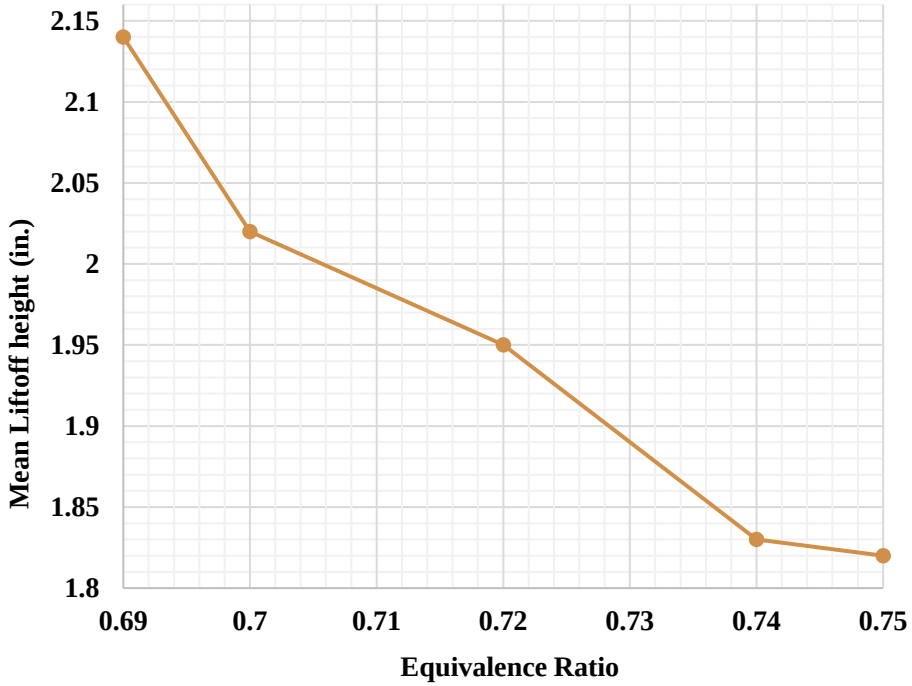

Figure 44: Mean liftoff height distribution for an increase in equivalence ratio.

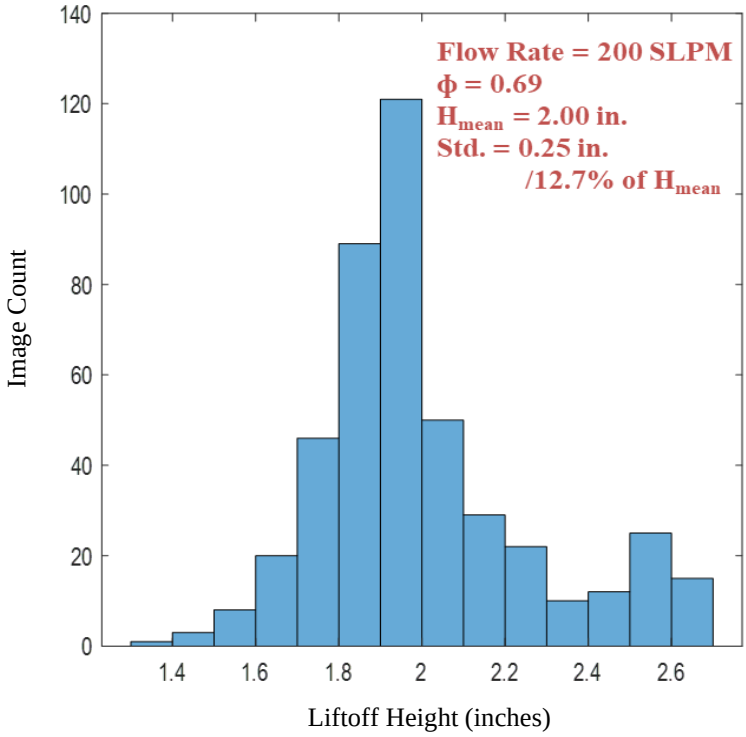

Figure 45: Liftoff height distribution for an air flowrate of 200 SLPM and an equivalence ratio of 0.69.

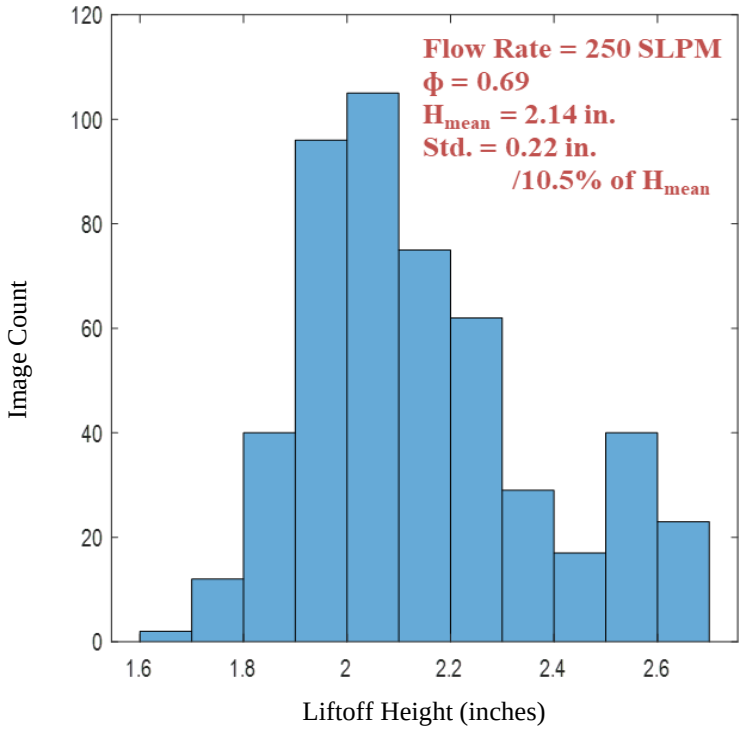

Figure 46: Liftoff height distribution for an air flowrate of 250 SLPM and an equivalence ratio of 0.69.

3.6 Plasma Generation: Effect of air flowrate

From previous work referenced in Section 2.1, two distinct plasma regimes were identified in quiescent air: diffuse and filamentary. Prior to coupling the plasma with the flame, the effect of the air flowrate on these distinct plasma regimes was investigated. The goal was to understand which plasma regimes were possible for the flow rates used on the burner. In this configuration, the inner electrode is placed approximately 1/4-inch below the burner exit plane. The plasma discharges were created with a fixed PRF of 50 kHz and a pulse width of 70 ns, as higher PRFs and pulses are required to break down the high resistance in the electrode gap. The electrical properties of last 10 pulses within the pulse train for a burst duration of 100 ms are presented. The last 10 pulses were captured by setting 99 ms delay on the delay generator which triggers the oscilloscope.

In the absence of flowing air, filamentary discharges like those shown in Section 2.1 were produced at the burner outlet and were confined to a small sector of the electrode plane. To obtain the energy deposited in the gap for one pulse, the voltage and current waveforms were multiped and then integrated in time over the pulse duration to yield energy deposited by the pulses. The average peak current and total energy deposited by the last 10 pulses in the electrode gap was 12 A and 18 mJ, respectively, as shown in Figure 48. The measured peak current from each of the last 10 pulses is comparable to the magnitude of the measured peak current from the last pulse in the diffuse plasma regime for the 100 ms case presented in Section 2.1. The distance between the tip of the inner electrode and the burner exit plane and in addition to the electrode gap further increased the resistance in the gap resulting in lower peak current.

For a constant air flow rate of 150 SLPM, the plasma regime changed from filamentary to a more diffuse streamer-like discharge, as shown in Figure 47. The high velocity of the incoming gas reduced the residence time of the concentration of the excited and ionized plasma species in the gap. The estimated residence time of an air particle in the gap can be obtained by diving the cathode length (length of ring electrode) by the bulk velocity after the swirler:

$$t_p = \frac{h}{v} \quad (7)$$

The number of pulses that the air particles are subjected to when traveling through the electrode gap can be obtained by multiplying the residence time by the PRF:

$$no.pulses = t_p \times PRF \quad (8)$$

In this condition, the residence time was 11.7 ms resulting in 588 pulses. For a PRF of 50 kHz, the calculated number of pulses is 5000; therefore, the air particles are exposed to less than 15% of the calculated number of pulses. The increased in voltage amplitude and total energy deposited mitigates this effect to increase the number of species in the gap to achieve breakdown. The average peak voltage, peak current and total energy deposited was 12 kV, 6 A, and 35 mJ, respectively, as shown in Figure 49.

As the air flowrate increased further to 300 SLPM, a similar trend was observed. The residence time is 5.77 ms corresponding to 289 pulses. The average peak voltage, peak current and total energy deposited for the last 10 pulses was 12 kV, 6 A, and 35 mJ, respectively as shown in Figure 50. The electrical properties remained the same, likely because 289 pulses were sufficient to break down the gap. This effect is also observed in a study by Heitz et al. [42] using a ring-pin electrode geometry with gap length of 7.7 mm at a PRF of 30 kHz. A summary of the electrical properties for the last 10 pulses is presented in Figure 51.

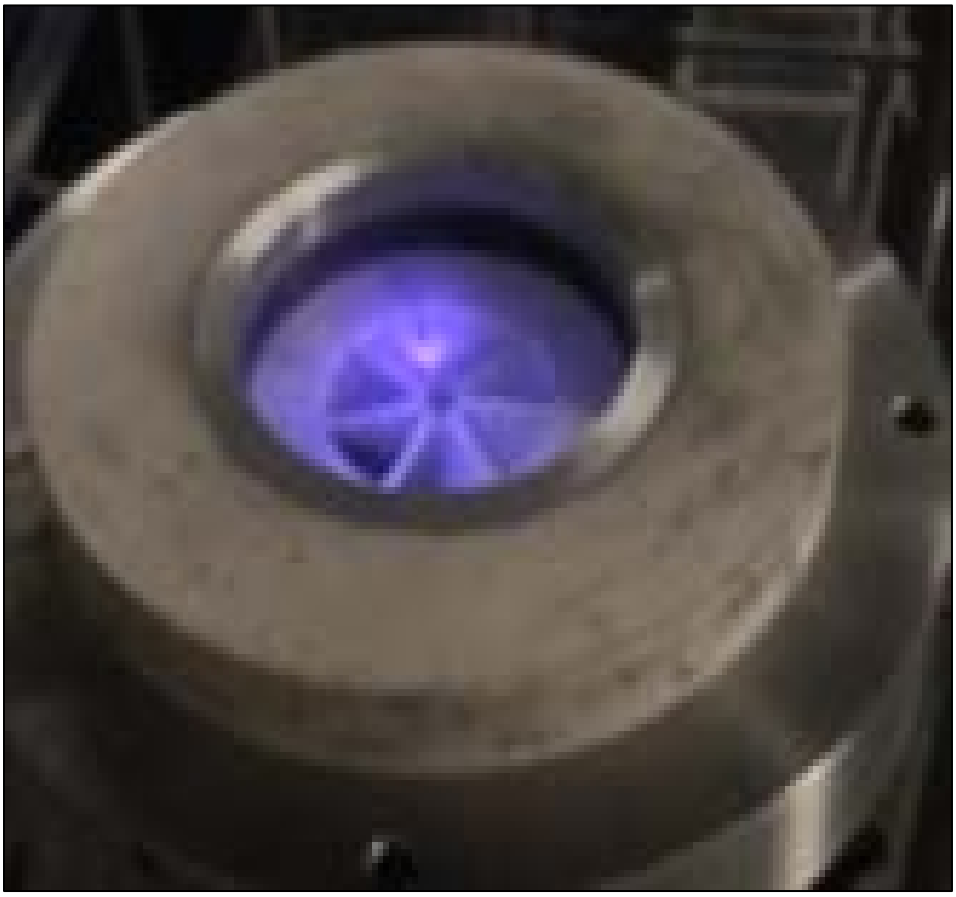

Figure 47: Diffuse plasma regime for an air flowrate of 300 SLPM.

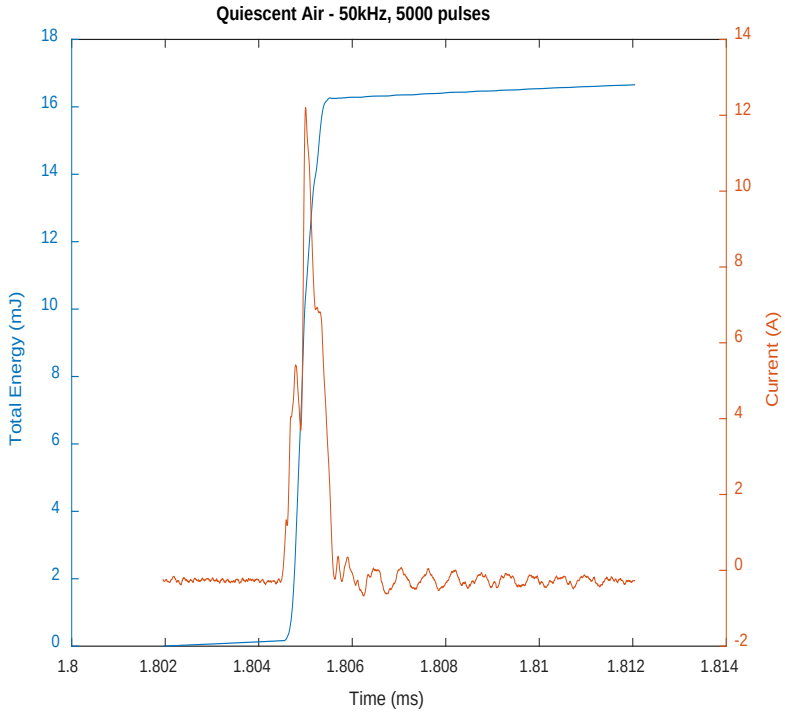

Figure 48: Total energy and peak current from the last 10 pulses for filamentary plasma regime in quiescent air.

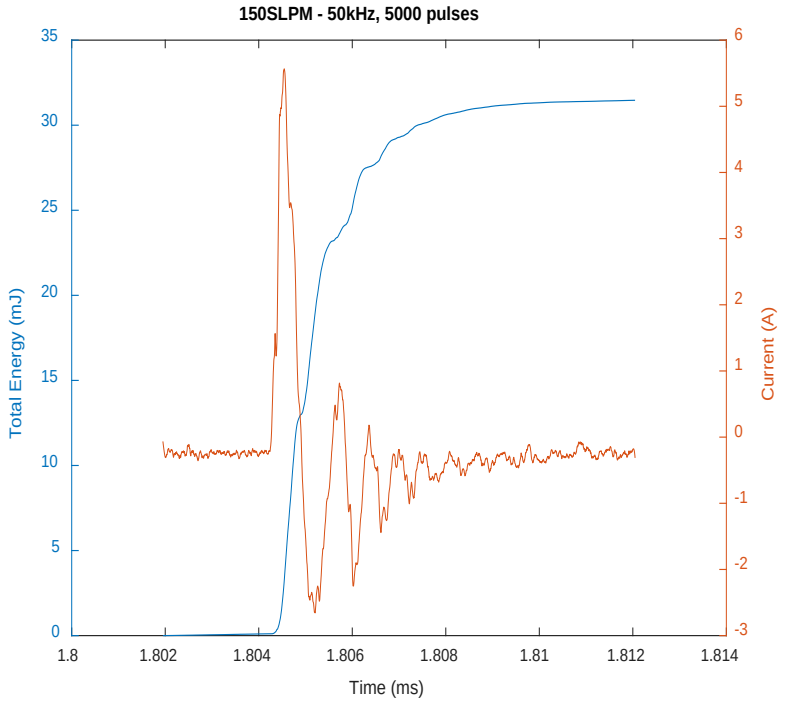

Figure 49: Total energy and peak current from the last 10 pulses for diffuse plasma regime with an air flowrate of 150 SLPM.

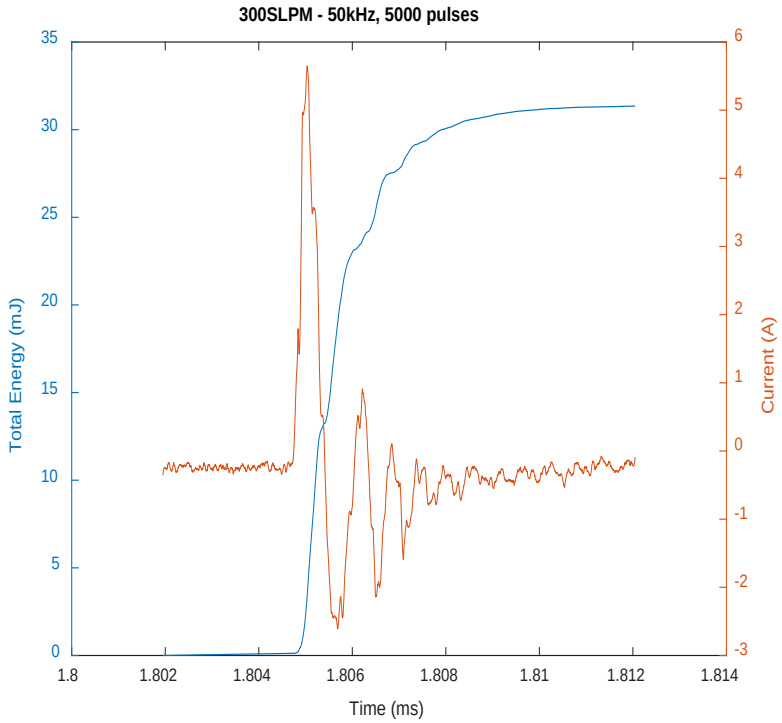

Figure 50: Total energy and peak current from the last 10 pulses for diffuse plasma regime with an air flowrate of 300 SLPM.

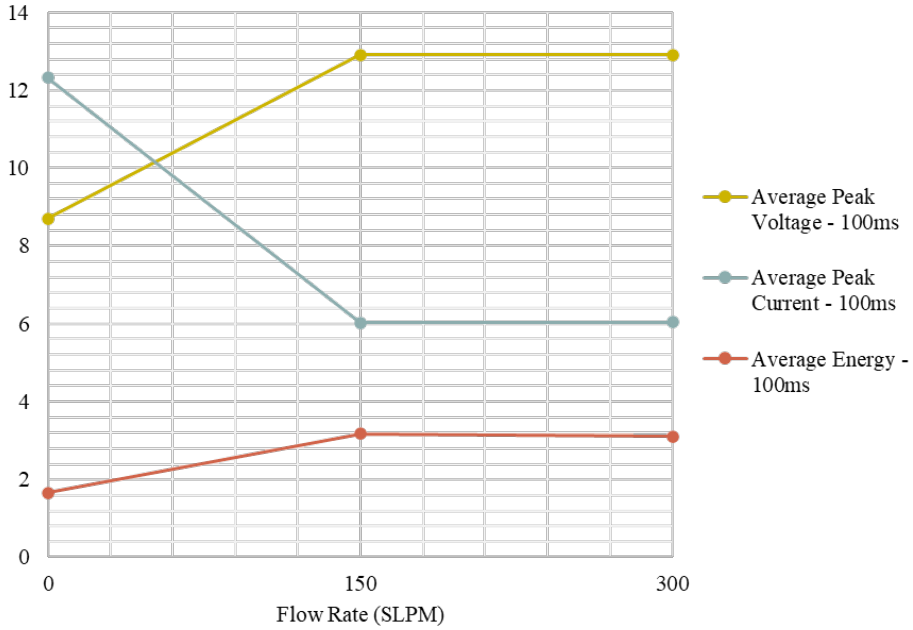

Figure 51: Average peak voltage, current, and energy distribution from the last 10 pulses as a function of air flow rate.

3.7 Direct Imaging of Plasma-Assisted Swirled Flames

The effect of the plasma discharge on flames was investigated using a cylindrical quartz tube with a confinement ratio of 2.56, as shown Figure 52. In this configuration, the effect of the corner recirculation zone is reduced, and the flame location is approximately 1-inch above the burner exit plane. For these series of tests, the swirlers were not coated with stainless-steel paint and we hypothesize that the smaller confinement ratio and circular cross section effectively reduced the effect of the corner recirculation zone. The flow velocity remains relatively high as it exits the burner and has insufficient time to create a low velocity region where significant heat could be transferred to the swirler. In the cuboid configuration, the large expansion (confinement) and geometry allowed for heat to be concentrated near the exit plane forming a strong corner recirculation zone. The concentrated heat was not conducted away and significant heat was transferred to the swirlers. The cylindrical confinement is 2.0 inches taller than the cuboid and the flame was observed to stretch significantly leading to some heat loss from the flame to the glass. The operating envelope for this configuration is presented in Table 6. The experiment schematic for these measurements is the same as the schematic shown in Figure 16.

We began with the investigation of the plasma discharge on lifted flames. In this case, the flame was ignited using a propane torch, and upon stabilization, the plasma discharge was applied. Qualitative direct imaging was performed to visualize on the effect of the plasma discharge on the flame. The images were obtained at 8000 fps with a 63% intensifier gain. A bit shift of 2 was applied to the flame images, taken before the plasma discharge was applied, to increase the signal in image processing. The camera was set on center mode to record images before and after the plasma discharge was applied. A summary of the plasma pulse parameters is presented in Table **7**.

From the quiescent measurements, it was observed that a minimum of 500 pulses at 10 kHz was needed to produce a plasma discharge in the large electrode gap. For the plasma-flame measurements, a minimum of 100 pulses at 50 kHz generated bright, filamentary plasma discharges in the electrode gap. The significant heat transfer from the flame to the incoming gas effectively reduced the resistance in the gap, accelerating the electron-impact ionization process and allowing breakdown to occur with very low number of pulses. Figure 53 and Figure 56 show the effect of the plasma discharges on a swirl stabilized lifted flame.

Table 6: Burner operating envelope with cylindrical confinement.

Air Flow Rate (SLPM)	Thermal Power (kW)	Bulk Re
300	10.3	11787
275	9.3	10794
250	8.4	9813
200	6.6	7842

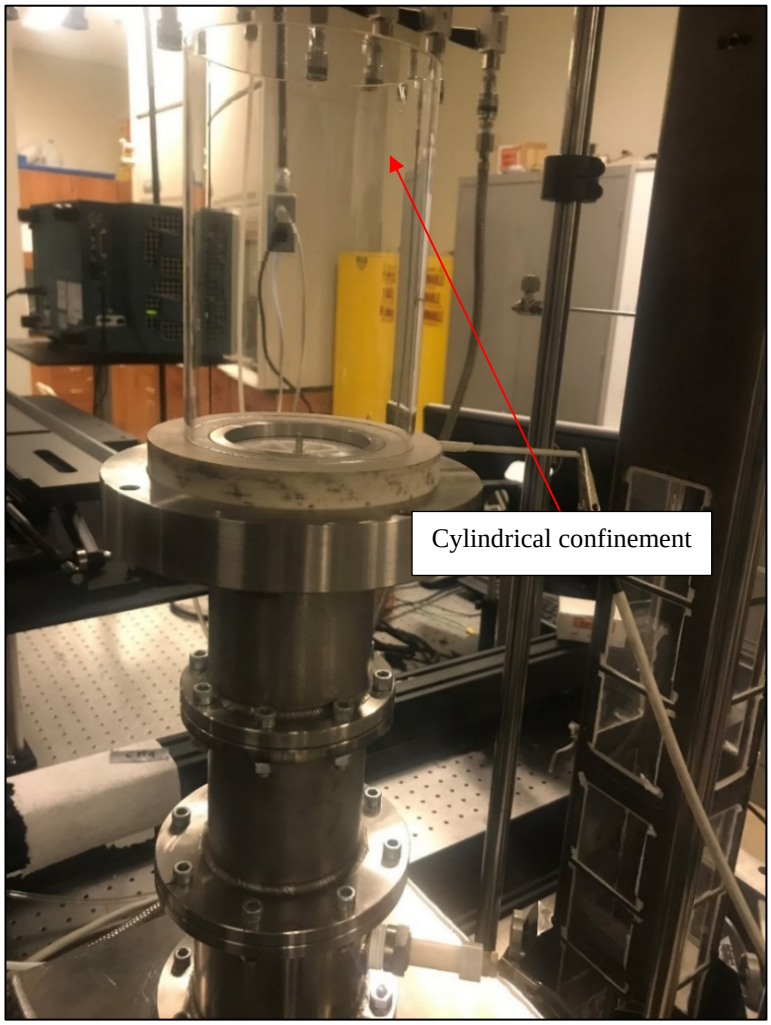

Figure 52: Burner geometry for plasma assisted flames and ignition measurements.

Table 7: Electrical pulse parameters used for direct imaging of plasma-assisted swirled flames.

Plasma Flame Imaging		
Pulses	**Frequency (kHz)**	**Burst Duration (ms)**
100	50	2.00
500	50	10.00
Plasma Ignition Imaging		
6000	50	120.00

Figure 53 shows a sequence of images a lean (ϕ = 0.58, 200 SLPM) methane-air flame. The thermal power and bulk Reynold's number for this condition is 6.6 kW and 7840, respectively. The images were not chosen consecutively but show the evolution of the plasma-assisted flame at several time steps. In Figure 53 #a, a weakly luminous lifted flame is observed, stable at approximately 1 inch above the burner exit plane. A secondary flame from the plasma is developed and a bright ignition kernel is observed in Figure 53 #d. We hypothesized the induced flow field by the discharge is weak and Figure 53 #f shows the presence of both the original flame and the plasma-assisted flame at 5.7 ms. The newly ignited, bright plasma-flame travels downstream of the burner to merge with the original flame where it stabilized. The final flame is visually more luminous as compared to the flame from the torch igniter in Figure 53 #a. Although the discharge was visually observed to be in the filamentary regime, the effect of the plasma in this condition is presumed to be more in the altering of the chemical kinetic pathways, producing a much brighter flame with a high number of radicals in the flame region. No additional visual effects from direct imaging were observed in this condition besides the bright, secondary plasma-assisted flame. the liftoff height remained at approximately 1 inch above the burner exit demonstrating the ineffectiveness of the plasma discharge by this condition similar to the observations of Laio et al. [41].

The current and voltage waveforms were measured to obtain the energy deposited in the flame. We added a 1 ms delay to the delay generator and collected the middle 14 pulses in the pulse train, as shown in Figure 54 and Figure 55. In Figure 54, we captured the initiation of the breakdown process with strong variation in both current and energy measurements for the 14 pulses measured. The highest peak current recorded is 2 A higher than the peak current (~ 6.5A) recorded in the non-reacting flow measurements and the highest energy deposited by a single pulse is twice as much (3.5 mJ vs. 1.7 mJ). The addition of methane molecules in the gap likely increased the energy demand needed to initiate the formation of the plasma channel to generate the filamentary discharge for this case. The average peak voltage, current, and total energy from this case is shown in Table 8. The total energy deposited by the 14 pulses is approximately 32 mJ for a plasma power of 107 W for 0.3 ms. The plasma power is approximately 1.6% of the total flame power.

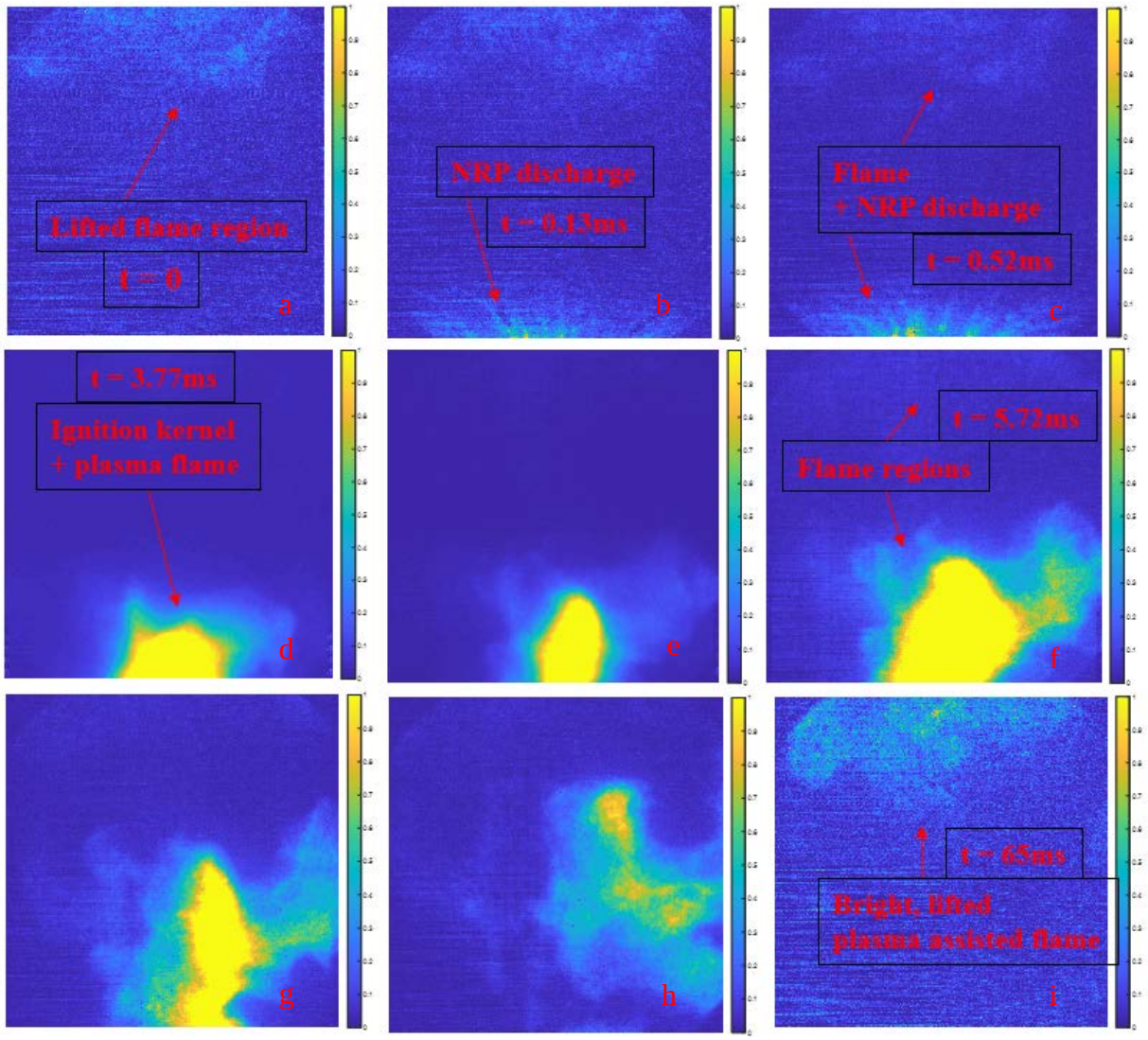

Figure 53: Images of a lean (ϕ = 0.58, 200 SLPM air) methane/air plasma-assisted flame obtained using a Photron SAZ high speed camera at 8000 fps with 100 pulses applied at 50 kHz for a burst duration of 2.0 ms.

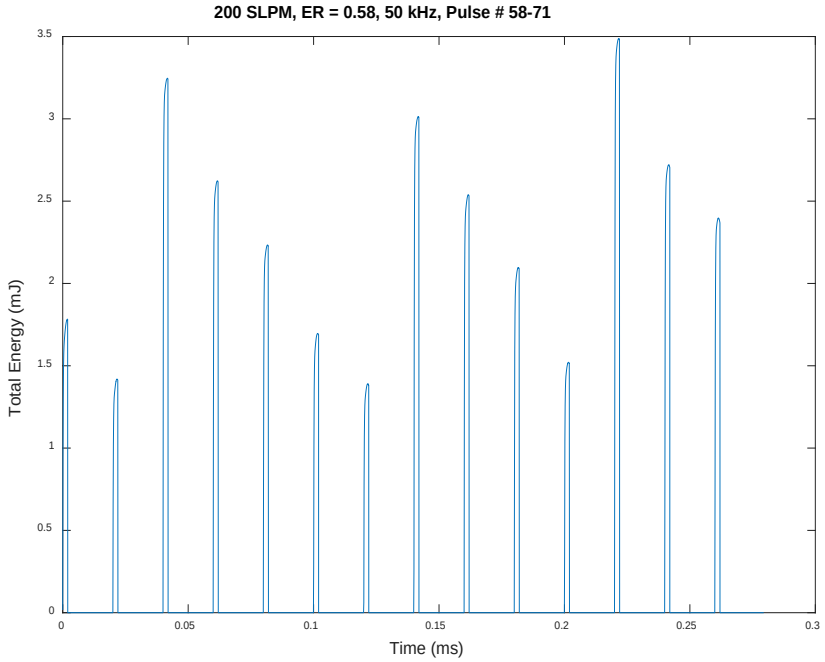

Figure 54: Total energy deposited (14 pulses) for plasma discharge generated in a lean (ϕ = 0.58, 200 SLPM air) methane/air flame at 50 kHz with a 1 ms delay.

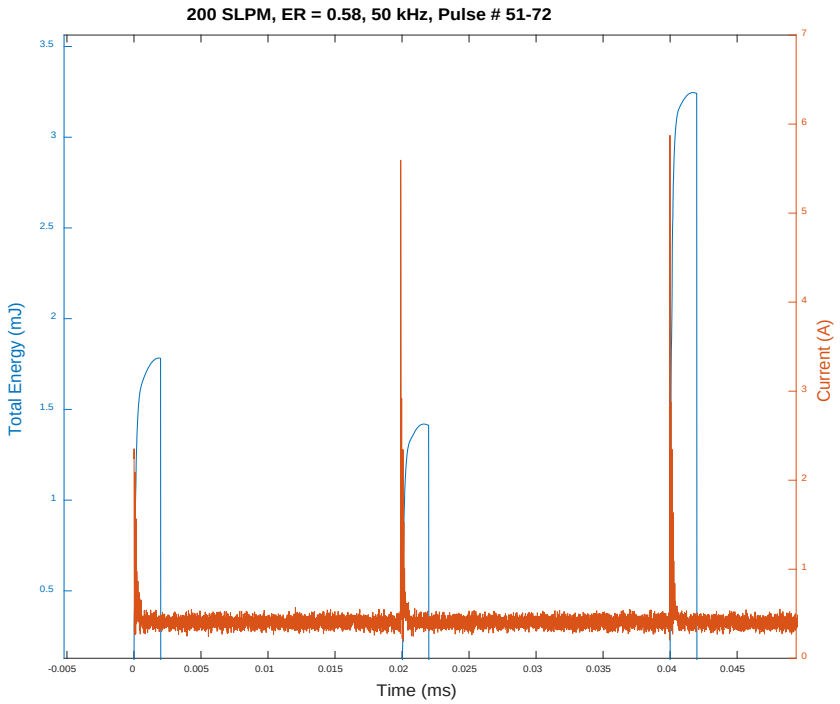

Figure 55: Current and total energy deposited (first 3 pulses) for plasma discharge generated in a lean (ϕ = 0.58, 200 SLPM air) methane/air flame at 50 kHz with a 1 ms delay.

Table 8: Average peak voltage, current, and total energy from the middle 14 pulses for plasma discharge generated in a lean (ϕ = 0.58, 200 SLPM air) methane/air flame at 50 kHz with a 1 ms delay.

Average Total Energy	Average Peak Voltage	Average Peak Current
2.29 mJ	24.08 kV	6.97A

Figure 56 shows a sequence of images a lean methane-air flame for the same condition as Figure 53. The images were not chosen consecutively but show the evolution of the plasma-assisted flame at several time steps. The flame ignited by the torch is shown in Figure 56 #a and the presence of both NRP discharge and the original flame is shown in Figure 56 #b-c. The plasma discharge was also in the filamentary regime but with visually higher intensity plasma channels similar to the discharges observed in Figure 23 #E in Section 2.1. A bright ignition kernel and plasma-assisted flame was observed upon ignition and the primary flame appeared to have extinguished. The result was a highly luminous, swirl-stabilized, plasma-assisted flame shown in Figure 56 #i. the plasma-assisted flame is stabilized at approximately 1 inch above the burner exit plane. We hypothesized that the effect of the plasma in this case is primarily the thermal mechanism with significant local induced flow and heating.

Current and voltage measurements were obtained to yield the energy deposited in the flame. A delay of 6 ms was applied to the pulse generator to trigger the oscilloscope to record the waveforms and the results for 14 pulses within a pulse train of 500 pulses are presented in Figure 57 – 57. The current and energy deposited for the 14 pulses are relatively constant compared to the 100 pulses case. We can conclude that breakdown has been achieved. The energy deposited by each pulse is consistently around 2.8 mJ which is a difference of 1 mJ compared to the non-reacting measurements in Section 3.6. The average peak current is approximately 9.2 A and is a difference of 3 A also compared to the non-reacting measurements in Section 3.6. The presence of the methane molecules likely requires more energy to be deposited in the gap to achieve breakdown. Table 9 details the average peak current, voltage, and total energy. More current is recorded compared to the 100 pulses case due to the higher number of pulses having reduced the resistance in the gap. The total energy deposited by the 14 pulses is approximately 31 mJ for a plasma power of 105 W for 0.3 ms. The plasma power is approximately 1.6% of the total flame power.

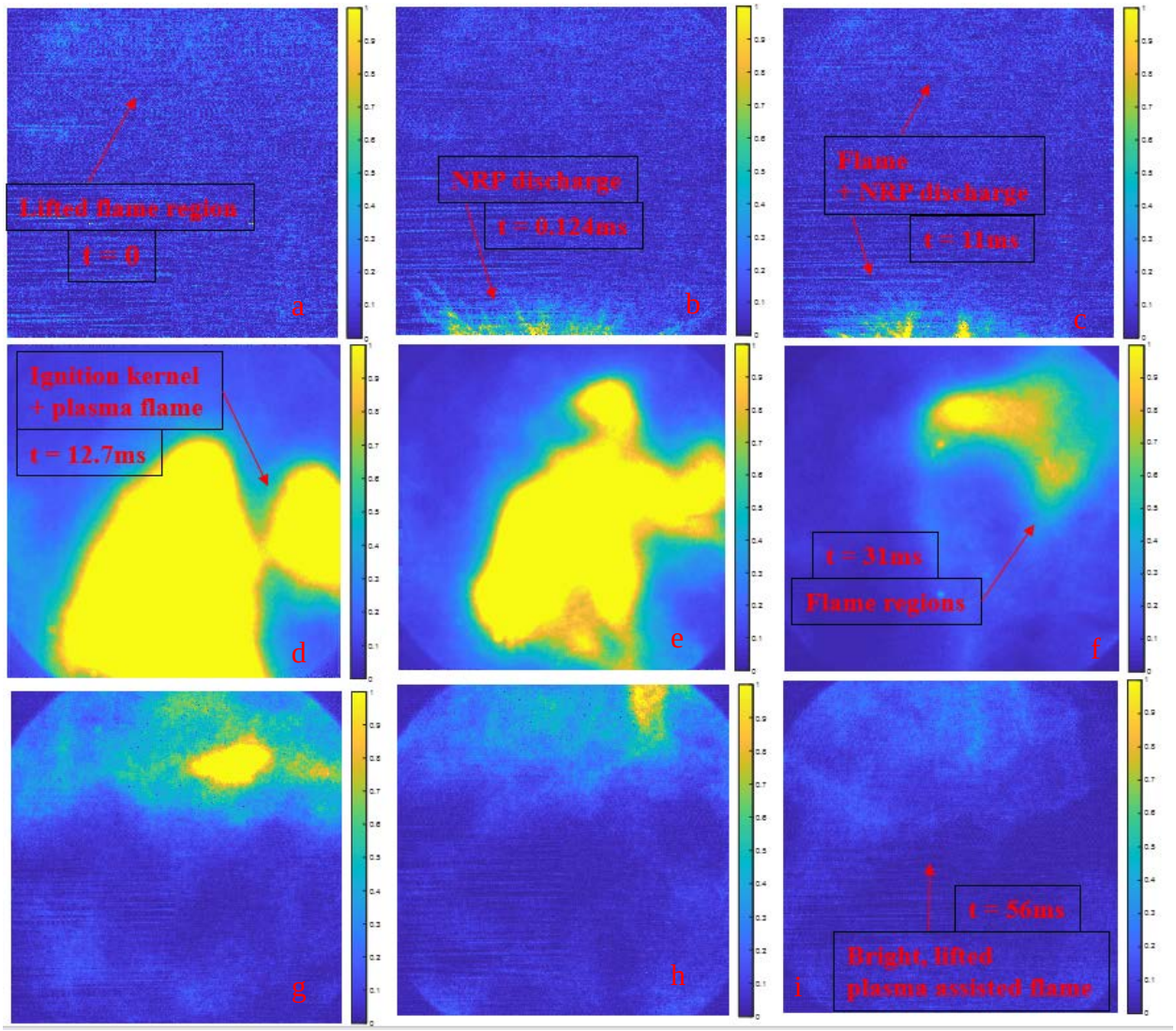

Figure 56: Images of a lean (ϕ = 0.58, 200 SLPM air) methane/air plasma-assisted flame obtained using a Photron SAZ high speed camera at 8000 fps with 500 pulses applied at 50 kHz for a burst duration of 10.0 ms.

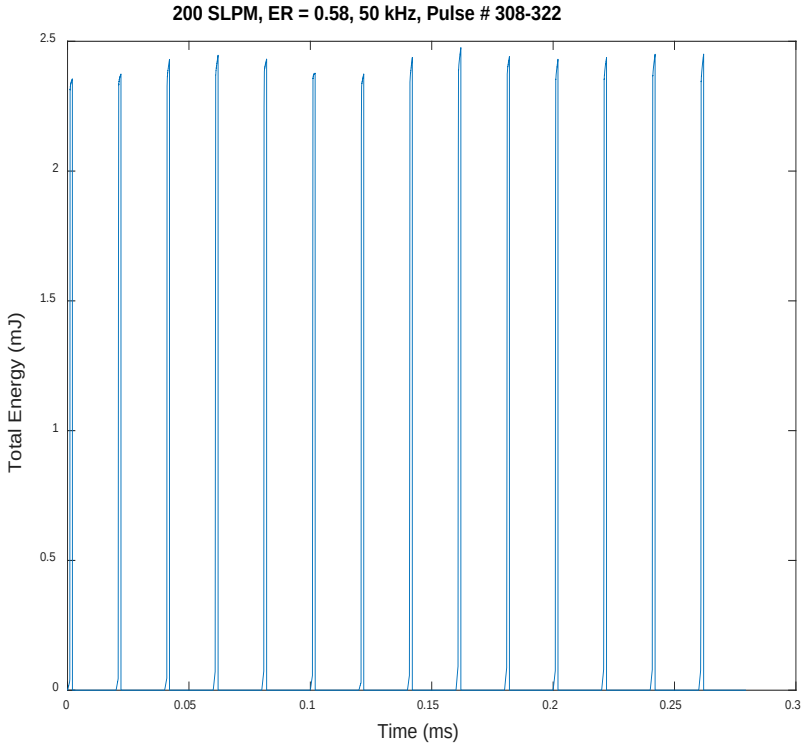

Figure 57: Total energy deposited (14pulses) for plasma discharge generated in a lean (ϕ = 0.58, 200 SLPM air) methane/air flame at 50 kHz with a 6 ms delay.

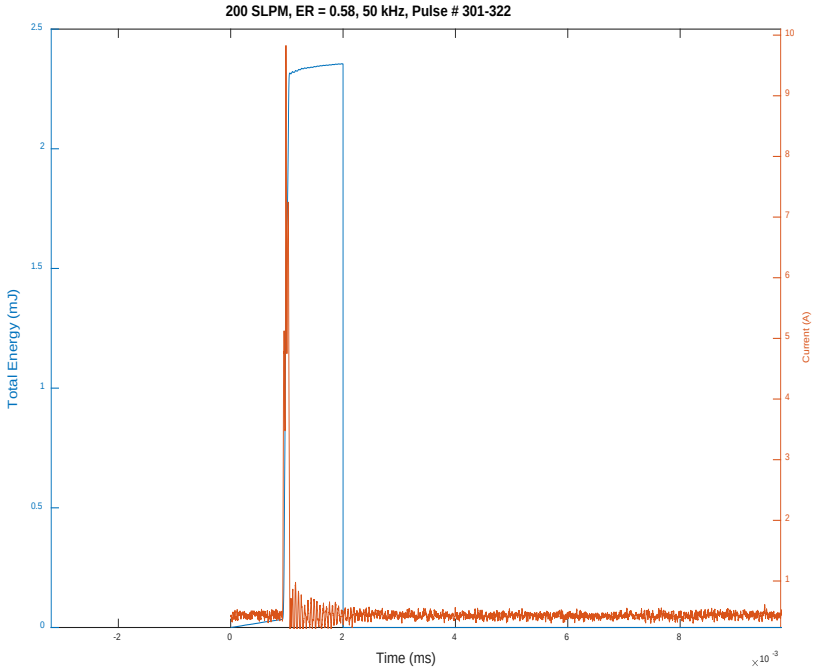

Figure 58: Total energy deposited and current (1st pulses) for plasma discharge generated in a lean (ϕ = 0.58, 200 SLPM air) methane/air flame at 50 kHz with a 6 ms delay.

Table 9: Average peak voltage, current, and total energy from the middle 14 pulses for plasma discharge generated in a lean (ϕ = 0.58, 200 SLPM air) methane/air flame at 50 kHz with a 6 ms delay.

Average Total Energy	Average Peak Voltage	Average Peak Current
2.41 mJ	20.7 kV	9.16 A

3.8 Direct Imaging of Plasma-Ignition of Swirled Flames

Figure 59 shows a sequence of images capturing the ignition of a lean methane-air flame (ϕ = 0.60, 200 SLPM air). The thermal power and bulk Reynold's number for this condition is 6.89 kW and 7860, respectively. The images were not chosen consecutively but show the evolution of the plasma-assisted flame at several time steps. A bright ignition kernel is formed with an accompanied plasma-flame in Figure 59 #b-h. The flame is stabilized and is anchored at approximately 1 inch above the exit plane in Figure 59 #i. As the equivalence ratio increased to 0.62 (6.67 kW, 7840, Figure 62), a plasma-assisted attached flame was obtained. This condition is near the attachment limit for the 200 SLPM case and we hypothesized that the plasma further increased the flame speed resulting in a thermally stable flame at the burner exit.

Current and voltage measurements were obtained to yield the energy deposited in the flame. A delay of 60 ms was applied to the pulse generator to trigger the oscilloscope to record the waveforms and the results for 14 pulses within a pulse train of 6000 pulses are presented in Figure 60 – 62. The current and energy deposited are relatively constant similar to the condition in Figure 54, an indication that breakdown has been achieved. The energy deposited by each pulse is consistently around 3.8 mJ which is a difference of 1 mJ compared to the plasma-flame measurements in Section 3.7. The total energy deposited by the 14 pulses is approximately 54 mJ for a plasma power of 180 W for 0.3 ms for the plasma-flame presented in Figure 59. The plasma power is approximately 2.6% of the total flame power. This result demonstrates that only a fraction of the flame power is needed from the plasma discharge to obtain a flame from plasma-ingiton. The average peak current is approximately 5.5 A. A summary is presented in Table 10. As the equivalence ratio increases, the methane flow rate increases as well, and the plasma discharge further increases the flame speed thereby producing attached flames at the burner exit.

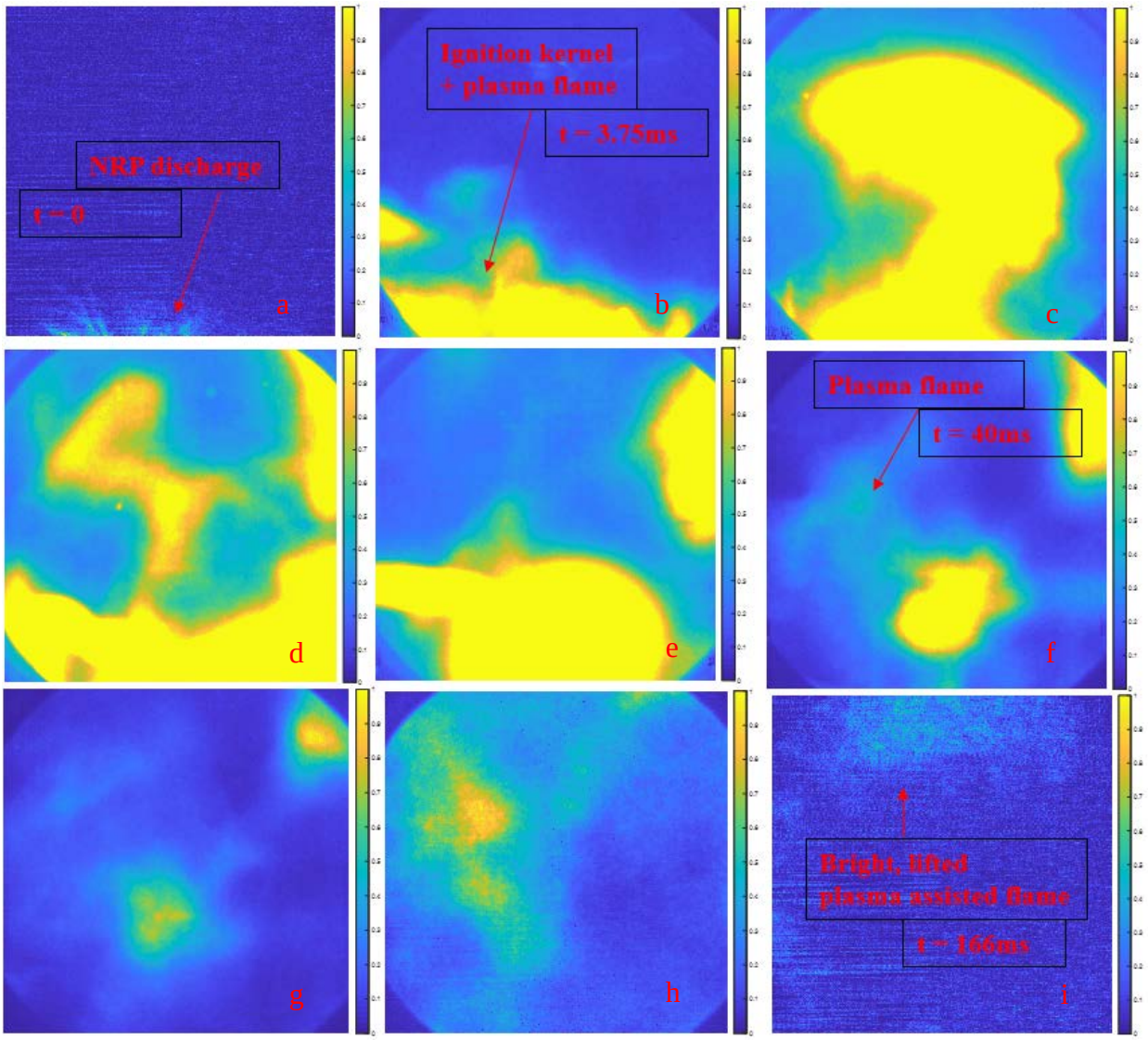

Figure 59: Images of a lean (ϕ = 0.60, 200 SLPM air) methane/air plasma ignition flame obtained using a Photron SAZ high speed camera at 8000 fps with 6000 pulses applied at 50 kHz for a burst duration of 120 ms.

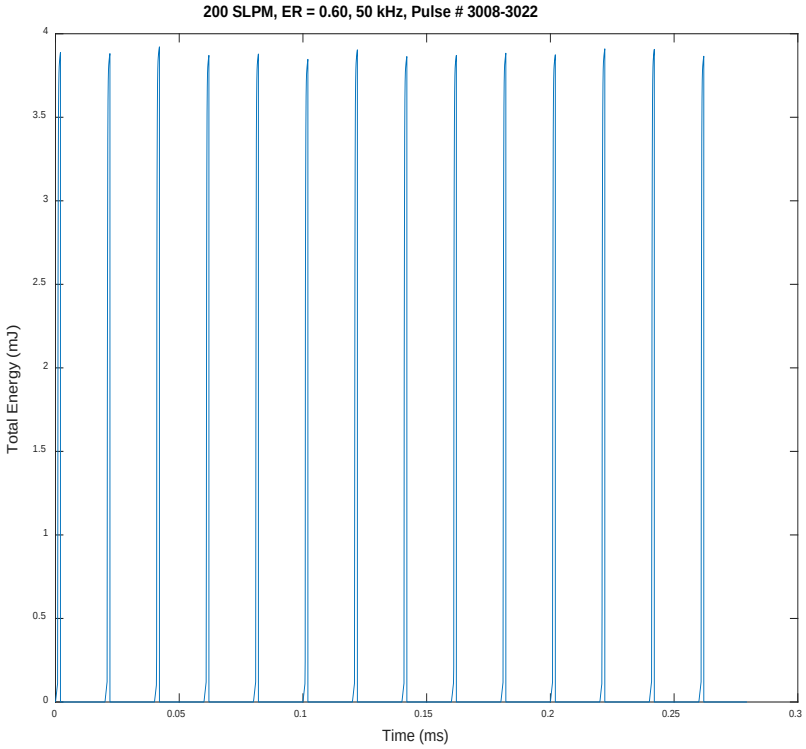

Figure 60: Total energy deposited (14 pulses) for plasma discharge generated in a lean (ϕ = 0.60, 200 SLPM air) methane/air flame at 50 kHz with a 60 ms delay.

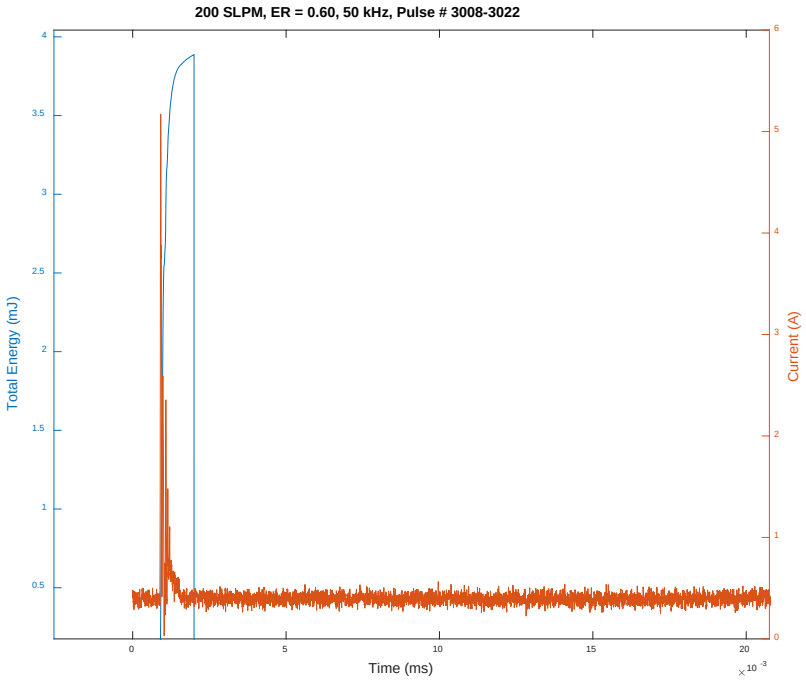

Figure 61: Total energy deposited (first pulse) and current a for plasma discharge generated in a lean (ϕ = 0.60, 200 SLPM air) methane/air flame at 50 kHz with a 60 ms delay.

Table 10: Average peak voltage, current, and total energy from the middle 14 pulses for plasma discharge generated in a lean (ϕ = 0.60, 200 SLPM air) methane/air flame at 50 kHz with a 60 ms delay.

Average Total Energy	Average Peak Voltage	Average Peak Current
3.88 mJ	24.78 kV	5.29 A

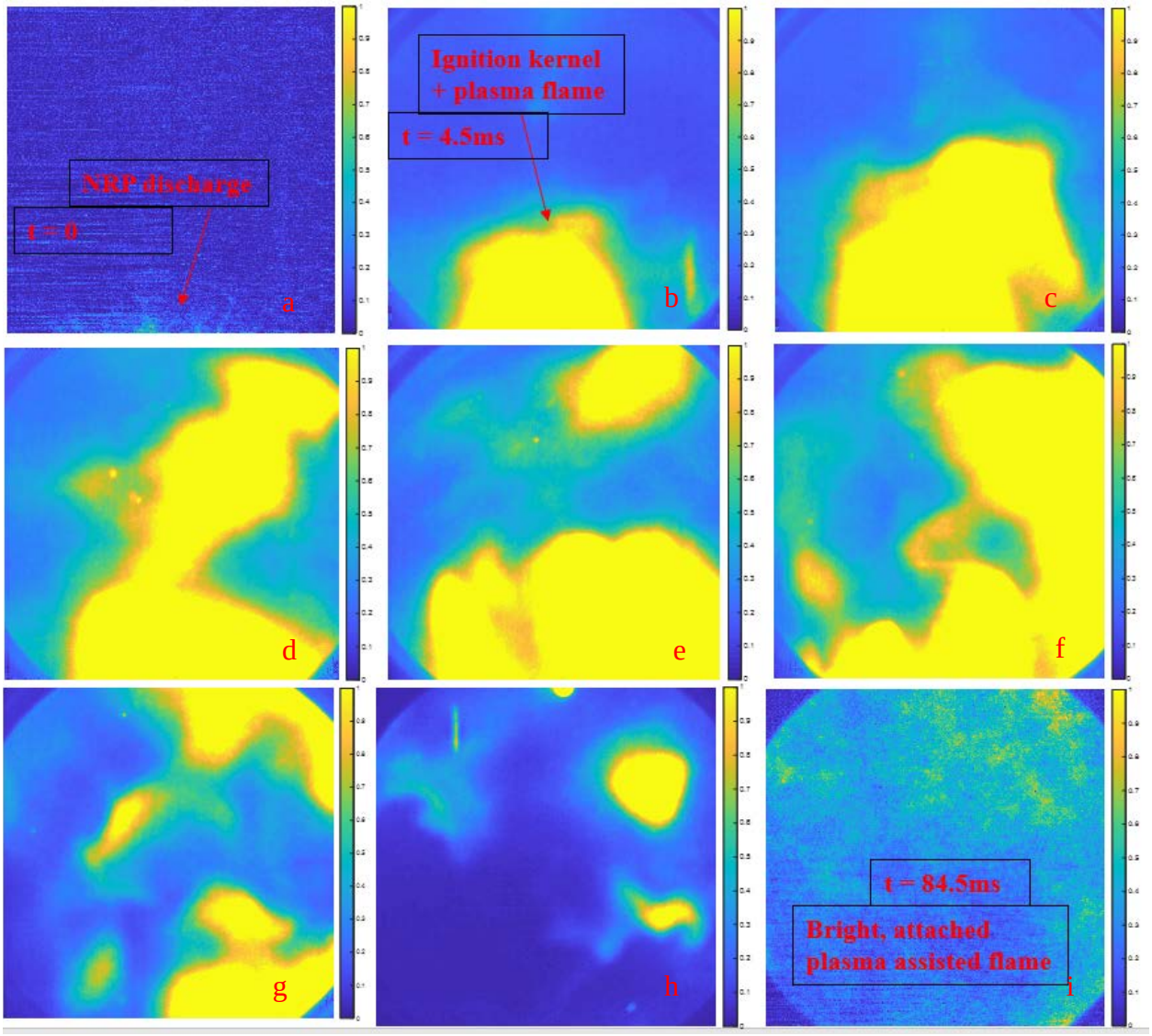

Figure 62: Images of a lean (ϕ = 0.62, 200 SLPM air) methane/air plasma ignition flame obtained using a Photron SAZ high speed camera at 8000 fps with 6000 pulses applied at 50 kHz for a burst duration of 120 ms.

3.9 Preliminary Investigation of Thermoacoustic Instability

To achieve thermoacoustic instability in the burner, a 4 inch square cross-section confinement tube was installed on top of the burner as shown in Figure 63. A confinement ratio (defined as the ratio of exit area of the burner to confinement area) of 9 was used to minimize interaction between the confinement tube walls and the swirl-stabilized flame. The L/D ratio of the confinement tube is 11. The tube has windows at the bottom to permit visual observation and optical measurements of the flame. Further, to study the effect of changing the L/D ratio on promotion of self-sustaining instability, a new flange system will be designed to facilitate a range of tube dimensions.

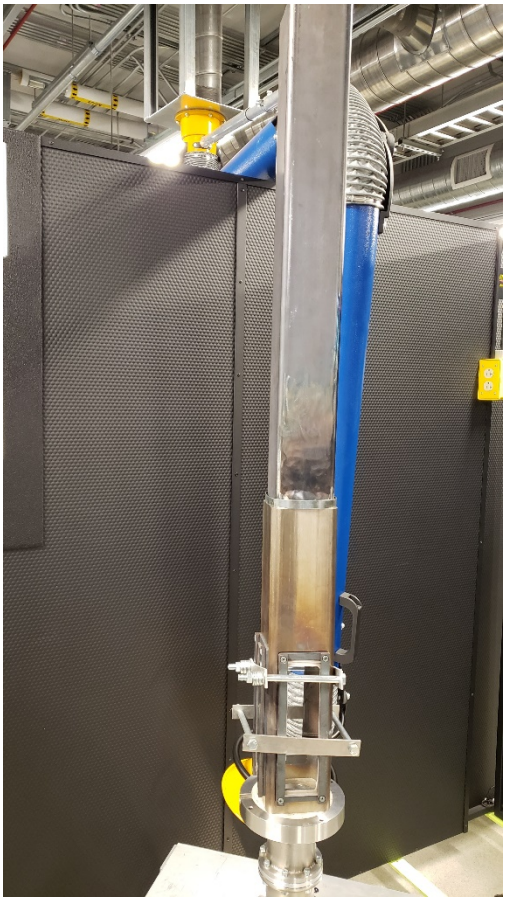

Figure 63: Burner with confinement tube installed to promote thermoacoustic instability.

To determine the burner operating range and investigate the presence of thermoacoustic instability, the swirl-stabilized burner with confinement tube was operated without plasma using air flow rates ranging from 150 SLPM to 350 SLPM. The focus of this preliminary study was to determine the detached and attached flame regimes at fuel-lean operating conditions and to detect the presence of any pressure oscillations corresponding to an instability. The burner blow-off equivalence ratio was used as the starting point, and further increasing the equivalence ratio moved

the detached flame closer to the burner exit until an attached flame was observed. The burner operating regime is shown in Figure 64. An image of the burner operating in the detached flame regime is shown in Figure 65. The equivalence ratios ϕ where significant visual flame oscillations were observed near the blow-off limit were noted. However, we did not observe self-excited thermo-acoustic instabilities in this configuration. The effect of NRP discharges on extending the flame blow-off limit will be studied in ongoing work.

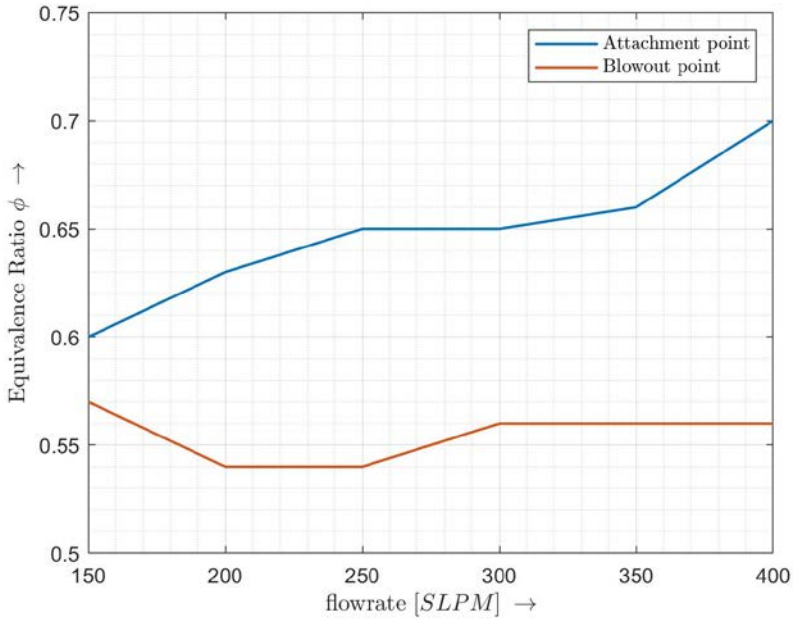

Figure 64: Burner operation regime between blow-out and attached flame.

To effectively promote thermoacoustic instabilities, the flow rate range was increased to 350 to 450 SLPM and the attached flame regime in the equivalence ratio range $\phi = 0.70$-0.90 was considered. Figure 66 shows images of a stable flame (left, $\phi = 0.70$, 400 SLPM) and an unstable flame (right, $\phi = 0.85$, 400 SLPM) with a background subtraction of the mean of the images taken for a period of 3 seconds (a total of 1500 images), the unstable flame has a lot of white spots in the flame region which shows it is oscillating more compared to the stable flame with a more defined outer recirculation zone. A distinct audible sound amplitude increase was observed when the flame was unstable. The conditions for achieving thermoacoustic instability will be further explored by moving the swirler position approximately 3 inches upstream. The effect of the distance between the swirler and the plasma generation (both near the burner exit vs. separated by 3 inches) will also be investigated.

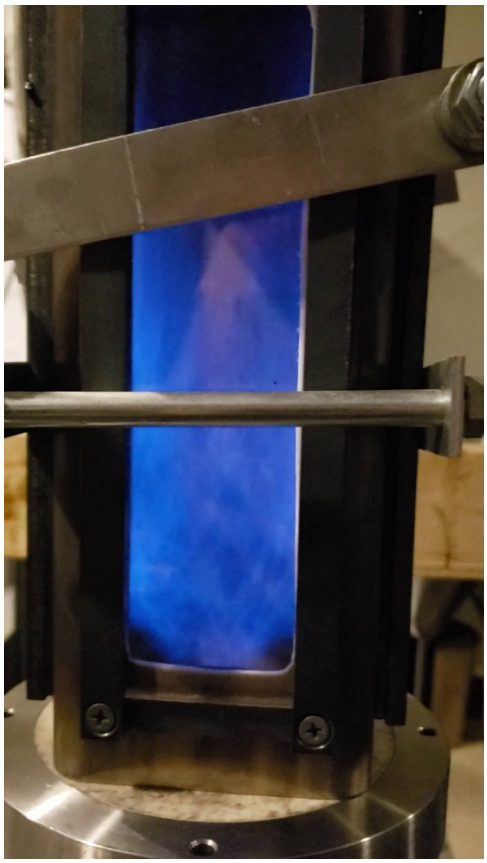

Figure 65: Swirl-stabilized detached flame (no plasma, $\phi = 0.6$, air flow rate = 200 SLPM).

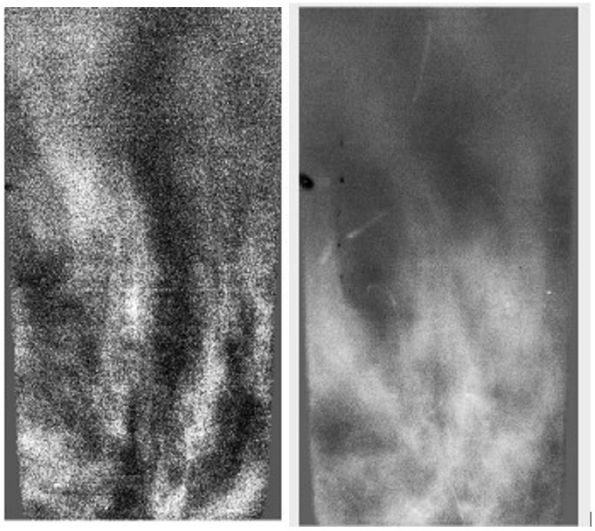

Figure 66: (Left) Stable swirled flame structure with recirculation zone at $\phi = 0.70$ and air flow rate of 400 LPM. (Right) Unstable flame at $\phi = 0.85$ and air flow rate of 400 LPM.

A condenser-type prepolarized microphone (PCB Electronics 378B02) was mounted near the confinement tube walls to measure the the frequency and amplitude of pressure fluctuations. The burner operating conditions was varied until high-amplitude pressure oscillations are observed, such as in the case shown in Figure 66 and the frequency detected by the microphone was recorded as shown in Figure 67. The high amplitude pressure signal (blue) corresponds to the right side image of the flame in Figure 66 and the low amplitude pressure signal (orange) corresponds to the left image with a stable flame.

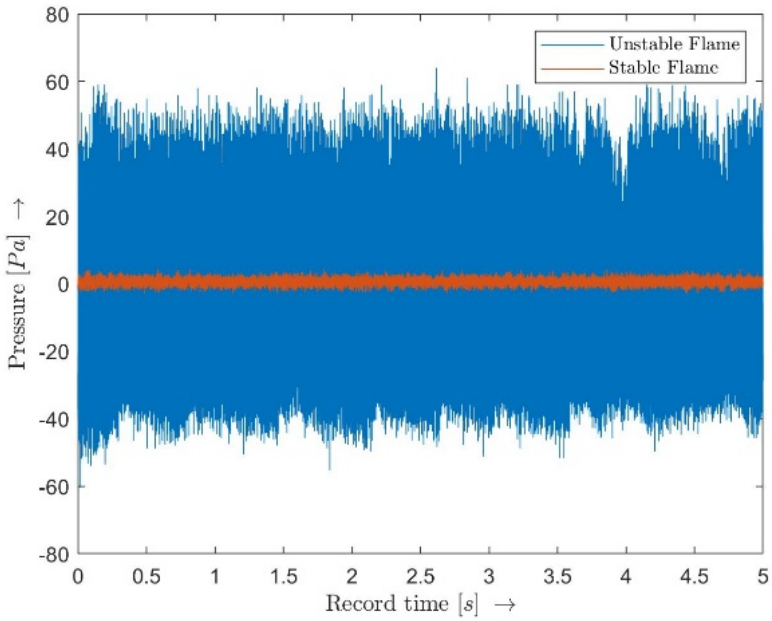

Figure 67: Pressure vs. time measured downstream of the flame.

4. SUMMARY & FUTURE WORK

The main goal of this project was to develop both atmospheric and high-pressure plasma-assisted burners to investigate the effect of nanosecond repetitively pulsed discharges on methane-air flames. To begin, a small plasma generation system was developed using a ring-pin electrode configuration with the goal of producing a plasma disk at the burner outlet. For all pulse parameters considered, two distinct plasma regimes were identified: diffuse and filamentary. Diffuse, homogenous plasmas are observed at low and intermediate PRF, while high PRF produced localized, high intensity sparks at random locations along the loop electrode.

We then moved to characterize the induced flow field by the plasma discharge. We employed high speed schlieren visualization which allows for the visualization of the density gradients in the flow. Supporting our hypothesis, the diffuse plasma discharges produced modest heating of the gas and weak shock waves due to the rapid heating. For the filamentary plasma discharges, the gas heating was significantly higher, resulting in stronger induced shock waves, and a higher degree of induced flow. High-speed (10kHz) particle image velocimetry (PIV) was used to quantify the flow velocity produced by the plasma discharges. The PIV images were recorded and processed using PRANA (PIV Research and ANAlysis) software. Preliminary results show significant induced flow near the location of the discharge, which coincides with the high-speed schlieren observations. The absolute velocity of the induced flow field is on the order of 15m/s which suggests the plasma-induced flow velocity may have a significant effect on the flame. Lastly, OES was used to investigate the magnitude of the gas temperature in the electrode gap. We found that both vibrational and rotational temperatures moderately at PRFs of 10 – 20 kHz but significantly at 50 kHz.

Finally, an atmospheric pressure plasma-assisted burner was designed and fabricated for investigating plasma-flame interaction. The burner can produce both Bunsen-type and swirl-stabilized flames with a modular design to allow for a removable block swirler component. A helical vane swirler with a swirl number of 0.62 was designed and 3D printed to produce swirl stabilized flames. For simple non-swirled flames, the design includes a straight honeycomb structure with 2.8 mm cell size which serves as a flow straightener to ensure swirl-free flows. A ring-pin electrode configuration is installed at the burner exit for generating the plasma. A plumbing system for supplying fuel and oxidizer to the burner at precisely controlled flow rates as well as an experiment control/data acquisition system have been designed and built. The burner along with the plumbing and control/DAQ systems are installed on a portable cart for transporting the burner to different labs for laser diagnostic measurements.

To characterize the burner, chemiluminescence and direct imaging was done to understand the burner's operating limits. The burner can operate 6 – 13 kW flames. Liftoff height measurements were done to approximate the flame anchor location. We found that the flame is stabilized at approximately 2 inches above the burner exit plane for all of the cases investigated. The effect of flow rate on the plasma regimes determined with the smaller electrode fixture was investigated. In quiescent air, the plasma discharge regimes were similar to that of the smaller plasma generation

system. In non-reacting flowing air, only filamentary discharges were produced. The short residence time of the plasma species reduced the effect of the accumulation of pulses that created a filamentary discharge in quiescent air.

Finally, the plasma discharge was applied on lifted, swirled flames and used for plasma-assisted ignition. For lifted swirled flames, we found that a minimum of 100 pulses is required to generate a filamentary discharge in the air stream. The heat transfer from the flame to the incoming gas reduced the resistance in the gap, allowing breakdown to occur at very low number of pulses. Diffused discharges did show any visual impact on lifted flames, but we hypothesize that their impact will have to be measured quantitatively for further investigation. For ignition, a minimum of 6000 pulses was used to obtain a filamentary discharge to ignite the burner under cold start conditions. The methane flow rate had a significant impact on the plasma regime obtained. Diffused discharges did not provide enough energy deposition in the gap for ignition. Filamentary discharges, with their high energy deposition, were more suited for ignition in cold flow conditions. Increasing the equivalence ratio with the addition the plasma discharge further increased the flame speed, allowing for the flame to thermally stabilize at the burner exit.

The findings for these preliminary sets of measurements on the atmospheric pressure plasma-assisted burner show that the plasma discharges have significant impact on combustion if applied under the proper conditions. For lifted flames, the plasma-flame coupling effected can be attributed to the chemical mechanism where the effect is more quantitative in the generation of chemical species and direct imaging showed more luminous flames once the plasma discharge had been applied. For plasma ignition, the plasma discharges were used to ignite very lean flames, extending the lean blowout limit which corroborates findings from published results. The plasma-flame measurements presented in this document were primarily qualitative; therefore, more quantitative measurements will further probe into the effect of plasma discharges on swirled flames.

The development of the plasma-assisted burner experiment in this work provides the necessary infrastructure for many ongoing and future studies. The current focus of ongoing work is exploring the effect of NRP plasmas on thermoacoustic instability by continuing the work presented in Section 3.9. This pressure data will be matched with the quarter wave resonating frequency of the confinement tube using Fast Fourier Transforms to classify it as thermoacoustic instability. NRP plasma discharges will then be generated at the burner exit using a range of PRFs, focusing first on plasma actuation at the same frequency of the pressure fluctuations but with different phase shifts. Any resulting changes to the instability frequency, amplitude, and phase will be measured using the microphone.

In addition, the effect of the plasma on the flame structure will be investigated using CH* chemiluminescence visualization. A LaVision lens coupled image intensifier mounted on a Photron SA-Z high-speed camera with appropriate filters for CH* will be used to obtain images at rates up to 10,000 frames per second. The effects of the plasma on the steady-state and dynamic flame structure and on the thermoacoustic instability will be investigated simultaneously. Based on the results, further testing conditions (flow rates, confinement tube sizes, etc.) will be proposed, and plans for implementing advanced diagnostics (e.g. absorption spectroscopy techniques for measuring gas temperature and radical species) will be outlined.

LIST OF REFERENCES

[1] F. Cebulski, T. R. Garcia and D. Strong, "Clean and Efiicient Combustion of 21st Century Transportation Fuels," Arlington, Va, 2006.

[2] A. Starikovskiy and N. Aleksandrov, "Plasma-Assisted Ignition and Combustion," *Progress in Energy and Combustion Science,* vol. 39, pp. 61-110, 2013.

[3] W. R. Lempert and I. V. Adamovih, "Challenges In Understanding and Predictive Model Development of Plasma-Assisted Combustion," *Plasma Physics and Controlled Fusion,* vol. 57, p. 014001, 2015.

[4] Y. Ju and W. Sun, "Plasma assisted combustion: Dynamics and Chemistry," *Progress in Energy and Combustion Science,* vol. 48, pp. 21-83, 2015.

[5] Y. P. Raizer, Gas Discharge Physics, Moscow: Springer-Verlag, 1987.

[6] A. Starikovskiy and N. Aleksandrov, "Plasma-Assisted Ignition and Combustion," *Progress in Energy and Combustion Science,* vol. 39, pp. 61-110, 2013.

[7] G. D. Stancu, F. Kaddouri, D. A. Lacoste and C. O. Laux, "Investigations of rapid plasma chemistry generated by nanosecond discharges in air at atmospheric pressure using advanced optical diagnostics," in *40th AIAA Plasmadynamics and Lasers Conference*, San Antonio, TX, 2009.

[8] S. Nagaraja, T. Li, J. A. Sutton, I. V. Adamovich and V. Yang, "Nanosecond plasma enhanced H2/O2/N2 premixed flat flames," *Proceedings of the Combustion Institute,* vol. 35, pp. 3471-3478, 2015.

[9] D. A. Xu, D. A. Lacoste and C. O. Laux, "Temporal and spatial evolution of OH concentration in a lean premixed propane-air flame assisted by nanosecond repetitively pulsed discharges," in *51st AIAA Aerospace Sciences Meeting*, Grapevine, TX, 2013.

[10] T. M. Vu, S. H. Won, T. Ombrello and M. S. Cha, "Stability enhancement of ozone-assisted laminar premixed Bunsen flames in nitrogen co-flow," *Combustion and Flame,* vol. 161, pp. 917-926, 2014.

[11] D. A. Lacoste, D. A. Xu, J. P. Moeck and C. O. Laux, "Dynamic Response of a Weakly Turbulent Lean-Premixed Flame to Nanosecond Repetitively Pulsed Discharges," *Proceedings of the Combustion Institute,* vol. 34, pp. 3259-3266, 2013.

[12] W. Kim, M. G. Mungal and M. A. Cappelli, "The role of in situ reforming in plasma enhanced ultra lean premixed methane/air flames," *Combustion and Flame,* vol. 157, pp. 374-383, 2010.

[13] W. Sun, M. Uddi, T. Ombrello, S. H. Won, C. Carter and Y. Ju, "Effects of non-equilibrium plasma discharge on counterflow diffusion flame extinction," *Proceedings of the Combustion Institute,* vol. 33, pp. 3211-3218, 2011.

[14] W. Sun, M. Uddi, S. H. Won, T. Ombrello, C. Carter and Y. Ju, "Kinetic effects of non-equilibrium plasma-assisted methane oxidation on diffusion flame extinction limits," *Combustion and Flame,* vol. 159, pp. 221-229, 2012.

[15] W. Sun, S. H. Won and Y. Ju, "In situ plasma activated low temperature chemistry and the S-curve transition in DME/oxygen/helium mixture," *Combustion and Flame,* vol. 161, pp. 2054-2063, 2014.

[16] D. A. Lacoste and C. O. Laux, "Effect of Plasma Discharges on Nitric Oxide Emissions in a Premixed Flame," *Journal of Propulsion and Power,* vol. 29, no. 3, pp. 748-751, 2013.

[17] G. D. Stancu, M. Simeni Simeni and C. O. Laux, "Study of nitric oxide and carbon monoxide production in plasma assisted combustion by Quantum Cascade Laser Absorption Spectroscopy," in *21st International Symposium on Plasma Chemistry,* Queensland, Austraila, 2013.

[18] G. Pilla, D. Galley, D. Lacoste, F. Lacas, D. Veynante and C. Laux, "Stabilization of a Turbulent Premixed Flame Using a Nanosecond Repetitively Pulsed Plasma," *IEEE Transactions on Plasma Science,* vol. 34, no. 6, pp. 2471-2477, 2006.

[19] G. L. Pilla, D. A. Lacoste, D. Veynante and C. O. Laux, "Stabilization of a Swirled Propane-Air Flame Using a Nanosecond Repetitively Pulsed Plasma," *IEEE Transactions on Plasma Science,* vol. 36, no. 4, pp. 940-941, 2008.

[20] Q. L. L. Pham, D. A. Lacoste and C. O. Laux, "Stabilization of a Premixed Methane-Air Flame Using Nanosecond Repetitively Pulsed Discharges," *IEEE Transactions on Plasma Science,* vol. 39, no. 11, pp. 2264-2265, 2011.

[21] D. A. Lacoste, J. P. Moeck, D. Durox, C. O. Laux and T. Schuller, "Effect of Nanosecond Repetiviely Pulsed Discharges on the Dynamics of a Swirl-Stabilized Lean Premixed Flame," *Journal of Engineering for Gas Turbines and Power,* vol. 135, p. 101501, 2013.

[22] J. P. Moeck, D. A. Lacoste, D. Durox, T. F. Guiberti, T. Schuller and C. O. Laux, "Stabilization of a Methane-Air Swirl Flame by Rotating Nanosecond Spark Discharges," *IEEE Transactions on Plasma Science,* vol. 42, no. 10, pp. 2412-2413, 2014.

[23] J. P. Moeck, D. A. Lacoste, C. O. Laux and C. O. Paschereit, "Control of Combustion Dynamics in a Swirl-Stabilized Combustor with Nanosecond Repetitively Pulsed Discharges," in *51st AIAA Aerospace Sciences Meeting,* Grapevine, TX, 2013.

[24] D. A. Lacoste and J. P. Moeck, "Effect of Nanosecond Glow Discharges on a Lean Premixed V-Flame," *IEEE Transactions on Plasma Science,* vol. 42, no. 12, pp. 4040-4041, 2014.

[25] D. A. Lacoste, B. J. Lee, A. Satija, S. Krishna, S. A. Steinmetz, I. Alkkhesho, O. Hazzaa, R. P. Lucht, M. S. Cha and W. L. Roberts, "Investigation of Gas Heating by Nanosecond Repetitively Pulses Glow Discharges Used for Actuation of a Laminar Methane-Air Flame," *Combustion Science and Technology,* vol. 11, no. 189, pp. 2012-2022, 2017.

[26] J. Charonko, B. Drew and S. Raben, "PRANA PIV Manual, Aether Lab," Virginia Polytechnic Institute and State University, 2011.

[27] N. Syred and K. Dahman, "Effect of High Levels of Confinement upon the Aerodynamics of Swirl Burners," *Journal of Energy,* vol. 2, no. 1, pp. 8-15, 1978.

[28] Y. Fu, "Aerodynamics and Combustion of Axial Swirlers, PhD Dissertation," University of Cincinnati, Cincinnati, 2008.

[29] N. Syred and J. Beer, "Combustion in Swirling Flow: A Review," *Combustion and Flame,* vol. 23, pp. 143-201, 1974.

[30] D. Lilley, "Swirling Flows in Combustion: A Review," *AIAA,* vol. 15, no. 8, pp. 1603-1678, 1977.

[31] E. Kilik, "Better Swirl Generation by Using Curved Vane Swirlers," in *AIAA 23th Aerospace Sciences Meeting*, Reno, NV, 1985.

[32] R. W. Schefer, "Flame Sheet Imaging Using CH Chemiluminescence," *Combustion and Technology,* Vols. 1-6, no. 126, pp. 255-279, 1997.

[33] J. Vorac, "massiveOES," Atlassian Inc., [Online]. Available: https://bitbucket.org/OES_muni/massiveoes. [Accessed 26 11 2018].

[34] C. Slabaugh, A. Pratt, R. Lucht, M. Benjamin, K. Lyle and M. Kelsey, "The development of an optically accessible high-power combustion test rig," *Review of Scientific Instruments,* vol. 85, pp. 1-9, 2014.

[35] R. R. Jagannath, K. Newnam, P. W. Stockett, P. Wu and S. P. M. Bane, "Volumetric Plasma Discharge in a Coaxial Electrode Configuration Using Repetitively Pulsed Nanosecond Discharges," in *55th AIAA Aerospace Sciences Meeting*, Grapevine, 2017.

[36] D. Z. Pai, D. A. Lacoste and C. O. Laux, "Transitions Between Corona, Glow, and Spark Regimes of Nanosecond Repetitively Pulsed Discharges in Air at Atmospheric Pressure," *Journal of Applied Physics,* vol. 107, p. 093303, 2010.

[37] S. Bhavini, L. K. Rajendran, M. Giarra, P. P. Vlachos and S. P. M. Bane, "Measurement of the flow field induced by a spark plasma using particle image velocimetry," *Experiments in Fluids,* vol. 59, no. 179, pp. 1-15, 2018.

[38] W. J and F. Scarano, "Universal Outlier Detection for PIV Data," *Experiments in Fluids,* vol. 39, pp. 1096-1100, 2005.

[39] S. Turns, An Introduction to Combustion Fundamentals, 1996.

[40] S. Andrey and A. Nikolay, "Plasma-Assisted Combustion Mechanism for Hydrogen and Small Hydrocarbons," in *AIAA Aerospace Sciences Meeting*, Kissimmee, 2015.

[41] Y.-H. Liao and X.-H. Zhao, "Plasma-Assisted Stabilization of Lifted Non-premixed Jet Flames," *energy&fuels,* vol. 32, pp. 3967-3974, 2018.

[42] S. A. Heitz, J. P. Moeck, T. Schuller, D. Veynante and D. A. Lacoste, "Influence of air flow parameters on nanosecond repetitively pulses discharges in a pin-annular electrode configuration," *Jounal of Physics; Applied Physics,* vol. 49, 2016.

[43] N. M. Numa, R. R. Jagannath, P. Stockett and S. P. Bane, "Development of Atmospheric-Pressure Plasma-Assisted Burner Using Naosecond Repetitively Pulsed Plasma Discharges," in *2018 AIAA Aerospace Sciences Meeting*, 2018.

[44] Y. Zuzeek, I. Choi, M. Uddi, I. V. Adamovich and W. R. Lempert, "Pure rotational CARS thermometry studies of low-temperature oxidation kinetics in air and ethene–air nanosecond pulse discharge plasmas.," *Joournal of Physics,* vol. 43, no. 12.

[45] J. J. Wang and e. al., "Recent Developments in DBD Plasma Flow Control.," *Progress in Aerospace Sciences,* vol. 62, pp. 52-78, 2013.

[46] I. Vigness and R. Nowak, "Streak Photography," *Journal of Applied Physics,* vol. 21, no. 5, pp. 445-448, 1950.

[47] Y. Tsuchiya, E. Iuzuka and Y. Suzuki, "Untrafast Streak Camera," *International Society for Optics and Photonics,* pp. 517-520, 1979.

[48] F. O. e. a. Thomas, "Optimization of Dielectric Barrier Discharge Plasma Actuators for Active Aerodynamic Control.," *AIAA Journal,* vol. 47, no. 1, pp. 2169-78, 2009.

[49] S. A. Stepanyan, S. A. Yu, N. A. Popov and Starikovskia, "A nanosecond surface dielectric barrier discharge in air at high pressures and different polarities of applied pulses: transition to filamentary mode," *Plasma Sources Science and Technology,* vol. 23, no. 045003, 2014.

[50] G. D. Stancu, M. Janda, F. Kaddouri, D. A. Lacoste and C. O. Laux, "Time-Resolved CRDS Measurements of the N2(A3Σu+) Density Produced by Nanosecond Discharges in Atmospheric Pressure Nitrogen and Air," *Journal of Physical Chemistry,* vol. 114, no. 1, pp. 201-208, 2010.

[51] S. Shcherbanev, N. Popov and S. Starikovskaia, "Multi-point nanosecond surface discharge at high pressures for plasma assisted ignition: spectroscopy of the filamentary phase," in *AIAA*, Kissimmee, 2018.

[52] D. L. Rusterholtz, D. A. Lacoste, G. D. Stancu and D. Z. Pai, "Ultrafast heating and oxygen dissociation in atmospheric pressure air by nanosecond repetitively pulsed discharges.," *Journal of Applied Physics,* vol. 46, no. 464010, p. 21, 2013.

[53] A. Rakitin and A. Starikovskii, "Streak Images of Pulses Discharges Development at High Voltage," *Transactions on Plasma Science,* vol. 36, no. 4, pp. 900-901, 2008.

[54] A. Rakitin and A. Starikovskii, "Mechanisms of Deflagration-to-Detonation Transition under Initiation by High-Voltage Nanosecond Discharges," *Combustion and Flame,* Vols. 1-2, no. 155, pp. 343-355, 2008.

[55] G. Perrott and D. Gawthrop, "Photography measurement of rate of detonation of explosives," *Journal of Franklin Institute,* vol. 203, no. 1, pp. 103-110, 1927.

[56] D. Packan, F. Grisch and B. Attal-Tretout, "Study of Plasma-Enhanced Combustion Using Optical Diagnostics," in *42nd AIAA Aerospace Sciences Meeting and Exhibit*, Reno, 2004.

[57] E. Moreau, "Airflow Control by Non-Thermal Plasma Actuators," *Jpurnal of Applied Physics,* vol. 40, pp. 605-636, 2007.

[58] S. Miura, T. Goto, Y. Syono and Y. Nakagawa, "High-Sensitivity Streak Camera Applicable to Time-Resolved Spectroscopy," *Physics, Chemistry, Metallurgy,* vol. 28, no. 1, pp. 80-92, 1979.

[59] K. Kinoshita and Y. Suzuki, "Streak Tube with Microchannel Plate," *International Society for Optics and Photonics,* pp. 504-507, 1979.

[60] R. R. Jagannath, K. Newnam, P. W. Stockett, P. Wu and S. P. M. Bane, "Volumetric Plasma Discharge in a Coaxial Electrode," in *AIAA SciTech Forum*, Grapevine, 2017.

[61] R. D. L., A. A. Lacoste, G. D. Stancu and D. Z. Pai, "Ultrafast heating and oxygen dissociation in atmospheric pressure air by nanoseconnd repetitively pulsed discharge," *J. Phys D: Appl. Phys.,* vol. 46, pp. 1-22, 2013.

[62] T. Corke and M. L. P. D. M. Orlov, "Single dielectric barrier discharge plasma enhanced aerodynamics: physics, modeling, and applications.," *Experiments in Fluids,* vol. 46, no. 1, pp. 1-26, 2009.

[63] T. C. Corke and S. P. W. C. L. Enloe, "Dielectric Barrier Discharge Plasma Actuators for Flow Control.," *Annual Review of Fluid Mechanics,* vol. 42, no. 1, pp. 505-529, 2010.

[64] P. Ceccato, O. Guaitella, M. Le Gloahec and A. Rousseau, "Time Resolved Nanosecond Plasma Discharge in Water at Positive Applied Voltage Polarity," *Journal of Applied Physics,* vol. 17, no. 43, pp. 175-202, 2010.

[65] D. Bradley and S. Majumdar, "A New Electron Image Time Dissector Framing Camera for High Speed Photography in the Nanosecond Region," *Journal of Photographic Science,* vol. 14, no. 3, pp. 134-142, 1966.

[66] D. Bradley, A. Durrant, F. O'Neill and B. Sutherland, "Picosecond Pulses from Mode-Locked Dye Lasers," *Physics Letters A,* vol. 30, no. 9, pp. 535-536, 1969.

[67] M. A. Boumehdi, S. A. Stepanyan, P. Desgroux, G. Vanhove and S. S. M, "Ignition of methane and n-butane containing mixtures at high pressures by pulsed nanosecond discharge," *Combustion and Flame,* vol. 162, pp. 1336-1349, 2015.

[68] N. Benard and E. Moreau, "Electrical and mechanical characteristics of surface AC dielectric barrier discharge plasma actuators applied to airflow control.," *Experiments in Fluids,* vol. 55, no. 11, 2014.

[69] N. Aleksandrov, G. Ivanov, S. Kindysheva, I. Kosarev, P. Sagulenko, S. Starikovskaia and A. Starikovskii, "Kinetics of Plasma Assisted Ignition at Elevated Temperatures: Experiments and Modeling," in *AIAA*, Reston, 2008.

[70] Specair 3.0, "www.spectralfit.com,," 2013. [Online].

[71] D L Rusterholtz, D A Lacoste, G D Stancu, D Z Pai, "Ultrafast heating and oxygen dissociation in atmospheric pressure air by nanosecond repetitively pulsed discharges," *J. Phys. D: Appl. Phys,* vol. 46, no. 464010 (21pp), 2013.

[72] Gabi D. Stancu*, Mario Janda†, Farah Kaddouri, Deanna A. Lacoste and Christophe O. Laux, "Time-Resolved CRDS Measurements of the N2(A3Σu+) Density Produced by Nanosecond Discharges in Atmospheric Pressure Nitrogen and Air," *J. Phys. Chem. A,,* Vols. 114 (1), pp 201–208, 2010.

[73] Yvette Zuzeek, Inchul Choi, Mruthunjaya Uddi, Igor V Adamovich and Walter R Lempert, "Pure rotational CARS thermometry studies of low-temperature oxidation kinetics in air and ethene–air nanosecond pulse discharge plasmas," *Journal of Physics D: Applied Physics,,* Vols. Volume 43, , no. Number 12.

[74] Pai, D. Z., Stancu, G. D., Lacoste, D. A., & Laux, C. O., "Nanosecond repetitively pulsed discharges in air at atmospheric pressure—the glow regime.," *Plasma Sources Science and Technology, ,* Vols. 18(4), 045030., 2009.

[75] "Google Images," Google. [Online]. [Accessed 26 February 2019].

APPENDIX A

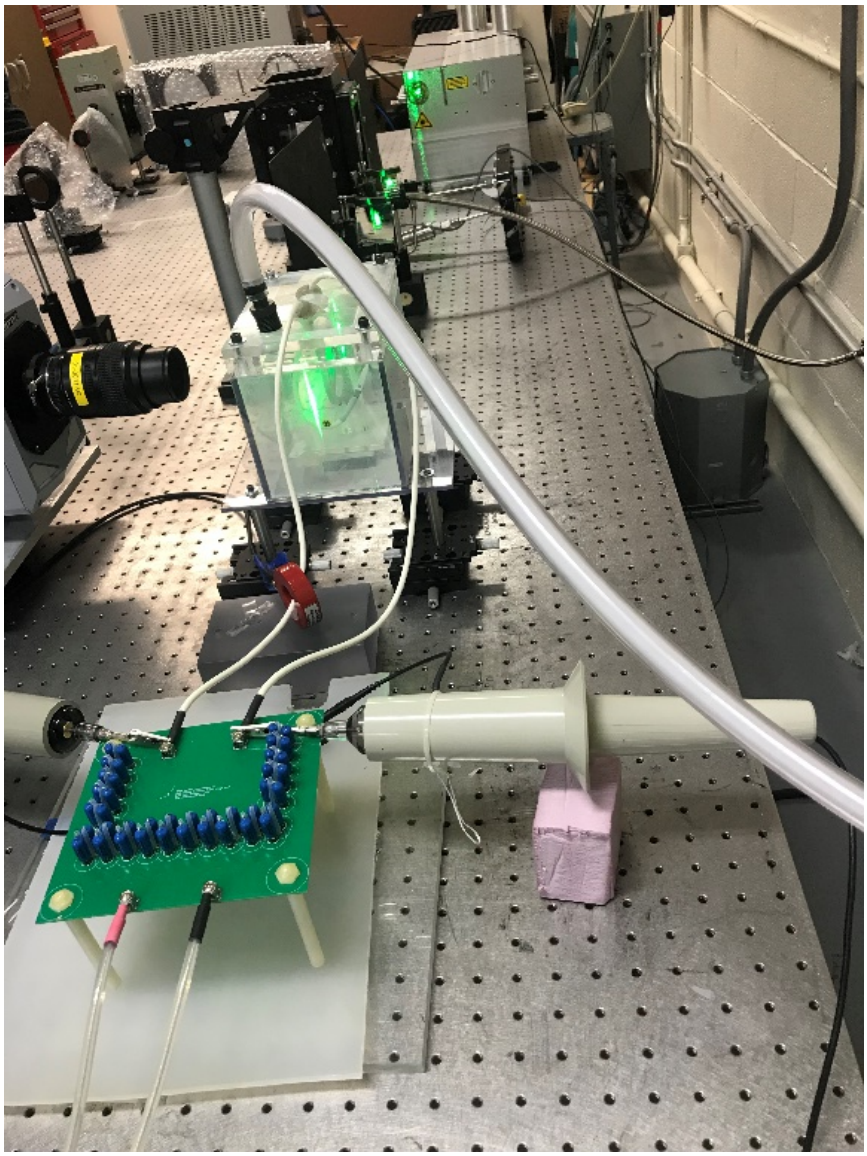

Figure 68: Photograph of the PIV setup.

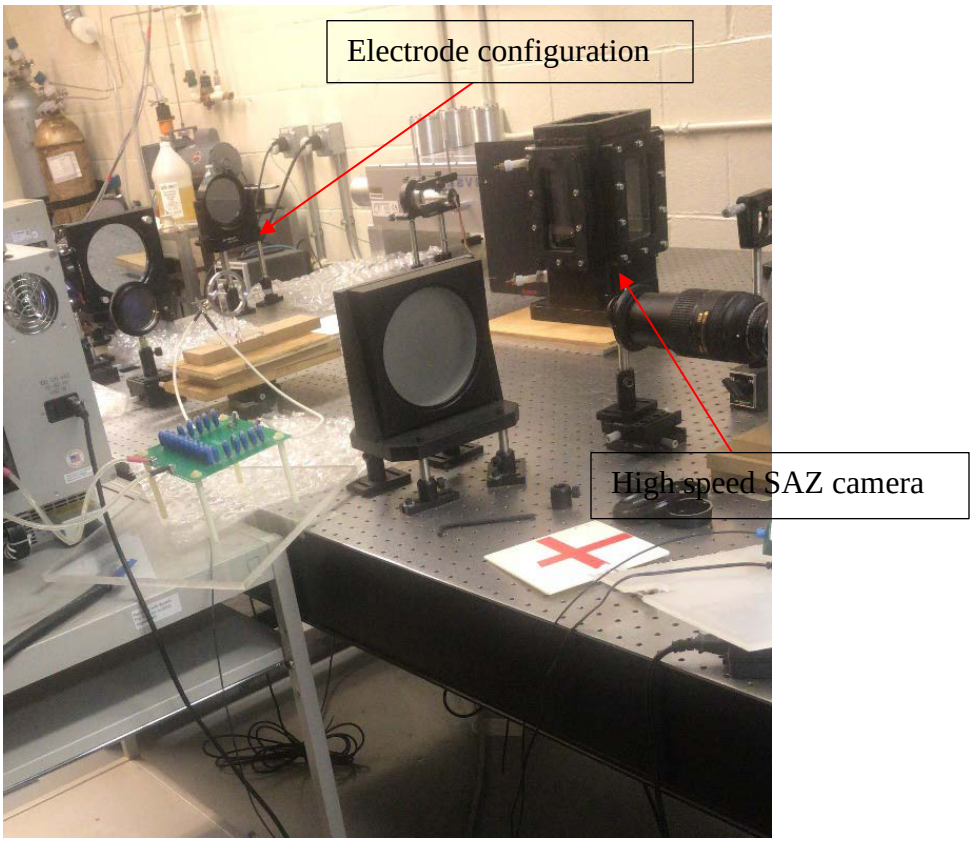

Figure 69: Photograph of the high speed schlieren visualization setup.

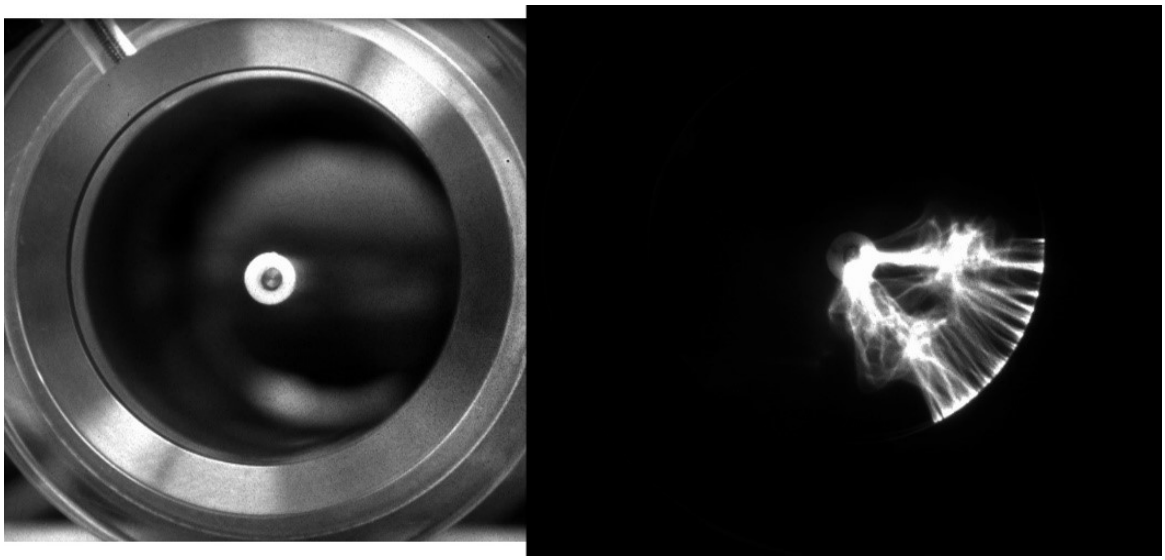

Figure 70: Photograph of a plasma discharge generated at the burner outlet at 5000 pulses and a PRF of 50 kHz.

APPENDIX B

Liftoff Height Code

```
% This code is to estimate the liftoff height for the PAB
clc
clear
close all
% Loop to iterate through 500 images

for idx = 101:551

    idx % This is to check if the loop is actually working

    if idx > 0 && idx < 9
        str1 = '200_0.6900000';
    elseif idx > 10 && idx < 100
        str2 = '200_0.690000';
    elseif idx > 100 && idx < 999
        str3 = '200_0.69000';

    else
        str4 = '200_0.6900'; % Indicator for code to identify the TIFF imahes
    end

    list = num2str(idx); % Changing the index to a string

    filename = [str3,list,'.tif']; % combining the previous variables to
create the filename

    output = imread(filename); % reading the TIFF images

    I = mat2gray(output); % conerting to grayscale to observe the intensity

    y = [0 1024]; % y-axis to add a line in mid of image to evaluate
intensity
    x = [525 525]; % y-axis to add a line in mid of image to evaluate
intensity
    c = improfile(I,x,y); % plotting the intensity profile

% This section plots the intensity and performs a fit on the intensities
%     figure
%     subplot(2,1,1)
%     imshow(I)
%     hold on
%     plot(x,y,'r')
%     B = [1:500]';
%     p = polyfit(B,c(2:501,1),3);
%     f = polyval(p,B);
%     subplot(2,1,2)
%     plot(c(2:501,1,1),'b')
%     hold on
%     plot(f,'g')
```

```
    threshold = 60; % Threshold to determine the bottom of the flame
    for r = 1:1024 % Evaluates the image from top to bottom
        % Checks to see where output is greater than threshold and that is
        % the bottom of the flame
         if output(r,512) < threshold
            flame_bot(idx) = r;
            break % break if you find it
         end

    end
%
%     calibration_mm = 0.004434; % mm/pixel for images taken with the
SAZ+intensifier
    calibration = 0.0016602; % in/pixel
    lift(idx) = 1024 - flame_bot(idx); % Subtracting from the total frame
size
    lofh_in(idx) = lift(idx) * calibration; % in inches
    lofh_final(idx) = lofh_in(idx) + 0.917; % in inches

end
histogram(lofh_final(101:551))
S = std(lofh_final(101:551));
lofh_mean = mean(lofh_final(101:551));
```

Energy Code

```
close all
clear
clc
%% Calling the correct data from the channels
filename = 'wave00000001_Ch2.xlsx';
filename_2 = 'wave00000001_Ch3.xlsx';
%% Reading the excel files
A = xlsread(filename);           % Voltage
B = xlsread(filename_2);         % Current
%% Sorting through to extract
Time = A(:,3);          % Time, this is also chosen for current assuming
there's no shift between cur & vol
Voltage = A(:,4).* 1000;         % multip by 1000 for calculations
Current = 10 .* B(:,4);          % multip by 10 for the attenuation
VI = Voltage .* abs(Current);    % product of voltage and current to obtain
energy
%% Energy from each pulse in the train
delT_matrix = -diff(Time);       % establishing a delta t between points
delT = 4.0E-10;                  % divisions in the scope is 40ns
energy = VI .* delT;

%% Total Energy
tot_ener_1 = energy(:,1);
Energy_1(1048576,1) = zeros;

k = 2;     % k = 1
j = 5000;  % j = 3000

while j < 1048576
```

```
        for i = k:j

            Energy_1(i) = tot_ener_1(i) + Energy_1(i-1);

        end

        k = j + 45000;
        j = k + 5000;

end

% order = 3;
% framelen = 51;
% sgf = sgolayfilt(abs(Current),order,framelen);
%
% plot(Time(350001:1048576)./10^-3,sgf(350001:1048576))
% xlabel('Time (ms)', 'FontSize', 16)
% ylabel('Current (A)', 'FontSize', 16)
% title('200 SLPM, ER = 0.62, 50 kHz, Pulse # 3008-3022', 'FontSize', 16)
%
% order = 3;
% framelen = 51;
% sgf = sgolayfilt(abs(Current),order,framelen);
%
% yyaxis left
% plot(Time(350001:1048576)./10^-3,Energy_1(350001:1048576).*10^3)
% xlabel('Time (ms)','FontSize', 16)
% ylabel('Total Energy (mJ)','FontSize', 16)
% yyaxis right
% plot(Time(350001:1048576)./10^-3,sgf(350001:1048576))
% ylabel('Current (A)','FontSize', 16)
% title('200 SLPM, ER = 0.60, 50 kHz, Pulse # 3008-3022','FontSize', 16)

order = 3;
framelen = 51;
sgf = sgolayfilt(abs(Current),order,framelen);

yyaxis left
plot(Time./10^-3,Energy_1.*10^3)
xlabel('Time (ms)')
ylabel('Total Energy (mJ)')
yyaxis right
plot(Time./10^-3,sgf)
ylabel('Current (A)')
title('200 SLPM, ER = 0.58, 50 kHz, Pulse # 301-322')

order = 3;
framelen = 51;
sgf = sgolayfilt(abs(Voltage),order,framelen);
yyaxis left
plot(Time./10^-3,Energy_1.*10^3)
xlabel('Time (ms)')
ylabel('Total Energy (mJ)')
yyaxis right
plot(Time./10^-3,sgf/10^3)
```

```
ylabel('Voltage (kV)')
title('200 SLPM, ER = 0.58, 50 kHz, Pulse # 301-322')

order = 3;
framelen = 51;
sgf_vol = sgolayfilt(abs(Voltage),order,framelen);
sgf_cur = sgolayfilt(abs(Current),order,framelen);
yyaxis left
plot(Time./10^-3,sgf_vol/10^3)
xlabel('Time (ms)')
ylabel('Voltage (kV)')
yyaxis right
plot(Time./10^-3,sgf_cur)
ylabel('Current (A)')
title('200 SLPM, ER = 0.58, 50 kHz, Pulse # 301-322')
```

APPENDIX C

	PURDUE UNIVERSITY	
	Aerospace Sciences Laboratory	
	Location: MSEE 345 Plasma Lab	
	Plasma Assisted Flame Test Procedures	
	Written by: Nadia Numa, Naveen Joel	
Test Requirements: Tests will be performed during normal business hours with minimum two students authorized to work by Dr. Sally Bane. All safety equipment must be present before tests begin. Extraneous personnel should be cleared of lab/control room areas prior to running a test sequence.		
SECTION 0: EMERGENCY		
IN CASE OF LEAK, FIRE, OR OTHER INCIDENT		
0.000	Test conductors will use their best judgment to determine the severity of the situation. Contact the appropriate stakeholders if necessary.	
0.001	Regardless of the incident severity, the appropriate personnel will be notified by phone of the incident and will provide guidance for further action. Sally Bane: 765-414-1357	
ITEMS NEEDED		
0.002	Labcoats, safety glasses/face shields, nitrile gloves, paper towels	
SECTION 1. OVERALL TEST SETUP		
1.001	Ensure test location is clear of debris and only the test personnel are present in the location	
1.002	Ensure that the fume hood is ON and clear of any unwanted material	
1.003	Verify that the burner is placed securely under the fume hood and mobile cart is placed securely near the burner	

1.004	Retrieve all the specific settings and parameters for all the components from the corresponding test cases in the test matrix	
1.005	Ensure that the experiment is assembled correctly - all Air, N2 and CH4 lines are assembled correctly and tightened	
1.006	Turn the 3-way manual valve MV-N2-01 to direct the flow to the burner line	
1.007	Ensure the NI USB cable is connected to the computer and that the ethernet cable is also connected to the computer	
1.008	Turn on the NI DAQ and start VI using LabView on the lab computer	
1.009	Ensure the valves are CLOSED in the VI (the valve gui must be BLACK) and then turn on the DAQ box knob to ON	
1.010	Ensure that MR-N2-01 on the bottle is unloaded (the regulator hand valve) all the way	
1.011	Open the N2-01 bottle all the way and close 1/4-1/2 a turn	
1.012	Load MR-N2-01 on the N2-01 bottle to 100 psi for pneumatic valve operation	
1.013	RUN the VI and valve check PV-AIR, PV-N2, and PV-FU and ensure all valves are CLOSED	
	make sure N2 valve faces down at beginning of test (points up = to burner via air line; down = to CH4 line)	
	bottles need to be iopen, load to 50 each and N2 pneumatics to 90psi	
1.014	Monitor the plumbing lines in this step to ensure there are no leaks	
1.015	Ensure that the Pulser is OFF and placed securely at a safe distance from cylinders	
1.016	Place the oscilloscope and pulse generator on the cart securely and close to the Pulser	
1.1 CAMERA AND DELAY GENERATOR SETUP		
1.101	Connect the camera trigger to Channel A and Pulser trigger to Channel B of the delay generator	
1.102	Switch on the delay generator and enter the retrieved settings for each channel of the delay generator. See Camera & Delay Generator Sheet	
1.103	**ALL CAMERA AND FILTER SETTINGS TO BE ADDED HERE**	
1.104	Continuously adjust to verify that cameras are focused correctly and hit the trigger button on the cameras to wait for a trigger from the delay generator. Verify.	
1.105	Run the trigger button and ensure that the camera is triggered correctly after the specified delay. Check image for focus and repeat 1.104 if needed	
1.2 PULSER AND OSCILLOSCOPE SETUP		
1.201	Connect all the power cords on the pulser and connect the pulser trigger through the fiber transmitter	

1.202	Connect the voltage clips from the pulser to the respective electrodes on the burner setup. RED = Pin BLACK = Ring	
1.203	Ensure the wires from the pulser to the resistor unit and the voltage lines to the electrodes are atleast 2" away from the ground	
1.204	Clip the voltage probes to the electrodes; Place the current probe through one of the voltage lines.	
1.205	Connect the voltage and current probes to the channels of the oscilloscope through BNC cables	
1.206	Turn on the oscilloscope, launch the application and enter retrieved oscilloscope settings for the output display and triggers. See SCOPE settings	
1.207	Hit RUN and ensure that the oscilloscope is waiting for trigger signal from the respective channel	
1.208	**ANNOUNCE WARNING: HIGH VOLTAGE TO BE TURNED ON! ALL NEARBY PERSONNEL TO MOVE 3 FT AWAY FROM BURNER**	
1.209	Turn on the Pulser and set the retrieved parameters for the test case from the test matrix	
1.210	Trigger the pulse generator and ensure the plasma forms at the desired location at the exit plane of the burner.	
1.211	Ensure the voltage and current output on the scope and symmetric and without errors	
1.212	Verify the waveforms are as expected. If the current waveform is negative, position the current probe such that the arrow points to the opposite direction.	
SECTION 2. PRE-TEST PROCEDURES		
2.001	Put on PPE (lab coat, face shield and nitrile gloves)	
2.002	Ensure that MR-AIR on the air cylinder is unloaded all the way and the needle valve NV-AIR is fully open. Needle valve is at the back of the regulator	
2.003	Open the air cylinder all the way and close 1/4 - 1/2 turn	
2.004	Load MR-AIR to 100 psi for air flow	
2.005	Ensure that MR-N2-02 on the N2-02 cylinder is unloaded all the way and the needle valve NV-N2-02 is fully open	
2.006	Open the N2-02 cylinder all the way and close 1/4 - 1/2 turn	
2.007	Load MR-N2-02 to 100 psi for nitrogen purge flow	
2.008	Ensure that MR-CH4 on the CH4 cylinder is unloaded all the way and the needle valve NV-CH4 is fully open	
2.009	Open the CH4 cylinder all the way and close 1/4 - 1/2 turn	
2.010	Load MR-CH4 to 80 psi for CH4 fuel flow	
2.011	Set the retrieved flow rate setting for the air and fuel mass flow controllers for a given equivalence ratio using the VI. See MATRIX for flow rates and voltage settings	

SECTION 3. TESTING		
	Set flow rates to both MFCs verify mass flow controller operational	
3.001	Set correct flow rate via voltage for the test to begin	
3.002	OPEN PV-AIR and ensure that output pressure is 100 psi and verify correct flow rate on the air mass flow controller	
3.003	OPEN PV-FU and ensure that output pressure is 80 psi and verify correct flow rate on the fuel mass flow controller	
3.004	**ANNOUNCE WARNING: FLAME TO BE IGNITED**	
3.005	Ignite the flame by triggering the pulse generator to create the plasma and also the camera to capture the images	
3.006	**INCASE OF UNEXPECTED FLAME BEHAVIOUR OR HAZARD, ABORT TEST BY SHUTTING OFF PV-FU IMMEDIATELY**	
3.007	Make necessary observations and check for flame stabilization	
3.008	Record all required data (camera images, voltage and current recordings, etc.,) and ensure correct readings	
3.009	After test is over, CLOSE PV-AIR, PV-FU and PV-N2 bottles	
3.010	Evaluate and save all data files	
3.011	If exact same test case is to repeated, repeat steps 3.001 to 3.010	
3.012	If a different test case is to be executed, go to CHANGE SETTINGS AND PARAMETERS section 4	
3.013	If NO additional testing is to be done, skip to the SHUTDOWN AND CLEANUP section 5	
SECTION 4. CHANGE SETTINGS AND PARAMETERS		
4.001	If some adjustment is required on the burner setup or the electrodes, turn OFF the pulser and discharge using discharge stick to ground	
4.002	Measure the burner surface temperature using surface thermocouple and ensure safe temperature for handling burner	
4.003	If adjustments are not required on the burner or electrodes, skip the above two steps and proceed to the next step	
4.004	Turn the 3-way manual valve MV-N2-01 to direct the flow to fuel line	
4.005	OPEN PV-N2 valve to purge the fuel line for 1 min. Flip the 3 way valve to purge the burner line for 3 mins	
4.006	Make changes to the settings on the delay generator for the new test case using new settings from the test matrix	
4.007	Repeat the above step for camera settings, pulser settings and oscilloscope settings for the new test case and ensure correct settings	
4.008	Verify that cameras are focused correctly and hit the trigger buttons on the cameras to wait for a trigger from the delay generator	

4.009	Run the trigger button and ensure that the camera is triggered correctly after the specified delay	
4.010	Hit RUN on the oscilloscope and ensure that it is waiting for trigger signal from the respective channel	
4.011	If pulser had been turned OFF, issue the high voltage warning again and turn ON the pulser	
4.012	Trigger the pulse generator and ensure the plasma forms at the desired location at the exit plane of the burner	
4.013	Ensure the voltage and current output on the scope and symmetric and without errors	
4.014	If equivalence ratio is to be changed, keeping the air flow rate constant, adjust the flow rate of the fuel line using value from test matrix	
4.015	After all settings and parameters have been changed corresponding to the new test case, go to TESTING section 3	
SECTION 5. SHUTDOWN AND CLEANUP		
5.001	Ensure that all data has been saved properly	
5.002	CLOSE Air and Fuel bottles and secure them tightly	
5.004	Set mass flow rate on CH4 flowmeter on VI for depressurizing, set 0.1 for voltage	
5.005	OPEN PV-FU to de-pressurize the line	
5.006	With PV-FU open, load MR-CH4 slightly (depressurizing the first gauge) and ensure both dials on the regs display read 0	
	Unload CH4 regulator then set MFC to 0 voltage	
5.007	Repeat steps 5.004 to 5.006 for air bottle as well to depressurize the air line and set air mass flow rate to zero	
5.008	Set a desired mass flow rate on MFC-CH4 for purging ch4 line after depressurizing it	
5.009	Turn the 3-way manual valve MV-N2-01 to direct flow towards the fuel line for purging	
	Close CH4 and Air valves	
5.010	OPEN PV-N2 valve to begin purging the fuel line for ~1 minute	
	add "1.1 the ch4 mfc to pull N2 to purge	
5.011	Turn the 3-way manual valve MV-N2-01 to direct flow to the burner and purge the burner for ~3 minutes	
	zero MFC first	
5.013	CLOSE N2-02 bottle fully and secure it tightly	
5.015	With PV-N2 open, load MFC-CH4 slightly (depressurizing the first gauge) and ensure both dials read 0	

5.016	Unload MR-N2-02 completely	
	set MFC to 0 and close N2 on the VI	
	close N2 bottles that is used for pneumatics	
5.017	CYCLE PV-N2 several times until pneumatic lines are depressurized	
	just open one of the valves to make sure reg goes to zero; click the valve open and close until there is no "pop" when you actuate it open	
	unload N2 reg	
	turn off MFCs	
5.018	Turn off the high voltage of the pulser and switch off all the power lines	
5.019	Discharge the anode and cathode connections to the ground to prevent static shocks	
5.020	STOP the VI and exit LabView application	
5.021	Turn off the DAQ and switch off the DAQ power strip	
5.022	Turn off the delay generator	
5.023	Turn off the oscilloscope and computer	
5.024	Complete testing and cleanup the test location	